

Digital Control Systems in the Regeneration Cavity of
ALPS IIa

Von der Fakultät für Mathematik und Physik
der Gottfried Wilhelm Leibniz Universität Hannover
zur Erlangung des Grades
Doktor der Naturwissenschaften
Dr. rer. nat.

genehmigte Dissertation von

Richard Cameron Gardner Smith

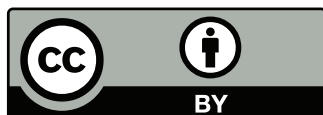
2020

Referent: apl. Prof. Dr. Benno Willke
Koreferent: Prof. Dr. Guido Müller
Korreferentin: Prof. Dr. Michèle Heurs
Koreferent: Dr. Axel Lindner
Tag der Promotion: 12 Oktober 2020

This work is licensed under a Creative Commons Attribution 4.0 International License (<https://creativecommons.org/licenses/by/4.0/>).

The terms of the Creative Commons license only apply to original material.

Reuse of material from other sources (marked by quoting the original source) such as diagrams, images, photos and text extracts may require further usage permits from the respective rights holder.



Abstract

ALPS II is a light-shining-through-a-wall experiment that will search for axion-like particles. These experiments seek to generate and measure axion-like particles in a laboratory using oscillations between photons and axions in the presence of a magnetic field. ALPS II builds on the innovation of its predecessor, ALPS I: optical cavities to enhance the sensitivity. ALPS II will use a production cavity (PC) to increase the number of photons available to generate axion-like particles, and a regeneration cavity (RC) to enhance the probability of the axion-like particles oscillating back into photons.

To resonantly enhance the light in the cavities, the input laser light needs to be well-matched to the resonance of the cavities even in the presence of disturbances. Additionally, the resonances of the two cavities must be matched such that the axion-like particles' reconversion probability is enhanced in the RC. The requirement on the frequency noise between the two cavities for ALPS IIc is a root-mean-square (RMS) deviation of smaller than 3.0 Hz. This necessitates the use of high-performance control loops.

ALPS IIa is a smaller-scale experiment to test and characterize critical systems for use in the full-scale ALPS IIc. ALPS IIa has the facilities for two cavities to mirror the PC and RC in ALPS IIc. Control systems can be designed and tested to determine their suitability for use in ALPS IIc, and alternative designs can be compared based on their performance in the short-scale experiment.

In this thesis, the baseline analog control systems in the ALPS IIa RC are characterized. These include frequency actuation systems for two laser sources, and a length actuation system. The noise of this length actuation system is projected onto the requirements of the resonance overlap between the two cavities and an RMS of 1.0 Hz should be achievable with this system.

In order to investigate the viability of digital control systems, two digital frequency control systems are tested: one that replaces the analog servo, and one that replaces the analog demodulation system as well. The RMS of the frequency noise of both digital systems is within a factor of two of the fully analog system. The system with the digital demodulation is the better-performing of the two.

A fully digital system is designed to sense phase changes between the light circulating in the two cavities to minimize that phase difference. This system is able to actuate on laser frequency to achieve similar performance to other frequency control systems.

Keywords: axion-like particles, optical cavities, digital control systems

Zusammenfassung

ALPS II ist ein Licht durch die Wand-Experiment, das nach axionartigen Teilchen sucht. Diese Experimente zielen darauf ab axionartige Teilchen in einem Labor zu erzeugen und zu messen, wobei in Gegenwart eines Magnetfelds die Oszillation zwischen Photonen und axionartige Teilchen erfolgt. ALPS II baut auf die Neuerungen seines Vorgängerexperiments ALPS I auf: optische Resonatoren zur Verbesserung der Empfindlichkeit. ALPS II wird einen Produktionsresonator (PC) verwenden, um die Anzahl der zur Erzeugung von axionartigen Teilchen verfügbaren Photonen zu erhöhen und einen Regenerationsresonator (RC), um die Wahrscheinlichkeit zu erhöhen, dass axionartige Teilchen zurück in Photonen konvertieren.

Um das Licht in den Resonatoren resonant zu überhöhen, muss das auf den Resonator einfallende Laserlicht, auch in Gegenwart von Rauschquellen, an die Resonanz des Resonators angepasst werden. Zusätzlich müssen die Resonanzen der beiden Resonatoren so aufeinander abgestimmt werden, dass die Rekonversionswahrscheinlichkeit der axionartigen Teilchen im RC erhöht wird. Die Anforderung an das Frequenzrauschen zwischen den beiden Resonatoren für ALPS IIc müssen kleiner sein als eine Effektivwertabweichung (RMS) von 3.0 Hz. Dies erfordert die Verwendung von Regelkreisen mit hohen Regelbandbreiten.

ALPS IIa ist ein kleineres Experiment zum Testen und Charakterisieren kritischer Systeme für den Einsatz in ALPS IIc. ALPS IIa verfügt über Räumlichkeiten, in denen zwei Resonatoren, ähnlich der PC und RC in ALPS IIc, aufgebaut sind. Regelkreise können entworfen und getestet werden, um sie für die Eignung in ALPS IIc zu testen und die Leistungsfähigkeit alternativer Designs kann im kleinen Mastab evaluiert werden.

In dieser Dissertation werden die grundlegenden analogen Regelkreise der ALPS IIa RC charakterisiert. Dazu gehören Frequenzstabilisierungssysteme für zwei Laserquellen und ein Längenstabilisierungssystem. Das Rauschen dieses Längenstabilisierungssystems wird auf die Anforderungen der Resonanzüberlappung zwischen den beiden Resonatoren projiziert und ein RMS Wert von 1.0 Hz sollte mit diesem System erreicht werden.

Um die Funktionsfähigkeit digitaler Regelsysteme zu untersuchen, werden zwei digitale Frequenzstabilisierungssysteme getestet: eines, das analoge Servo ersetzt, und eines, das zusätzlich das analoge Demodulationssystem ersetzt. Das RMS des Frequenzrauschens beider digitaler Systeme liegt innerhalb eines Faktors von zwei des vollständig analogen Systems. Das System mit der digitalen Demodulation ist das leistungsfähigere der beiden Systeme.

Ein vollständig digitales System ist so ausgelegt, dass es Phasenänderungen zwischen dem in den beiden Resonatoren zirkulierenden Licht erfasst, um Phasendifferenzen zu minimieren. Dieses System kann die Laserfrequenz beeinflussen und eine ähnliche Stabilität wie andere Frequenzstabilisierungssysteme erreichen.

Stichworte: axionartigen Teilchen, optische Resonatoren, digitale Regelsysteme

Contents

Abstract	iii
Zusammenfassung	iv
List of Abbreviations	viii
List of Figures	ix
1. Introduction	2
1.1. Axion-Like Particles	2
1.2. Any Light Particle Search	5
1.3. Optical Cavities	8
1.4. Cavity Field Sensing	12
1.5. Use of Optical Cavities in ALPS II	16
2. Controls and Digital Signal Processing	24
2.1. Feedback Control Systems	24
2.2. Transfer Functions	27
2.3. Control Stability	30
2.4. Discrete Time	32
2.5. Quantization in Digital Systems	34
3. ALPS IIa Regeneration Cavity	37
3.1. Calibration	37
3.2. Infrared Frequency Control	39
3.3. Green Frequency Control	47
3.4. Green Length Control	55
3.5. Mirror Actuator Design	65
3.6. Conclusions	69
4. Digital Frequency Control	70
4.1. Digital Architecture	70
4.2. Frequency Control with a Digital Servo	71
4.3. Fully Digital Frequency Control System	77
4.4. Conclusions	81
5. Digital Phase-Locked Loop	84
5.1. Phase-Locked Loops	84

5.2. Phase-Locked Loop for Frequency Actuation	90
5.3. Simulated Length Actuation	95
5.4. Measuring Cavity Free Spectral Range and Linewidth Using a Phase-Lock Loop	99
5.5. Conclusions	101
6. Conclusions	103
Bibliography	106
A. State Space Models	110
A.1. State Space Representation	110
A.2. Converting a State-Space Model to a Transfer Function Model	111
A.3. Converting a Transfer Function Model to a State-Space Model	113
A.4. Discrete State Space	117
A.5. Converting a Transfer Function Model to a State-Space Model in Discrete Time	117
Acknowledgments	120
Curriculum Vitae	122
Publications	123

List of Abbreviations

ALPS	Any Light Particle Search
PDH	Pound-Drever-Hall
IR	Infrared
RC	Regeneration Cavity
HPL	High-Power Laser
RL	Reference Laser
FPGA	Field Programmable Gate Array
PC	Production Cavity
TES	Transition Edge Sensor
WISP	Weakly-Interacting Slim Particle
LSW	Light Shining Through a Wall
SNR	Signal-to-Noise Ratio
FSR	Free Spectral Range
FWHM	Full Width at Half Maximum
RF	Radio Frequency
EOM	Electro-Optic Modulator
RMS	Root-Mean-Square
LO	Local Oscillator
FCS	Feedback Control System
ADC	Analog to Digital Converter
LSB	Least Significant Bit
RAM	Residual Amplitude Modulation
DAC	Digital to Analog Converter
DESY	Deutsches Elektronen-Synchrotron
mTCA	MicroTCA
AMC	Advanced Mezzanine Card
RTM	Rear Transition Module
PLL	Phase-Locked Loop
NCO	Numerically-Controlled Oscillator

List of Figures

1.1.	Exclusion plot of axion-like particle experiments.	4
1.2.	Schematic diagram of the ALPS II experiment.	7
1.3.	ALPS IIa Regeneration Cavity Schematic.	8
1.4.	Axial cavity modes.	11
1.5.	Fullwidth at half maximum of an axial cavity mode.	12
1.6.	How to generate Pound-Drever-Hall signal.	13
1.7.	Detecting PDH error signals.	15
1.8.	Example of a Pound-Drever-Hall error signal.	16
1.9.	Example of a Pound-Drever-Hall error signal near resonance.	17
2.1.	Feedback control system to keep a laser resonant with an optical cavity. . .	25
2.2.	Example of quantization.	35
3.1.	Example of a calibrated control and error amplitude spectral density. . . .	38
3.2.	Example of an open-loop transfer function.	39
3.3.	Feedback control system to match infrared high power laser to the ALPS IIa regeneration cavity.	40
3.4.	Open-loop transfer function for the high power laser frequency control system.	41
3.5.	IR ring-down measurement of ALPS IIa RC.	42
3.6.	Control and error signal amplitude spectral density for frequency control of the high power laser to match the ALPS IIa RC.	44
3.7.	Sensing noise of different components of the HPL sensing system.	45
3.8.	Error signal amplitude spectral density compared to sensing noise am- plitude spectral density for frequency control of the high power laser to match the ALPS IIa RC.	46
3.9.	Feedback control system to match frequency doubled reference laser to the ALPS IIa regeneration cavity.	47
3.10.	Open-loop transfer function for the frequency-doubled reference laser fre- quency control system compared to the high power laser frequency control system.	48
3.11.	Control and error spectra for green frequency control.	49
3.12.	Primary and secondary sensing path error compared to sensing noise am- plitude spectral density for frequency control of the reference laser.	50
3.13.	Sensing noise of different components of the primary RL sensing system. . .	51
3.14.	Sensing noise produced at different parts of the secondary detection path. .	52
3.15.	Electronic noise from electronics to control the offset of the error signal. .	53

3.16. Experimental setup to investigate optical source of sensing noise.	54
3.17. Optical sensing noise before and after sensing system.	55
3.18. Mirror mount with piezo actuator.	56
3.19. Schematic of length control with digital filtering.	57
3.20. Comparison of mirror actuator transfer function with and without compensation.	58
3.21. Comparison of length control open-loop transfer function with and without compensation.	59
3.22. Control and error spectra for length control without compensating for actuator resonances.	60
3.23. Sensing noise produced by the analog and digital parts of the error path. .	61
3.24. Control and error spectra for length control compensating for actuator resonances.	62
3.25. Sensing noise compared to primary and secondary error spectra for compensated length control system.	63
3.26. Comparison of error spectra between compensated and uncompensated length control.	64
3.27. Projection of compensated and uncompensated length control onto the coupling between the two cavities of ALPS IIc.	65
3.28. Mirror actuator design using a mirror holder.	66
3.29. Mirror holder assembly.	67
3.30. Transfer function of 3-axis and mirror holder actuators.	68
4.1. Schematic of a feedback control system with a digital servo.	72
4.2. Open-loop transfer function of green frequency control with analog and digital servos.	73
4.3. Control and error signal with FPGA as digital servo.	74
4.4. Sensing noise of primary error signal path with FPGA as digital servo. . .	75
4.5. Primary and secondary error spectra compared with sensing noise.	76
4.6. Error spectra of secondary sensing path comparing analog servo to digital servo performance.	77
4.7. Schematic of a fully digital feedback control system.	78
4.8. Open-loop transfer function of green frequency control with fully digital control compared to fully analog control.	79
4.9. Control and error signal with FPGA as full control system.	80
4.10. Sensing noise of primary error signal path with FPGA as full control system.	81
4.11. Secondary error spectrum compared with sensing noise.	82
4.12. Error spectra of secondary sensing path comparing fully analog system to fully digital system performance.	83
5.1. Schematic of concept to ensure dual resonance between the PC and RC with the TES detector.	86
5.2. Schematic of a phase-locked loop controller design with a numerically-controlled oscillator for high-speed phase tracking.	87

5.3. Schematic of a one-cavity test of phase-locked loop length control.	88
5.4. Schematic of a phase-locked loop controller and sensing system for the ALPS IIa RC.	90
5.5. Open-loop transfer function of the phase-locked loop compared to the analog frequency control.	91
5.6. Control and PDH spectra for the phase-locked loop.	92
5.7. Phase-locked loop PDH spectrum compared to noise sources.	93
5.8. Phase-locked loop PDH spectrum compared to analog and digital frequency control error spectrum.	94
5.9. Open-loop transfer function of the phase-locked loop length control simulation compared to the compensated length control.	96
5.10. Control and PDH spectra for the phase-locked loop.	97
5.11. Calculated servo gain of the phase-locked loop length control simulation compared to the compensated length control.	98
5.12. Phase-locked loop length control simulation PDH spectrum compared to noise sources.	98
5.13. Phase-locked loop length control simulation PDH spectrum compared to compensated length control error spectrum.	99
5.14. Phase-locked loop length control simulation PDH spectrum compared to compensated length control error spectrum with both projected onto the ALPS IIc cavities.	100
5.15. Measurement of the transmitted power versus the RL offset frequency for two cavity resonances separated by a free spectral range.	101
5.16. All cavity resonance measurements overlaid.	102

1. Introduction

The Any Light Particle Search (ALPS) is an experiment to find novel particles. These particles, known as axion-like particles, are a type of weakly-interacting slim particles (WISPs) that are part of a theorized extension of the standard model of particle physics. One of the critical technologies used in ALPS is the use of optical cavities to enhance the probability of detecting these particles. This thesis will discuss and characterize one of the cavities of the technology demonstrator phase of the ALPS II experiment, and investigate the potential for digital control of these cavities in comparison with both the analog systems and the requirements for the full-scale phase of the experiment.

1.1. Axion-Like Particles

The standard model of particle physics has successfully predicted a number of particles and has been instrumental in many other aspects of particle physics [1]. However, not all observations can be explained by physics described in the standard model. The most apparent discrepancy is that only $\sim 5\%$ of the energy in the universe can be explained by the standard model, with the rest of it currently known as either dark matter or dark energy.

One particle predicted to exist beyond what has been described and identified in the standard model is the axion, which could explain why the charge polarity is almost perfectly symmetrical in the strong force despite no requirement for such behavior in the standard model [2]. Additionally, astrophysical observations suggest that there could be additional particles similar to the axions, which are known as axion-like particles. These observations include a larger-than-expected transparency of the universe to high-energy photons [3] and an unexplained energy loss in some stars [4]. These particles would also constitute a significant contribution to the energy of what is currently known only as dark matter [5].

One of the properties of these axion-like particles that is most relevant to the ALPS experiment is that they can couple to two photons. The first of the two photons is from a light source such as a laser, and the second of the two photons is a virtual photon supplied by a magnetic field. The probability of this coupling is described by

$$p_{\gamma \rightarrow A} = \frac{1}{4} \frac{\omega}{\sqrt{\omega^2 - m_A^2}} (g_{A\gamma\gamma} BL)^2 |F(qL)|^2, \quad (1.1)$$

where ω is the photon frequency, m_A is the axion-like particle mass, $g_{A\gamma\gamma}$ is the axion-to-photon coupling constant, B is the magnetic field strength, L is the length of the interaction, $F(qL)$ is the form factor, and q is the momentum transfer from the photon

to the magnetic field [6]. As a note for these calculations, $\hbar = c = 1$. Additionally, the probability of photons oscillating into an axion-like particle is the same as the probability of the conversion of an axion-like particle into a photon, $p_{\gamma \rightarrow A} = p_{A \rightarrow \gamma}$, for the same parameters.

The momentum transfer, q , in Equation 1.1 is given by

$$q \approx \omega(n - 1) + \frac{m_A^2}{2\omega}, \quad (1.2)$$

where n is the refractive index of the medium in which the light is propagating, and the form factor, $F(qL)$, is determined by the specifics of the magnetic field [6]. For a uniform magnetic field [6],

$$|F(qL)| = \left| \frac{2}{qL} \sin\left(\frac{qL}{2}\right) \right|, \quad (1.3)$$

making the probability of oscillation

$$p_{\gamma \rightarrow A} = \frac{\omega}{\sqrt{\omega^2 - m_A^2}} \left(\frac{g_{A\gamma\gamma} B}{q} \right)^2 \sin^2\left(\frac{qL}{2}\right). \quad (1.4)$$

Equation 1.4 shows that a larger magnetic field and a longer length of interaction (so long as $qL < \pi$) both couple into the probability. However, when $qL/2$ is large enough that the \sin^2 term stops increasing, the probability begins decreasing as length increases. At the extreme when $qL/2 = N\pi$, where N is an integer, the net probability of oscillation drops to 0.

Most experiments to detect axion-like particles use this oscillation of axion-like particles into photons in the presence of an external magnetic field. These experiments can be put into three different categories: helioscopes, haloscopes, and light-shining-through-a-wall experiments.

Helioscopes seek to detect the axion-like particles generated by the sun and focus on oscillating them into photons. These experiments include CAST [7], the upcoming IAXO [8], and others.

Haloscopes look for axion-like particle emissions from the galactic halos. In these experiments, the dark matter axion-like particles from the galactic halos oscillate into photons that would be detected by these experiments. They include ADMX [9], ORGAN [10], HAYSTAC [11], ABRACADABRA [12], the upcoming MADMAX [13], and others.

Both helioscopes and haloscopes operate only as detectors of externally-generated axion-like particles [14], and therefore depend strongly on models of their sources. Helioscopes rely on models that describe the rate at which the sun produces axions, while haloscopes rely on models for galactic halo production of axions. The significant disadvantage of both of these approaches is that any flaws in models affecting the rate of axion production will be indistinguishable from a different reconversion probability.

Light shining through a wall (LSW) experiments are independent of source models, because they both produce and re-convert axions in the laboratory. The principle is that there is a generation section which produces the axion-like particles by the interaction of

photons with a magnetic field. There is then placed a wall that prevents the transmission of photons, but allows the weakly-interacting axion-like particles to pass. On the other side of the wall, there is a magnetic field that oscillates the axion-like particles into photons [15].

There have been a number of LSW experiments starting with BFRT [16]. After an anomalous result was reported by the PVLAS group in their experiment searching for vacuum polarization effects that could be explained by axion-like particles [17], a number of LSW experiments were attempted to demonstrate that axion-like particles could explain this result, though the anomalous result was not able to be replicated [18]. These new LSW experiments included GammeV [19], two experiments performed by the BMV collaboration [20, 21], OSQAR [22], CROWS [23], and ALPS I [24].

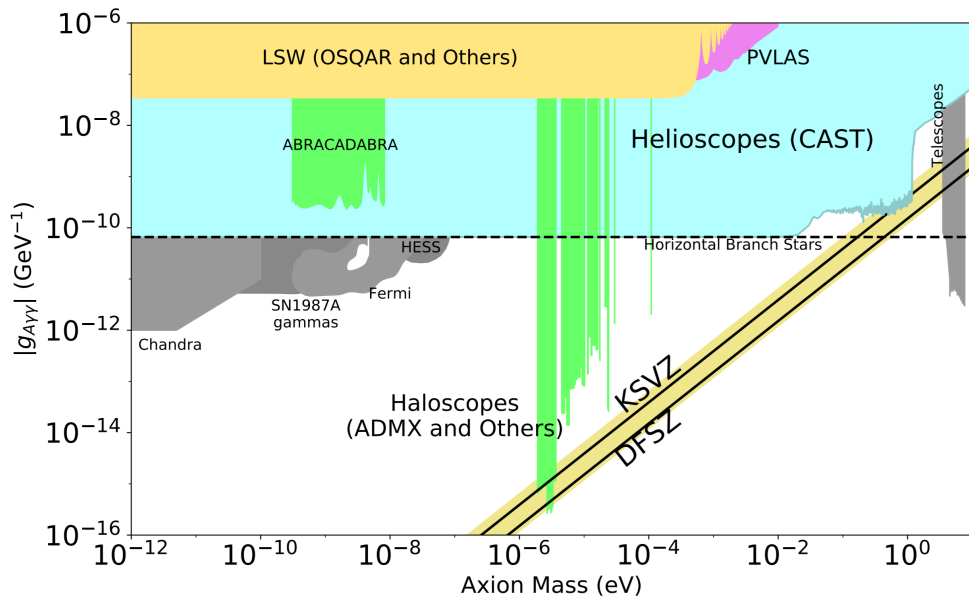


Figure 1.1.: Exclusion plot of axion-like particle experiments [1].

A number of parameters drive the photon to axion-like particle oscillation, as well as the reverse process. Some of these parameters, such as $g_{A\gamma\gamma}$ and m_A , are inherent to the axion-like particle, and some are determined by the experimental or environmental parameters. By combining the experimental and environmental parameters, we can determine the axion-like particle parameters that are excluded by experiment or observation. These regions excluded by experiment are those that would have resulted in a detection of axion-like particles. The regions excluded by observation are those where an observation was made where axion-like particles in those parameter regions would have yielded an anomalous measurement, but no anomaly was seen. These regions are shown in Figure 1.1 [1]. The regions of color are regions excluded by the experiments written on the text. For example, the green regions are regions excluded by haloscopes, the blue regions are excluded by helioscopes, and the darker yellow region is excluded by

LSW experiments. The gray regions are those excluded by other observations. Finally, the lighter yellow with the two parallel lines are the regions that are predicted for the QCD axion.

As ALPS II is an LSW experiment, it is important to understand how LSW experiments are sensitive to experimental and axion-like particle parameters. The probability of a photon oscillating into an axion-like particle, crossing the wall, and then oscillating back into a photon is given by

$$p_{LSW} = p_{\gamma \rightarrow A}(L_g, B_g, \dots) p_{A \rightarrow \gamma}(L_r, B_r, \dots), \quad (1.5)$$

where L_g, B_g, \dots and L_r, B_r, \dots are the length, magnetic field strength, etc. of the generation and regeneration side of the experiment [25]. As such, the number of photons detected in such an experiment, N_{LSW} is given by

$$N_{LSW} = \frac{P_0}{\omega} \cdot \Delta t \cdot p_{LSW} \cdot \eta, \quad (1.6)$$

where P_0 is the power incident on the generation side, Δt is the data collection time, and η is the detector efficiency [25]. Section 1.2 will focus on one of the major ways to enhance this number.

1.2. Any Light Particle Search

ALPS II [26] is a planned successor to ALPS I that builds on the major innovation of ALPS I over previous LSW experiments: optical cavities. Equation 1.6 includes the power on the generation side of the experiment. As such, by increasing the number of photons on the generation side using a production cavity (PC), it should be clear that the number of photons oscillating into axion-like particles should increase. This concept has been discussed for many years [27, 28, 29], and also introduces the idea that experiments can benefit additionally from a resonator on the regeneration side in a regeneration cavity (RC). This resonator enhances the electric field from any axion-like particles that pass through this resonator and thus increases the axion-photon conversion. In this case, Equation 1.6 becomes

$$N_{LSW} = \beta_g \cdot \frac{P_0}{\omega} \cdot \Delta t \cdot p_{LSW} \cdot \beta_r \cdot \eta, \quad (1.7)$$

where β_g and β_r are the enhancement factors due to the use of optical cavities on the generation and regeneration side, respectively [25].

ALPS IIc plans to increase p_{LSW} by using 12 superconducting HERA magnets on each side of the wall to generate a large magnetic field over a long length [30]. These magnets generate a magnetic field of 5.3 T, but there are gaps in this magnetic field where consecutive magnets are connected. This modifies the form factor, $|F(qL)|$, from that given in Equation 1.3 to

$$|F(qL)| = \left| \frac{2}{qL} \sin\left(\frac{qL}{2N}\right) \frac{\sin\left(\frac{qN}{2} \left[\frac{L}{N} + \Delta\right]\right)}{\sin\left(\frac{q}{2} \left[\frac{L}{N} + \Delta\right]\right)} \right|, \quad (1.8)$$

where N is the number of magnets (in the ALPS IIc case, this is 12), Δ is the gap between the magnets, and L is only the length of magnetic field interaction, given by Nl , where l is the magnetic field length of each magnet [6, 26].

A simplification can be made in that both the generation and regeneration side of the ALPS IIc experiment will be identical. As such, $p_{\gamma \rightarrow A} = p_{A \rightarrow \gamma} = p$, meaning that $p_{LSW} = p^2$. Additionally, we can make the simplifications that the system will be in vacuum, so the refractive index, n , is 1, and that the photon energy is significantly larger than the mass of the axion-like particle, $\omega \gg m_A$. This reduces the momentum transfer, q , from the expression given in Equation 1.2 to

$$q \approx \frac{m_A^2}{2\omega}, \quad (1.9)$$

and $\omega/\sqrt{\omega^2 - m_A^2}$ to 1. $|F(qL)|$ can be further simplified by assuming $q = m_A^2/2\omega \ll 1$, which is true for the very small masses for which ALPS IIc will be most sensitive. This assumption makes $\sin(qL/2N) \approx qL/2N$ (N is an integer that is always ≥ 1), and $\sin(qL/2 + qN\Delta/2) \approx qL/2 + qN\Delta/2$, since $\Delta N < L$, leading to

$$|F(qL)| = \left| \frac{2}{qL} \left(\frac{qL}{2N}\right) \frac{\frac{qN}{2} \left(\frac{L}{N} + \Delta\right)}{\frac{q}{2} \left(\frac{L}{N} + \Delta\right)} \right| \approx 1 \quad (1.10)$$

Thus, the probability of oscillation on both the generation and regeneration side becomes

$$p_g = p_r = \frac{(g_{A\gamma\gamma}BL)^2}{4}. \quad (1.11)$$

When combined with Equation 1.7, we can get the full equation for the number of photons detected after the wall as

$$N_{LSW} = \beta_g \cdot \frac{P_0}{\omega} \cdot \Delta t \cdot \frac{(g_{A\gamma\gamma}BL)^4}{16} \cdot \beta_r \cdot \eta. \quad (1.12)$$

The final piece is that the target is not necessarily a number of photons, but a desired signal-to-noise-ratio (SNR). In this instance, the background rate must be included. When considering the SNR that is primarily background and shot-noise limited, we see that the SNR increases as the square root of the integration time, and inversely proportional to the square root of the background rate, while remaining proportional to the other signal strength parameters. The equation for SNR of an LSW experiment is

$$SNR_{LSW} = \beta_g \cdot \frac{P_0}{\omega} \cdot \frac{(g_{A\gamma\gamma}BL)^4}{16} \cdot \beta_r \cdot \eta \cdot \sqrt{\frac{\Delta t}{n_b}} \quad (1.13)$$

This can be re-arranged to solve for the sensitivity of an LSW experiment to the axion-like particle coupling parameter, $g_{A\gamma\gamma}$

$$g_{A\gamma\gamma} = \frac{1}{\beta_g^{1/4}} \cdot \frac{\omega^{1/4}}{P_0^{1/4}} \cdot \frac{2}{BL} \cdot \frac{1}{\beta_r^{1/4}} \cdot \frac{n_b^{1/8}}{\eta^{1/4} \Delta t^{1/8}}. \quad (1.14)$$

In this case, a smaller $g_{A\gamma\gamma}$ is an experiment sensitive to weaker couplings. Since $g_{A\gamma\gamma}$ appears in the probability as the fourth power, most experimental parameters do not couple in more than to the 1/4 power. The main exception to this is the magnetic length, BL , which couples linearly. Therefore, it is strongly desirable to increase the length and the magnetic field of the experiment as much as possible. This is the reason that it is planned to use the 12 superconducting dipole magnets covering optical cavities of 124.4 m. A schematic of the ALPS IIc experiment is shown in Figure 1.2 with the PC on the left containing photons that will oscillate into axion-like particles in the magnetic field provided by the 12 magnets and the RC on the right where the axion-like particles oscillate back into photons in the magnetic field provided by a further 12 magnets.

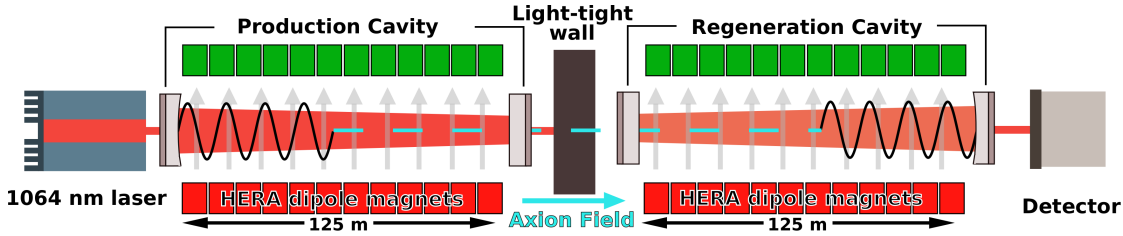


Figure 1.2.: Schematic diagram of the ALPS II experiment. There are two optical cavities. One cavity is a production cavity with photons from an input laser circulating to generate axion-like particles. The other cavity is a regeneration cavity to enhance the oscillation the axion-like particles back into photons before being sent to a detector. Each cavity is inside 12 superconducting HERA dipole magnets. Adapted from [31].

One final design feature in ALPS IIc is the detection system. Two independent detection concepts will be used. The first one that will be implemented uses the interference between a local oscillator and the photon field generated by the axion-like particles to generate a heterodyne signal at the frequency difference between the two fields [26, 32]. The other system implemented will be one that detects re-converted photons using a transition edge sensor (TES). The transition edge sensor works by thermally coupling a photon absorber to a superconducting material that is maintained on the transition edge of superconductivity, and therefore any thermal change due to photon absorption causes a detectable change in the resistance of the material [26].

The next step is to calculate β_g and β_r . This will allow us to calculate the projected sensitivity of the ALPS IIc experiment. The calculation of the enhancement of the signal due to optical cavities requires a description of how optical cavities enhance electric fields.

1.3. Optical Cavities

The majority of this section parallels the more detailed presentation of the ideas, derivations, and equations presented in Chapter 11 of [33].

Optical beams are three dimensional. However, optical cavities can be explained almost entirely in one dimension: the direction of propagation. In this approximation, we can use plane waves. These plane waves are infinite and flat in x and y , propagate along the z direction, and are polarized in the x direction, given by the equation

$$\vec{E}(z, t) = E_0 e^{i(\omega t - \vec{k} \cdot \vec{z})} \hat{x}, \quad (1.15)$$

where E_0 is the magnitude of the plane wave, ω is the angular frequency of the optical wave, \hat{x} is the unit vector in the x direction, and \vec{k} is the wave vector given by

$$\vec{k} = \frac{2\pi}{\lambda} \hat{z} = \frac{2\pi n}{\lambda_0} \hat{z}, \quad (1.16)$$

where \hat{z} is the unit vector in the z direction. Since \vec{k} is parallel to \vec{z} , we can treat them both as scalars. Additionally, as the polarization is not relevant in this approximation, we can treat the electric field as scalar. Applying these simplifications, the electric field becomes

$$E(z, t) = E_0 e^{i(\omega t - kz)}. \quad (1.17)$$

Optical cavities are made of at least two mirrors that allow light to circulate between them. If the light from every round trip is in-phase and constructively interferes, then the optical power in the cavity can build up to be much larger than the input power. ALPS II uses linear cavities made up of only two mirrors where the light propagates entirely along one line, such as the ALPS IIa Regeneration Cavity (RC) shown in Figure 1.3.

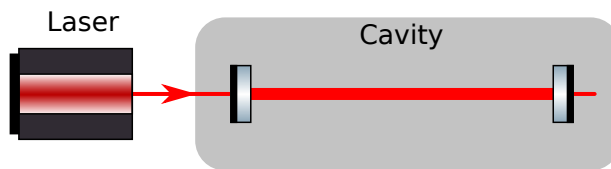


Figure 1.3.: A schematic diagram of an input laser and the ALPS IIa Regeneration Cavity. This is a linear cavity with the light circulating between two mirrors in line with the input light from the laser.

In these linear cavities, the round-trip length of the cavities is $2L$, where L is the distance between the two mirrors. The mirrors used in these cavities are not perfectly reflective, but instead allow some light to be transmitted through. For an electric field propagating through vacuum and encountering an interface, the reflected field is given by

$$E_{refl} = \frac{1-n}{1+n} E_0. \quad (1.18)$$

The mirrors used in ALPS IIa and IIc are made by depositing many layers of dielectric materials onto a transmissive surface to end up with a very large effective refractive index. After these mirrors, the reflected field is given by

$$E_{refl} = -\sqrt{R}E_0, \quad (1.19)$$

where R is the power reflectivity given by

$$R_{mirror} = \left| \frac{(1 - n_{mirror})}{(1 + n_{mirror})} \right|^2 \quad (1.20)$$

As Equation 1.18 is for light propagating in vacuum and interacting with a surface with a larger refractive index, Equation 1.19 that follows from it is only true for this situation. For surfaces that have a lower refractive index than the propagation medium, there is no $\pi/2$ phase shift of the light on reflection. Neglecting mirror losses, this power reflectivity is related to the power transmissivity, T by

$$R + T = 1. \quad (1.21)$$

In addition to the magnitude change from reflection, there are additional losses such that the magnitude of the light in a cavity with perfect reflectors after one round trip would be given by

$$E = E_0 e^{-\alpha}, \quad (1.22)$$

where α is the net loss coefficient and includes scattering losses from the mirror surfaces, as well as losses that accrue from propagation through the cavity. All of these effects combine to give us the equation after each round trip to be

$$E_{rt} = \sqrt{R_1 R_2} E_0 e^{-\alpha} e^{-i2kL}, \quad (1.23)$$

where R_1 and R_2 are the power reflectivities of the first and second mirror, respectively. The change in magnitude of one round trip can be combined into the round trip gain, g_{rt} given by

$$g_{rt} = \sqrt{R_1 R_2} e^{-\alpha}. \quad (1.24)$$

The final factor to consider is the amount of light that couples into the cavity. This is given by the transmission of the first mirror

$$E_{cav} = \sqrt{T_1} E_{in} \quad (1.25)$$

In steady state operation, where the cavity length, wavelength of the light, and power in the cavity are stable, the circulating field, E_{circ} remains constant. In order to achieve this constant field, the changes to the circulating field from one round trip are exactly

offset by the field that is coupled into the cavity. This includes both the amplitude and the phase. This gives us the recursive relationship

$$E_{circ} = \sqrt{T_1}E_{in} + \sqrt{R_1R_2}e^{-\alpha}e^{-i2kL}E_{circ}, \quad (1.26)$$

which can be re-arranged to give us a relationship between the input field and the circulating field

$$\frac{E_{circ}}{E_{in}} = \frac{\sqrt{T_1}}{1 - g_{rt}e^{-2ikL}}. \quad (1.27)$$

In this equation E_{circ} is much larger when $2kL = 2\pi q$ where q is an integer, as when this condition is met, $e^{-2ikL} = 1$. The circulating field at that point becomes

$$\frac{E_{max}}{E_{in}} = \frac{\sqrt{T_1}}{1 - g_{rt}} = \frac{\sqrt{T_1}}{1 - \sqrt{R_1R_2}e^{-\alpha}} \quad (1.28)$$

Since the field is related to power by $P \propto |E|^2$, the power build-up in the cavity becomes

$$\frac{P_{max}}{P_{in}} = \frac{|E_{max}|^2}{|E_{in}|^2} = \frac{T_1}{(1 - g_{rt})^2}. \quad (1.29)$$

This power build-up happens when the cavity is resonant with the input light. That is, when the length of the cavity is related to the wavelength by the following equation

$$L_{peak} = \frac{q\lambda_0}{2n}, \quad (1.30)$$

or when the wavelength matches the cavity, which is often more convenient to write in terms of frequency where $f = c/\lambda_0$ and c is the speed of light in a vacuum

$$f_{peak} = \frac{qc}{2nL}. \quad (1.31)$$

From this equation, we can see that the resonant frequency is inversely proportional to length. If we take the derivative of the resonant frequency with respect to length to see what the behavior is for small changes, we see that

$$\frac{df_{peak}}{dL} = -\frac{qc}{2nL^2}. \quad (1.32)$$

For small changes, $\Delta L \ll L$, we can assume that the right side is constant, and thus substitute in the difference in for the differential to get

$$\Delta f_{peak} = -\frac{\Delta L}{L} \frac{qc}{2nL}, \quad (1.33)$$

and then combined with the result of Equation 1.31 and get that.

$$\frac{\Delta f_{peak}}{f_{peak}} = -\frac{\Delta L}{L}. \quad (1.34)$$

Another important relationship is that of successive resonances. It is clear from Equation 1.31 that the the frequency difference between these resonances, also known as axial modes, is given by

$$f_{FSR} = \frac{c}{2nL}. \quad (1.35)$$

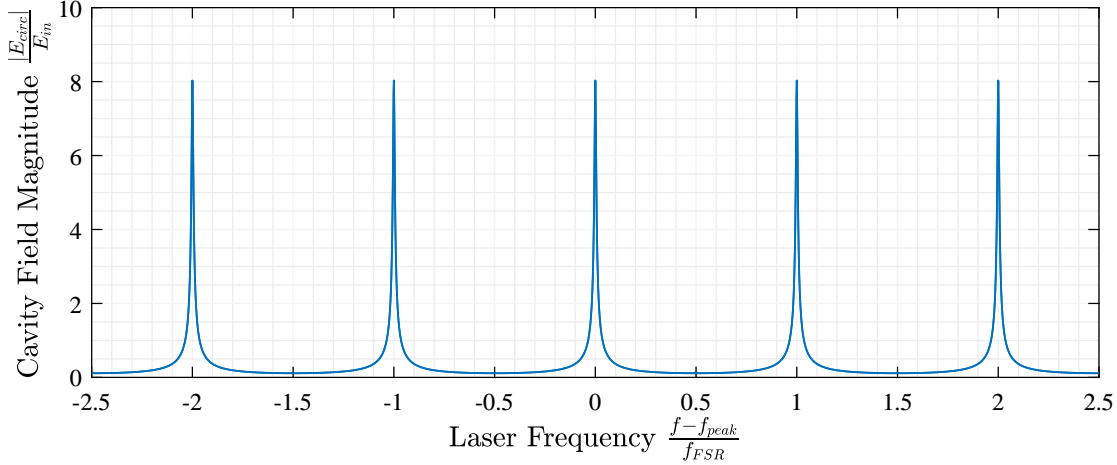


Figure 1.4.: Axial cavity modes where $T_1 = 0.05$, $T_2 = 0.005$, $\alpha = 2 \times 10^{-4}$ corresponding to approximately 200 ppm of losses. The resulting power build-up $P_{max}/P_{in} = 64$. The resonances occur periodically in frequency with a spacing given by f_{FSR} .

This spacing is also referred to as the free spectral range (FSR). This spacing in an example cavity can be seen in Figure 1.4. In addition to the FSR, it is important to know the bandwidth of the resonance. One way to measure this is the frequency over which the power is at least 1/2 of the maximum, which gives

$$\Delta f_{peak} = \frac{2c}{\pi nL} \sin^{-1} \left(\frac{1 - g_{rt}}{2\sqrt{g_{rt}}} \right) \approx \frac{c}{2nL} \left(\frac{1 - g_{rt}}{\pi\sqrt{g_{rt}}} \right) = \left(\frac{1 - g_{rt}}{\pi\sqrt{g_{rt}}} \right) f_{FSR}, \quad (1.36)$$

which is also known as the full width at half maximum (FWHM).

The final cavity parameter to consider in the Finesse (\mathcal{F}) of a cavity. Historically, it was used to calculate the resolving power of an etalon, but is still used for calculations and as a derived cavity parameter. It is given by the equation

$$\mathcal{F} \equiv \frac{\pi\sqrt{g_{rt}}}{1 - g_{rt}} \approx \frac{f_{FSR}}{\Delta f_{peak}}. \quad (1.37)$$

Finesse is can be more useful than the FWHM because the the FWHM scales with the FSR. The finesse is largely independent of cavity length and depends only on the mirror properties as well as other cavity losses. In the example cavity in Figures 1.4 and 1.5, $\mathcal{F} = 110$.

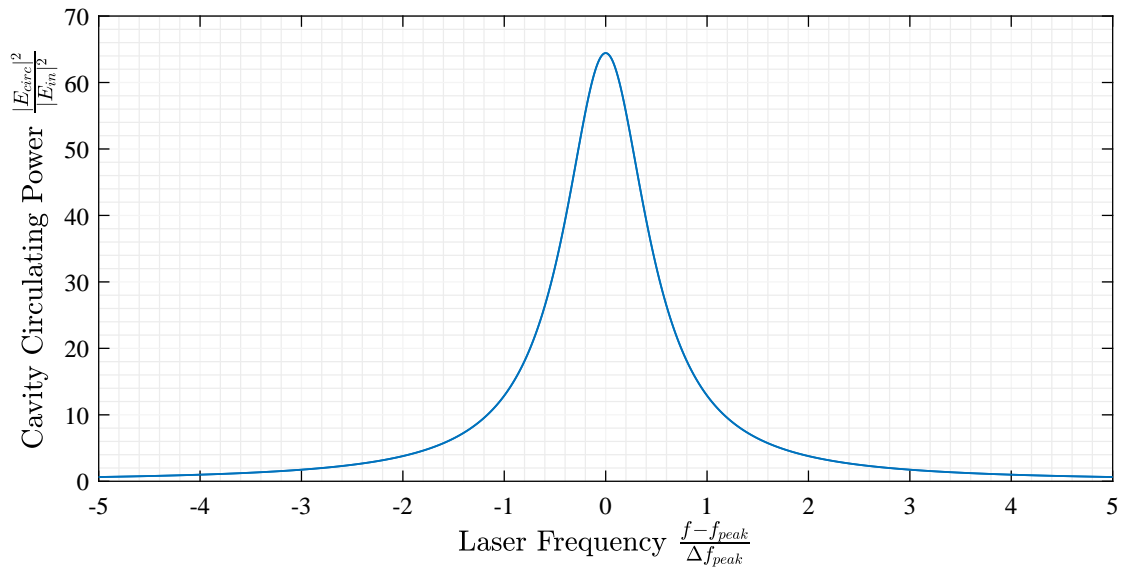


Figure 1.5.: Magnified resonance of a cavity with the same parameters as Figure 1.4. The offset from the resonance peak is given in terms of the cavity full width at half maximum.

1.4. Cavity Field Sensing

A discussion of how controls can be used to maintain cavity resonance, or any condition desired, is found in Chapter 2. One of the most important part of controls is the sensing method that would, in effect, tell the control system how the cavity and laser were away from the resonance condition. With this information, the control system could apply the appropriate corrections. This signal is known as the error signal, since it describes the system's ‘error’ away from a perfect resonance condition.

What is clear in Figure 1.5 is that the resonance is that the power changes in the same direction as the frequency moves off of the resonance, regardless of the direction of the frequency change. Additionally, the power contained within the cavity is dependent on the input power. Therefore, any attempt to use the power in the cavity to generate an error signal would not be able to determine in what direction the frequency (or cavity resonance) was moving when very close to the resonance, and any changes to the input power would be indistinguishable from changes in power due to changes in the resonance condition. Thus, it is important to use a method that both gives us knowledge of the direction of the error and largely decouples the error signal from the input power.

The solution to this problem is to introduce radio frequency (RF) phase modulation sidebands and compare the sidebands to the center band, which will be resonant or nearly resonant in the cavity, in a heterodyne technique [34], which has also been used in microwave oscillators [35]. This technique is known as Pound-Drever-Hall (PDH) and is used extensively in gravitational wave detectors [36] and other laser stabilization

systems [37]. An introduction to the technique can be found in [38], and the following section will mostly follow the explanations and derivations presented in that reference.

The generation of the sidebands is accomplished by applying a voltage oscillating at a certain frequency to an Electro-Optic Modulator (EOM). These devices use the Pockels effect whereby a voltage applies a phase change that is linearly proportional to the applied voltage [39]. The incident electric field is changed from that in Equation 1.17 to

$$E_{in} = E_0 e^{i(\omega t - kz + \beta \sin(\Omega t))}. \quad (1.38)$$

At this point, it becomes convenient to define the input to the cavity to be the origin, such that $z = 0$ for the input field, and we get the simpler version

$$E_{in} = E_0 e^{i(\omega t + \beta \sin(\Omega t))}. \quad (1.39)$$

This can be expanded in terms of Bessel functions where

$$E_{in} \approx E_0 [J_0(\beta) e^{i\omega t} + J_1(\beta) e^{i(\omega + \Omega)t} - J_1(\beta) e^{i(\omega - \Omega)t}]. \quad (1.40)$$

In this case, we have three parts of the beam: the un-modulated center band, one band at the sum frequency, and one band at the difference frequency. There are higher-order harmonics, but when $\beta \ll 1$, these are much smaller and can usually be ignored.

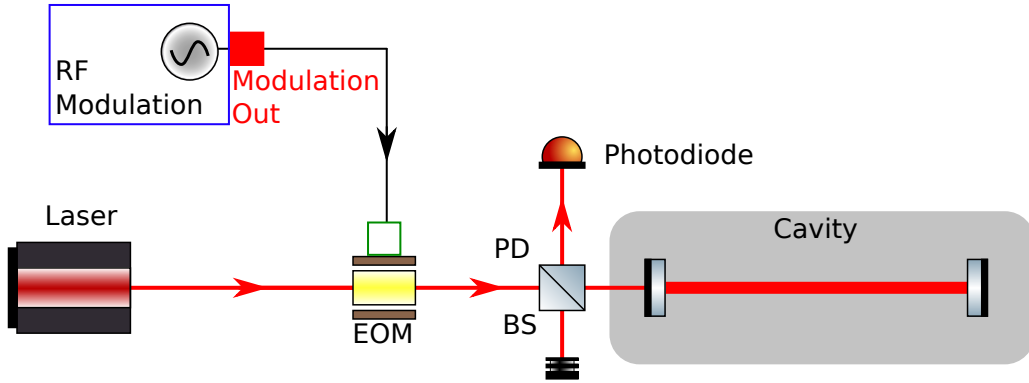


Figure 1.6.: A schematic diagram of an input laser with modulation sidebands, a beamsplitter and photodetector to sense the light reflected from the cavity, and the optical cavity. This is a simplified version of the optical setup used for PDH.

The three parts of the beam each interact with the cavity separately. The reflected beam is both the sum of the portion of the beam that is initially reflected off of the cavity mirror as well as a portion of that which is circulating inside the cavity. Because of this mixing of the reflected incident fields and the transmitted circulating cavity field, we are most interested in the signal in reflection of the cavity. Because of this, the experimental setup will look like Figure 1.6.

The cavity field exiting the input mirror is the cavity circulating field given in Equation 1.26 after propagation through the cavity excluding reflection from the input mirror.

Because of this, it is modified by the g_{rt} except for the input mirror reflectivity, as it is instead affected by the input mirror transmissivity. The reflected field for a given beam is

$$E_{refl} = -\sqrt{R_1}E_{in} + \frac{\sqrt{T_1}g_{rt}}{\sqrt{R_1}}E_{circ}. \quad (1.41)$$

This combined with Equation 1.27 gives us the ratio between the incident field and the combination of the promptly reflected beam and the circulating field that is transmitted through the input mirror as

$$\frac{E_{refl}}{E_{in}} = \frac{T_1}{\sqrt{R_1}} \frac{g_{rt}}{1 - g_{rt}e^{-2i\omega L/c}} - \sqrt{R_1} = F(\omega). \quad (1.42)$$

It is important to note that $F(\omega)$ does have a frequency (relative to cavity length) dependence, and is therefore different for the three different input beams in Equation 1.40. With these two equations, we get the full reflected field as

$$E_{refl} = E_0[F(\omega)J_0(\beta)e^{i\omega t} + F(\omega + \Omega)J_1(\beta)e^{i(\omega+\Omega)t} - F(\omega - \Omega)J_1(\beta)e^{i(\omega-\Omega)t}]. \quad (1.43)$$

However, we are not able to directly detect the field of the reflected signal. Instead we detect the voltage coming from the photodetector, which is proportional to the power incident on the photodetector. For this reason, the reflected power is measured and given by

$$P_{refl} \propto |E_0|^2 (\text{DC terms} + 2J_0(\beta)J_1(\beta) [\Re(F(\omega)F^*(\omega + \Omega) - F^*(\omega)F(\omega - \Omega)) \cos(\omega t) \\ + \Im(F(\omega)F^*(\omega + \Omega) - F^*(\omega)F(\omega - \Omega)) \sin(\omega t)] \\ + 2\Omega \text{ terms}), \quad (1.44)$$

where we have both a sine and a cosine term that are oscillating at Ω . This signal is first sent through a bandpass filter to eliminate both the DC and 2Ω terms. Then, in order to extract envelope of the terms oscillating at Ω , we send the signal resulting from the bandpass filter through a mixer, which multiplies the signals. Multiplying two oscillating signals with an arbitrary phase offset give us

$$\sin(\Omega t) \sin(\Omega' t + \phi) = \frac{1}{2} \cos(\phi) (\cos([\Omega + \Omega'] t) - \cos([\Omega - \Omega'] t)) \\ + \frac{1}{2} \sin(\phi) (\sin([\Omega + \Omega'] t) + \sin([\Omega - \Omega'] t)). \quad (1.45)$$

If we consider that $\Omega \approx \Omega'$, then we see that we would have one term oscillating at 2Ω and another at nearly DC. This DC part is the most interesting, and the 2Ω part can be eliminated with a low-pass filter. When $\phi = 0$, we see that only the cosine terms remain, in which the near-DC terms are multiplied by 1. On the other hand, if $\phi = \pi/2$, then we get only the sine terms remaining and the near-DC terms are multiplied by 0.

Since it is important to maximize the near-DC part of this signal, aligning the phase is critical. This can either be accomplished using a delay line, or by adjusting the phase offset of the signals as they are being generated.

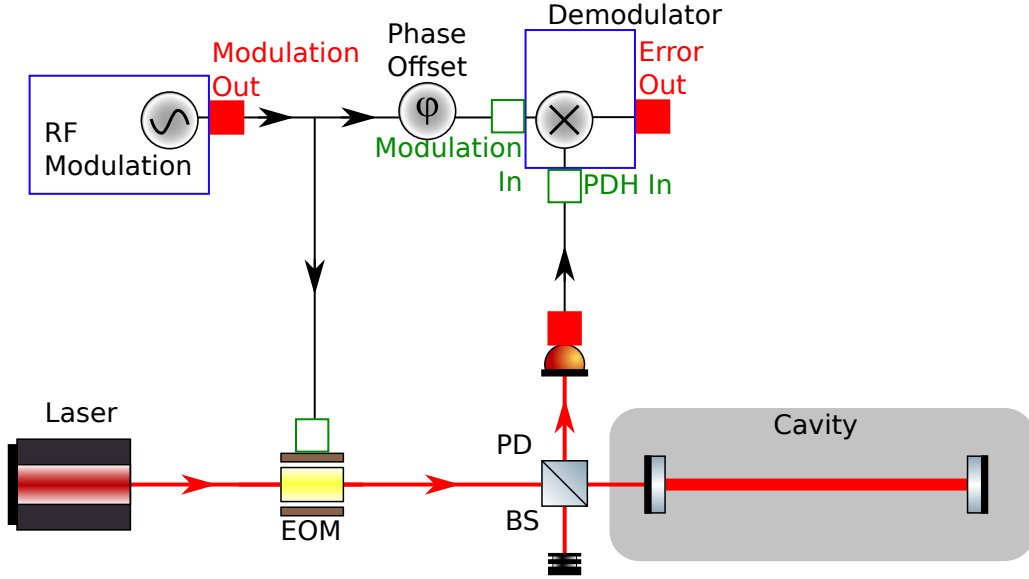


Figure 1.7.: A schematic diagram building on the generation of PDH signals in Figure 1.6 with the addition of a demodulator. This demodulator extracts the desired interference between the center and side bands.

We also see with this that the two different terms oscillating at Ω are $\pi/2$ out of phase, which means that we can only look at one term at a time. So we must further evaluate which of the two is most important. When we consider an oscillation frequency that is much larger than the FWHM of the cavity and the center band is on-resonance, we see that the sidebands are almost entirely made up of light reflected by the first surface and contain almost no contribution from light that has interacted with the cavity. Though the cavity in Figure 1.4 has an input mirror transmission of 5%, they are typically measured in the tens or hundreds of parts per million (ppm), resulting in a reflection very close to unity. As such, $F(\omega + \Omega)$ and $F(\omega - \Omega)$ are both approximately -1. With this knowledge, we see that

$$\begin{aligned} \Re(F(\omega)F^*(\omega + \Omega) - F^*(\omega)F(\omega - \Omega)) &\approx -\Re(F(\omega) - F^*(\omega)) = 0 \\ &\text{and} \\ \Im(F(\omega)F^*(\omega + \Omega) - F^*(\omega)F(\omega - \Omega)) &\approx -\Im(F(\omega) - F^*(\omega)) = -2\Im(F(\omega)). \end{aligned} \tag{1.46}$$

This means that sine term from Equation 1.44 is much larger than the cosine term, and we should therefore align our signals in the mixer to choose that term. This leaves us with the signal after demodulation and low-pass filtering as

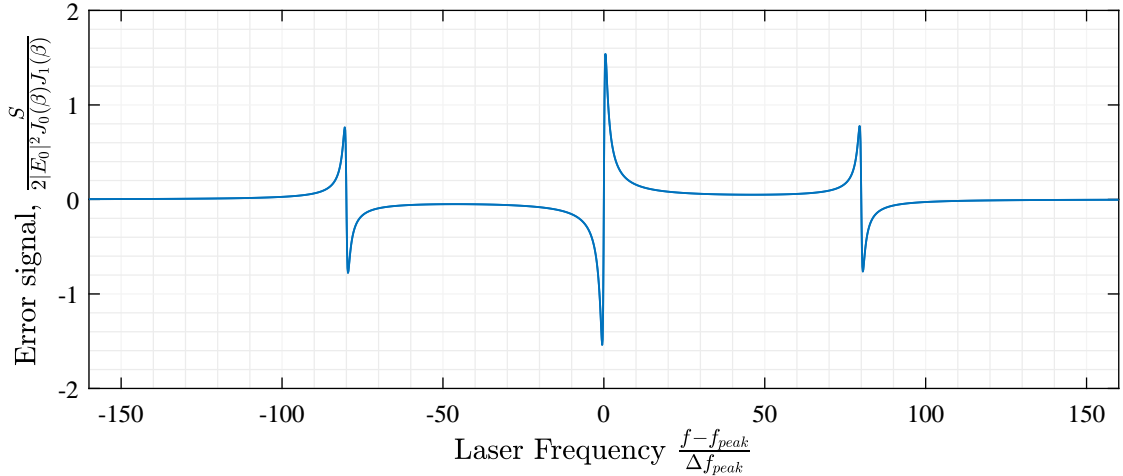


Figure 1.8.: An example of a Pound-Drever-Hall error signal when changing the input laser frequency with respect to the resonance frequency of the cavity. The Finesse for this example is 4,800 leading to a linewidth of $\approx 0.02\%$ of the axial mode spacing. The modulation frequency is 80 times the linewidth.

$$S \propto -2|E_0|^2 J_0(\beta) J_1(\beta) \Im (F(\omega) F^*(\omega + \Omega) - F^*(\omega) F(\omega - \Omega)). \quad (1.47)$$

When scanning over a resonance, an example of this error signal can be seen in Figure 1.8. The largest response is when the center band is close to resonance, while the side bands give a smaller response that is opposite in direction. The error signal near resonance of the same cavity is shown in Figure 1.9. The signal within the FWHM of the resonance peak is very close to linear, which makes control in that region much easier.

1.5. Use of Optical Cavities in ALPS II

The theory behind optical cavities make it possible to describe the enhancement factors, β_g and β_r , discussed in Section 1.2. Each is related to the build-up in electric field for the PC and RC, as the electric field is the most important parameter, but the source of each electric field is slightly different.

The source of the electric field in the PC is clear: laser input. As such, the electric field and power build-up is given by Equation 1.29. This takes into account the light from the input coupling into the cavity and then building up into a large number of photons that can oscillate into axion-like particles. One can also consider the full factor of $\beta_g P_0$ to be the power circulating in the cavity.

The enhancement factor in the RC, β_r , is a little different. Because the electric field enters the cavity as an axion-like particle, the input coupler can be considered to be completely transmissive. Then, the electric field can build up as it oscillates between the mirrors before being coupled out. As such, the enhancement factor starts the same

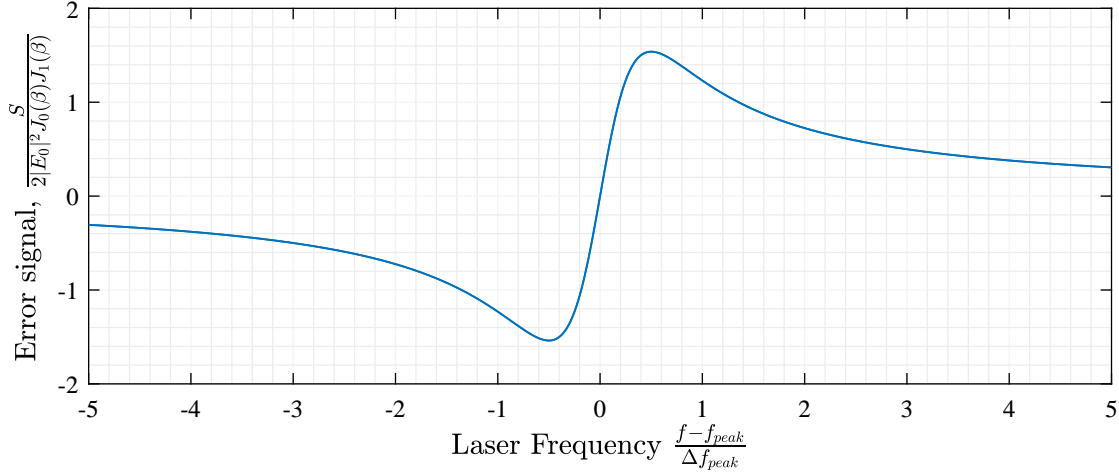


Figure 1.9.: A close-up view of the Pound-Drever-Hall signal in Figure 1.8 near the center band resonance. The signal is approximately linear within the FWHM of the resonance peak.

as with the production cavity, but assuming the input coupler has a transmission of 1. That makes the power build-up inside the cavity

$$\frac{P_{max}}{P_{in}} = \frac{1}{(1 - g_{rt})^2}, \quad (1.48)$$

which gives us the power build up in the cavity right after the mirror closest to the light tight wall. In order to determine how much of this power exits the cavity to the detection system, we need to identify how the light exits the cavity. For the case of ALPS IIc, it is different for each detection system. For the heterodyne detection, the mirror furthest away from the wall is the output coupler (M2), and for the TES system, the mirror closest to the light tight wall is the output coupler (M1). For the heterodyne system, this means taking the built up power in Equation 1.48 and coupling it out through the second mirror, that is

$$\frac{P_{out}}{P_{in}} = \frac{T_2}{(1 - g_{rt})^2}. \quad (1.49)$$

which is the enhancement of the power due to the axions generated in the PC for the heterodyne system.

For the TES system, we can multiply the circulating power by the full round trip gain except for the reflection of the first mirror. This entails multiplying the power-build up by $R_2 e^{-2\alpha}$, which is the same as g_{rt}^2 / R_1 . This gives us the power moving towards the first mirror but right before it. To determine how much exits the cavity, we multiply it by the transmission of the first mirror, T_1 , to give

$$\frac{P_{out}}{P_{in}} = \frac{T_1 g_{rt}^2}{R_1 (1 - g_{rt})^2}, \quad (1.50)$$

which is the enhancement of the power due to the axions generated in the PC for the TES system.

These power build-up equations are all for light that is perfectly resonant with the cavity. In real-world experiments, perfect resonance is impossible. As such, it is important to calculate the power build-up given imperfect matching between the resonance and the laser light. For variations in the frequency that are small compared to the free spectral range of the cavity, this is given by

$$\frac{P_{out}}{P_{in}} = \frac{P_{out,max}}{P_{in}} \frac{1}{1 + \left(\frac{2\mathcal{F}}{\pi}\right)^2 \sin^2\left(\frac{\pi f}{f_{FSR}}\right)} \quad (1.51)$$

where $P_{out,max}$ is the maximum power output for a cavity perfectly on resonance [40]. One can simplify this by assuming the laser is relatively close to a resonance, that is to say

$$\begin{aligned} \frac{\pi f}{f_{FSR}} &= q\pi + \frac{\pi \delta f}{f_{FSR}} \quad \text{and} \\ \pi \delta f &\ll f_{FSR}, \end{aligned} \quad (1.52)$$

where δf is the small offset between the resonance frequency of the cavity and the frequency of the laser. This allows us to apply the small angle approximation to Equation 1.51 and get

$$\frac{P_{out}}{P_{in}} \approx \frac{P_{out,max}}{P_{in}} \frac{1}{1 + \left(\frac{2\mathcal{F}\delta f}{f_{FSR}}\right)^2} \approx \frac{P_{out,max}}{P_{in}} \frac{1}{1 + \left(\frac{2\delta f}{\Delta f_{peak}}\right)^2}, \quad (1.53)$$

where $P_{out,max}$ is the power output for ideally-resonant light. This gives us the cavity enhancement term, β_g and β_r in terms of the maximum cavity enhancement term, $\beta_{g,max}$ and $\beta_{r,max}$.

The use of optical cavities to resonantly enhance the conversion probability on both sides of the wall introduces an additional parameter: the overlap of the electric fields. When a photon oscillates into an axion-like particle and then back into a photon, the properties of the photon remain the same over the coherence length of the axion-like particle field, which is assumed to be much longer than the experimental setup for the mass region in which ALPS IIc will be sensitive. As such, in order for the electric field to enhance the probability of reconversion, the regeneration cavity needs to be resonant for the light that is circulating in the production cavity. This introduces another parameter, the overlap parameter ξ . This parameter considers the percentage of power lost due to the electromagnetic component of the axion-like particles generated by the PC not being fully resonant in the RC. This considers the spatial overlap of the beams, as well as the frequency relationship. This thesis will be primarily considering the frequency overlap, as all systems discussed are to control the frequency of the cavities.

The requirements for this frequency overlap between the light of the two cavities can be divided into two separate requirements: dynamic variations of the phase between the light in the PC and the resonance in the RC, and a near-static offset due to slow drifts. The dynamic variations between the two cavities can be calculated using the spectrum of the frequency noise between the two cavities as presented in [41] and will be partially reproduced here. In this way, we treat the RC as the reference and determine the spectrum of the PC cavity field, and thus the electromagnetic part of the axion-like field, compared to it. The frequency component of that field, $\omega_a(t)$, is given by

$$\omega_a(t) = \omega_c + 2\pi \sum_k \sqrt{2} A_k^{RMS} \sqrt{df_k} \sin(2\pi f_k t + \phi_k), \quad (1.54)$$

where ω_c is the resonance frequency of the RC, A_k^{RMS} is the spectral density of the frequency noise at discrete frequency bin k , df_k is the size of frequency bin k , f_k is the frequency of bin k , and ϕ_k is the phase. This frequency is then integrated to get the phase. The frequency noise results in a phase modulation of modulation depth β_k in frequency bin k given by

$$\beta_k = \frac{\sqrt{2} \sqrt{df_k} A_k^{RMS}}{f_k}. \quad (1.55)$$

The phase term from the integration is the phase of the electric field circulating in the PC, which is then the input to the RC and the field build-up of the PC field in the RC is given by

$$\frac{E_{circ,RC}(n)}{E_{in,RC}(n)} \approx \sqrt{\frac{P_{circ,max}}{P_{in}}} \left(1 + i \sum_k \frac{\beta_k}{\sqrt{1 + \frac{f_k^2}{f_{cav}^2}}} \cos\left(2\pi f_k \frac{n}{f_{FSR}} + \phi_k\right) \right) e^{i\omega_c t}, \quad (1.56)$$

with $\beta_k \ll 1$. The RC acts as a low-pass filter to an input electric field with the corner frequency of f_{cav} , so that effect is included in the above equation. This corner frequency is given by

$$f_{cav} = \frac{\Delta f_{peak}}{2}. \quad (1.57)$$

When taking the time-averaged power in the cavity, we get

$$\frac{P_{circ}}{P_{in}} = \frac{P_{circ,max}}{P_{in}} \left(1 + \sum_k \frac{\beta_k^2}{2 \left(1 + \frac{f_k^2}{f_{cav}^2}\right)} \right), \quad (1.58)$$

This gives the power output from the cavity with the frequency noise given by β_k . This is then compared to the cavity output power without this frequency noise to determine how much of that power lost due to the noise. This is given by

$$\text{Relative power lost} = \frac{1}{2} \sum_k \beta_k^2 \left(1 - \frac{1}{1 + \frac{f_k^2}{f_{cav}^2}} \right), \quad (1.59)$$

and can be simplified to

$$\text{Relative power lost} = \frac{1}{f_{cav}^2} \sum_k df_k A_k^2 \frac{1}{1 + \frac{f_k^2}{f_{cav}^2}}, \quad (1.60)$$

which shows that the square of the numerically integrated RMS of the frequency spectral density, filtered by the cavity pole contributes to the power loss as a percentage of the cavity pole squared. This can be re-arranged to get the requirement on the RMS of the frequency spectral density after filtering by the pole

$$f_{cav} \sqrt{\text{Relative power lost}} = \sqrt{\sum_k df_k A_k^2 \frac{1}{1 + \frac{f_k^2}{f_{cav}^2}}}. \quad (1.61)$$

In the case of the ALPS IIc cavities where the goal is to keep the loss due to this dynamic frequency noise between the two cavities to less than 4%, or 0.04 relative power loss, the linewidth of both cavities is 30 Hz, this corresponds to a goal of less than 3.0 Hz RMS of dynamic frequency mismatch between the PC and the RC.

The goal for the loss of overlap due to a static offset, η_{offset} , is 0.1% [42]. The δf allowed for that value can be found by re-arranging Equation 1.53 to give

$$\delta f = \sqrt{\frac{1 - \eta_{offset}}{\eta_{offset}}} \frac{\Delta f_{peak}}{2}. \quad (1.62)$$

This gives us a maximum allowed offset of 0.5 Hz.

Name	Variable	Nominal Value	Initial Value
Effective laser power	$\beta_g P_0$	150 kW	150 kW
RC enhancement factor	β_r	40 000	10 000
Photon wavelength	λ	1064 nm	1064 nm
Magnetic length	$B \cdot L$	560 T · m	560 T · m
Background noise	n_b	7.7×10^{-6} Hz	7.7×10^{-6} Hz
Overlap	ξ	0.9	0.9

Table 1.1.: Nominal experimental values for the ALPS IIc experiment [26, 42, 43].

The nominal and initial ALPS IIc parameters are found in Table 1.1. As a note, the detector sensitivity has been generalized to a detector sensitive enough to detect a photon rate of 2.8×10^{-5} Hz with a 95% confidence interval over the integration time. The heterodyne system does not detect individual photons, and therefore the efficiency of a detector for detecting photons is not an effective way to measure its sensitivity.

Thus, it has been replaced by this requirement that is driven by the goals of the system and is a more effective way of specifying both systems than the detection efficiency.

The nominal parameters give a sensitivity of ALPS IIc $g_{A\gamma\gamma} = 2 \times 10^{-11} \text{ GeV}^{-1}$. The sensitivity of the experiment can be calculated by comparing the experimental parameters to their nominal parameters, and therefore calculating the ratio between the nominal value and the actual sensitivity of the experiment, $g_{A\gamma\gamma,s}$ as such

$$g_{A\gamma\gamma,s} = \frac{2 \times 10^{-11}}{\text{GeV}} \frac{1}{|F(qL)|} \left[\frac{560 \text{ T} \cdot \text{m}}{BL} \right] \left[\frac{0.9}{\xi} \right]^{\frac{1}{4}} \left[\frac{150 \text{ kW}}{\beta_g P_0} \frac{40\,000}{\beta_r} \right]^{\frac{1}{4}} \left[\frac{n_b}{7.7 \times 10^{-6} \text{ Hz}} \frac{480 \text{ h}}{\tau} \right]^{\frac{1}{8}}. \quad (1.63)$$

The initial science runs are not planned to reach the nominal parameters, and will thus be a little bit less sensitive to $g_{A\gamma\gamma}$ than the final plan. The power build-up of the RC is planned to be 10 000 instead of the nominal 40 000. This results in a planned initially sensitivity of $g_{A\gamma\gamma,s} = 2.8 \times 10^{-11} \text{ GeV}^{-1}$.

For the production cavity, the input coupler, M1 which is the furthest mirror from the wall, is planned to have a transmission of 100 ppm. The second mirror, M2 which is closest to the wall, is planned to have a transmission of 5 ppm. The cavity is expected to have internal losses primarily from surface scattering of 40–60 ppm [43]. The regeneration cavity will have two mirrors with the same parameters. The heterodyne system will have an RC that is a mirror image of the PC, so M1 will have a transmission of 5 ppm and M2 will have a transmission of 100 ppm. The TES system will be reversed from that, so that M1 will have a transmission of 100 ppm and M2 will have a transmission of 5 ppm. One thing to note is that the detection systems have reversed mirror transmissions to place the higher transmission mirror as the output coupler to the detection system. As such, the output coupler is the 100 ppm transmission mirror in both detection systems. With these mirror parameters, $g_{rt} \approx 1$ and $R_N \approx 1$, so we can see that

$$\frac{T_{2,\text{HET}}}{(1 - g_{rt})^2} \approx \frac{T_{1,\text{TES}} g_{rt}^2}{R_{1,\text{TES}} (1 - g_{rt})^2} \approx 17\,000. \quad (1.64)$$

These parameters also give both cavities a finesse of 40 000. The length corresponds to an FSR of 1.2 MHz. Both the finesse and the length give and a linedwidth of 30 Hz.

In addition to having a different detection layout, each detection scheme has a different control method to achieve the required power build-up and overlap. More information on control systems can be found in Chapter 2, and details about specific control systems can be found in Chapters 3, 4, and 5.

The method for achieving power build-up for PC for both schemes is the same, where the high-power laser (HPL) with an output of up to 70 W and a wavelength of 1064 nm [44] will be matched to the PC cavity resonance by actuating on the frequency of the laser. This laser is an amplifier seeded by a non-planar ring oscillator laser, which is also used for all of the lasers in ALPS II. The power build-up in the PC can be treated independently of the power build-up of the RC and the overlap parameter.

As far as the use of cavities goes, the primary difference between the two detection methods is their approach to the control of the RC. For both systems, the important

consideration for both schemes is to minimize light at exactly the same frequency as the light in the PC in the RC. This is because the light from axion-like particles oscillating into photons are expected to be at exactly that frequency and the light from the two sources would be indistinguishable from each other.

The heterodyne scheme can use 1064 nm light that is slightly different from the PC circulating field provided by a local oscillator laser (LO). This LO is matched to the RC resonance by actuating the frequency. This method cannot be used by the TES system, as this detector is not sufficiently sensitive to the frequency of photons to determine the difference between photons from axion-like particle oscillations and LO field. Instead, it is planned that the resonance of the cavity will be probed using 532 nm that is generated by doubling the frequency of 1064 nm infrared light (IR) from a reference laser (RL). This frequency doubling is done with second-harmonic generation using a medium that supports non-linear optical effects [39]. The cavity properties for the green light at 532 nm are somewhat different from the properties for the infrared light. M1, with its transmission for infrared of 100 ppm, will have a transmission of 5% for green. M2, with 5 ppm transmission for infrared, will have 1% transmission for green. These parameters result in a power build-up of 55, a finesse of 100, and combine with the length to give a linewidth of 12 kHz [43].

In both of these systems, the probe beam contains information about the power build-up in the RC independently of the overlap parameter and of the PC power build-up. This leaves the overlap parameter as the last important specification. This is where matching the resonance of both cavities becomes important. For both systems, this matching is done by actuating on the length of the PC so the resonance frequency of that cavity is adjusted such that the light circulating in that cavity is resonant with the RC. Each system has a slightly different method for comparing the frequency of the light circulating in the PC with the light circulating in the RC.

For the heterodyne system, the frequency of the LO circulating in the RC is compared to the frequency of the HPL light circulating in the PC. This is maintained to be offset by a set frequency that ensures both the LO and HPL are resonant with the RC, and this offset frequency is used as the frequency of the expected interference between the LO field and the light field due to axion-like particles.

The frequency difference between the green light circulating in the RC for the TES scheme and the infrared light circulating in the PC is too large to measure. As a result, this scheme uses light from the RL split off before being frequency doubled as the frequency reference of the RC. The green light from the second-harmonic generation has a frequency that is exactly double the frequency of the split off infrared light, and thus the relationship between the green light and the RL infrared light is a constant one. For this reason, comparing the frequency of the HPL light circulating in the PC with the infrared light generated by the RL provides the necessary information about the frequency changes between the two cavities.

The ALPS IIa experiment is a smaller-scale technology development and demonstration system. It features facilities for two cavities, which are intended to simulate the systems for the PC and RC. Since it is primarily to develop technology for the TES measurement system, it features a high power laser (HPL) seeded by a non-planar ring

oscillator laser capable of outputting 35 W at an infrared wavelength of 1064 nm [45], similar to the generation system will for ALPS IIc, and a non-planar ring oscillator reference laser (RL) at the same wavelength that is frequency-doubled to a green wavelength of 532 nm before being directed to the RC. For this thesis, only the RC is used and the PC is not equipped.

The mirror parameters for the ALPS IIa RC are slightly different from the planned parameters of the ALPS IIc cavities. The input mirror, M1, has a transmission of 25 ppm for infrared light and 5% for green light. The output mirror, M2, has a transmission of 3 ppm for infrared and 1% for green. The cavity is 9.24 m in length. The propagation losses for the ALPS IIa cavity have been measured to be (33 ± 1) ppm [46]. This results in a power build-up of $26\,900 \pm 900$ and a finesse of $101\,300 \pm 500$, an FSR of 16.2 MHz, and a linewidth of (160 ± 1) Hz. For green light, the mirror parameters are the same as expected in ALPS IIc, so everything that depends only on the mirror parameters like the power build-up and finesse will be the same as expected in ALPS IIc. Additionally, the FSR only depends on the length, so that should be the same as the FSR for the infrared beam. Finally, the linewidth depends on both, so that is expected to be 160 kHz.

It is necessary to be able to project the performance of the cavities of ALPS IIc given the performance of ALPS IIa. The measurement of the changes in frequency of the laser relative to the cavity resonance is done using the Pound-Drever-Hall technique discussed in Section 1.4. One consideration is the relationship between length and frequency in Equation 1.34. When considering the resonant frequency change due to a cavity length change, the same length change in a longer cavity causes a smaller frequency change than it would in a shorter cavity, given by

$$\frac{\Delta Lc}{L_{IIc}\lambda_0} = \Delta f_{IIc} = \frac{L_{IIa}}{L_{IIc}} \Delta f_{IIa}, \quad (1.65)$$

where L_{IIa} is the length of ALPS IIa and L_{IIc} is the length of ALPS IIc. As such, any frequency changes due to length changes will be smaller by the ratio of the lengths of the two cavities, which in the case of ALPS IIa and ALPS IIc is $9.24\text{ m}/124.4\text{ m} = 0.07$.

In order to meet the power build-up and cavity overlap requirements, control systems will need to be used. The next chapter will discuss some of the fundamentals of controls for both analog and digital systems.

2. Controls and Digital Signal Processing

The goal of control systems is to change the dynamics of a system in order to maintain a specific condition or state. The systems to be controlled can cover a wide range, from a tall building, to a lamp, to the air temperature in a room, and many others. Control systems can be passive or active. A passive system usually seeks to minimize the effect of anything that would change the desired state, whereas an active system seeks to correct any of the changes. A passive system could be a tuned mass damper in the tall building to minimize any movements of the building. Active systems can be changing the duty cycle of a lightbulb so that the lamp produces a specific amount of light, a thermostat and heating, ventilation, and air conditioning system maintaining the air temperature in the room, and any number of control systems matched to the system to be controlled.

There are a number of control systems in ALPS II. This thesis will focus on those used in the regeneration cavity (RC) of ALPS IIa. In this chapter, we will discuss the control theory that goes into the design and characterization of those control systems. The following chapters will describe the specific control systems that are being characterized.

2.1. Feedback Control Systems

One type of system that ALPS will use, and the type of system that is used in this thesis, is one that takes a measurement and uses that measurement to produce some sort of correction. This type of system is known as a feedback control system, or FCS. An FCS has a number of different parts that are each important: the plant, sensing system, servo, and actuation system.

The plant is the system to be controlled. The plants in the ALPS IIa RC are made up of lasers and cavities. The desired state of these plants is usually the lasers being resonant in the cavity. When no control is being exerted on this plant, it is said to be 'free-running.' When this is the case, it is subject to many effects that prevent this desired state from being maintained for any longer than a fraction of a second. These effects are known as disturbances, which induce noise to the system, and the point of a control system is to compensate for this noise.

The sensing system is made up of a number of components and techniques used to sense the state of the system including how far away and in what direction it is from the desired state. A sensing system for a control system to keep a laser close to resonant in the cavity uses the Pound-Drever-Hall technique discussed in Section 1.4, which includes photodetectors, demodulators, any read-in components for digital systems, and any other electronics in the error signal path.

The servo is the device that converts the error signal input from the sensing system into the control signal that is the input to the actuation system. The design of a servo is

very important to a control system, and the majority of this chapter describes different forms and rules of thumb involved in defining a servo.

The final part of an FCS is the actuation system. This system takes the control signal and uses it to make a change to the plant. This often includes the actuator itself, the actual device that induces the physical change, and any associated electronics like amplifiers to increase the dynamic range of the actuation beyond what the servo itself can provide.

When all parts of the FCS are operating, any changes in the plant are sensed by the sensing system, modified by the servo, and compensated for by the actuation system, thus creating a closed loop. This closed loop operation nominally keeps the state of the plant very close to the desired state and successful maintenance of this state is also referred to as a lock as it may seem like the plant is locked to the ideal state.

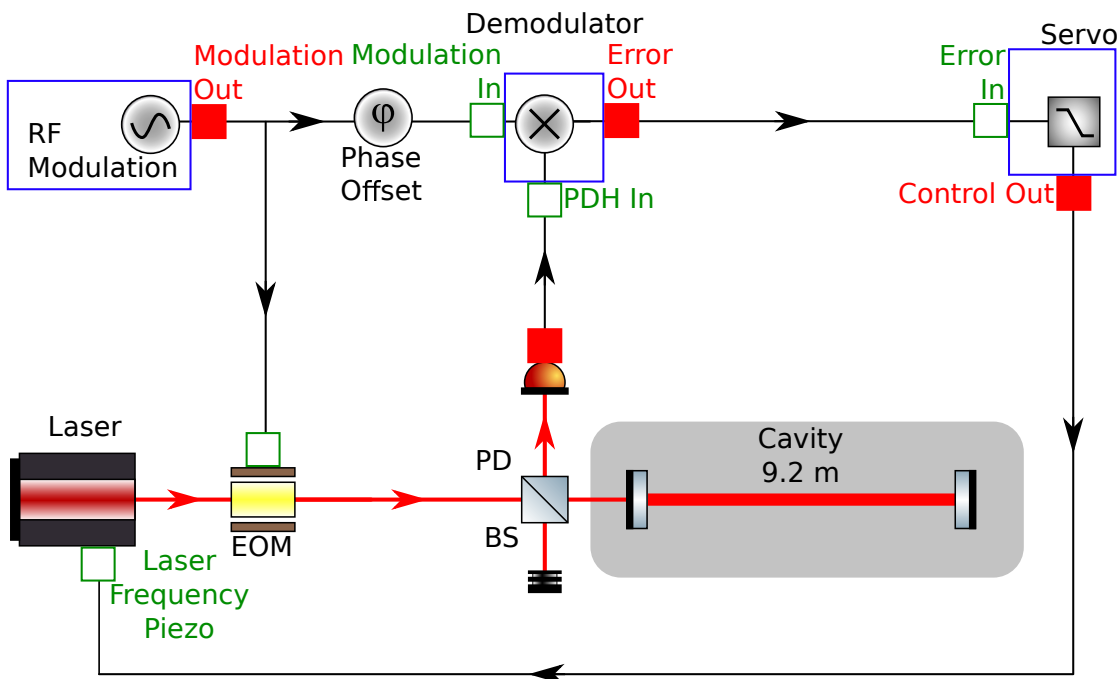


Figure 2.1.: An example of a feedback control system to keep a laser resonant with an optical cavity. The state of the resonance is measured using the Pound-Drever-Hall technique, modified by a servo, and fed back to the frequency of the laser.

A simple example of an FCS used in ALPS IIa to keep a laser resonant with a cavity is shown in Figure 2.1. The plant in this system is the laser and the cavity. The sensing system uses the Pound-Drever-Hall technique described in Section 1.4 and consists of the modulator, the photodetector, and the demodulator. The servo will be largely described in this chapter. Finally, the actuator in this example is a piezo-electric element that can put a variable amount of stress on the laser crystal which changes the frequency of the laser output.

This example is one system in ALPS II. However, there are other plants, measurement systems, servos, and actuators in the ALPS II experiment. As such, this chapter will be a general discussion of feedback control systems that can be applied to any system. Specific systems will be discussed as they are experimentally characterized in the following chapters.

In a perfect world, the error signal would be driven to zero during closed-loop operation and the control signal would be exactly the opposite of all noise induced by disturbances. However, doing so is impossible for a real control system. As such, the error signal ends up being much smaller than the disturbance-induced noise, but there is some residual error still present in the system. This noise left on the nominal operating point of the system is called suppressed noise, as it is after the suppression from the FCS. The noise induced by all disturbances is known as the unsuppressed noise, as it shows what the noise would be without suppression by the FCS.

However, the disturbances to the plant are not the only sources of noise in a closed-loop control system. Different parts of the control system also have noise associated with them. The sensing system, the servo, and the actuator can all impart noise into the system that would otherwise not be present. In a well-designed control system, the suppressed noise after implementing a FCS is much lower than the free-running noise of the plant, but that does not mean noise due to the FCS can be discounted.

The sensing system is not perfect and will have some noise from the electronics and other effects that do not reflect the behavior of the plant. This noise is referred to as sensing noise. One note is that noise added by the measurement system directly couples in to the suppressed noise. This is because sensing noise is feeding the control system incorrect information about the plant, which drives the system to compensate for this false noise. As such, the measured error signal is not always the same as the suppressed noise of the system, as the error point does not always perfectly correspond to the nominal operating point of the system due to sensing noise.

Similar to the measurement system, the actuation system also has some noise associated with it. This is usually due to the electronics involved in producing the actuation rather than the actuator itself, but some actuators can introduce their own noise. Fortunately, this control noise is suppressed by the loop and often much smaller than the disturbances to the plant, though that can depend specifically on the exact properties of the FCS and the actuator noise.

In addition to the sensing and control noise, the servo may have some noise associated with it. However, it can often be convenient to assign this noise to either sensing noise on the input side, or control noise on the output side. With this, the servo can be treated largely as a mathematical operation. It is not always true that there is no noise associated with the servo. However, these sources of noise are usually much smaller than the sensing noise and control noise.

There are many different ways to classify control systems, which can be analyzed very differently from each other. Some of the classifications of the systems used in the ALPS IIa RC will be discussed in this chapter, as well as what that classification means. The first simplification that we will make is based on inputs and outputs. A system can have any number of inputs and any number of outputs. These are multi-input,

multi-output systems and the analysis of these systems needs to take into account the similarities and differences of each input and output. However, all of the systems used in the ALPS IIa RC are single input, single output systems, or can be approximated as such as the interactions between the two systems are minimal. This allows us to perform analysis in a simpler way than would be possible in multi-input, multi-output systems.

2.2. Transfer Functions

A system can be defined as something that takes an input and produces an output. These systems are presented in [47] and some of this work will be paraphrased in the following derivation. This input being converted by a system to an output can be represented mathematically with a transformation, H , defined as

$$y = H(u), \quad (2.1)$$

where u is the input and y is the output. The input and outputs can be broken into multiple components given by

$$\begin{aligned} y &= y_1 + y_2 + y_3 + \dots \\ &\text{and} \\ u &= u_1 + u_2 + u_3 + \dots \end{aligned} \quad (2.2)$$

These components can be as small or as large as desired to describe the inputs and outputs. For a linear, time-invariant system, H can be defined such that

$$y(t) = H(u) = \int_{-\infty}^{\infty} u(\tau)h(t - \tau)d\tau, \quad (2.3)$$

where $h(t - \tau)$ is the impulse response function, defined as the input of the system to an infinitely short impulse at time τ . The output is simply the sum of the output infinitely many impulses, which is a result of the principle of superposition. Additionally, the output is dependent only on the time between input and observation. This operator is also known as a convolution, which is often represented as

$$\int_{-\infty}^{\infty} u(\tau)h(t - \tau)d\tau = u(t) * h(t). \quad (2.4)$$

This convolution of the input with the impulse response in the time domain is not always easy to work with, so it is more convenient to convert this into complex frequency space by using the Laplace transform. The Laplace transform is defined as

$$F(s) \equiv \mathcal{L}\{f(t)\} \equiv \int_0^{\infty} f(t)e^{-st}dt, \quad (2.5)$$

where s is a complex variable given by $s = \sigma + i\omega$ and known as the complex frequency. The behavior in frequency can be seen by setting $\sigma = 0$, or $s = i\omega$. This is very useful because of a property of the Laplace transform of convolutions, namely

$$\mathcal{L}\{f * g\} = F(s)G(s). \quad (2.6)$$

Therefore, when we take the Laplace transform of Equation 2.3, we get

$$Y(s) = H(s)U(s), \quad (2.7)$$

which can be re-arranged to show that $H(s)$ is the ratio of the output to the input, that is

$$\frac{Y(s)}{U(s)} = H(s). \quad (2.8)$$

$H(s)$ is referred to as the transfer function, because it determines how the signals are transferred from the input to the output at different frequencies. It can be more convenient to work in the frequency domain rather than the time domain, especially for designing control systems.

One property is that the transfer function of a system consisting of several sub-systems connected in series can be described by simply multiplying the transfer functions of the sub-systems together. This is apparent when considering the time domain explanation of such a system. If we take an example of three sub-systems with an impulse response of $h_1(t - \tau)$, $h_2(t - \tau)$, and $h_3(t - \tau)$, where h_1 is the first system and h_3 is the last system, we see that the output of the system in response to an input is

$$y(t) = h_3 * h_2 * h_1 * u(\tau), \quad (2.9)$$

and further systems would continue to add more convolutions. The Laplace transform of this equation is

$$Y(s) = H_3(s)H_2(s)H_1(s)U(s), \quad (2.10)$$

and therefore the transfer function is given by

$$H(s) = \frac{Y(s)}{U(s)} = H_3(s)H_2(s)H_1(s). \quad (2.11)$$

The combination of all transfer function in a control system, including the sensor, control electronics, actuator, and any other sub-systems is known as the open-loop transfer function. This open-loop transfer function is important, as an open-loop transfer function with a larger magnitude allows the system to suppress more free-running noise [48]. The magnitude of a transfer function is referred to as gain. There are limits when this gain affects the stability of a control system, which we will investigate in Sections 2.3.

The transfer function is a powerful tool for frequency-domain analysis of systems. It is also useful for designing control systems given the knowledge that the noise suppression of the system is largely determined by the transfer function of the full system. Though a given system can have an arbitrary transfer function, many linear, time-invariant, physical systems are described by the linear, constant coefficient differential equation

$$\sum_{k=0}^n a_{n-k} \frac{d^k}{dt^k} y(t) = \sum_{k=0}^m b_{m-k} \frac{d^k}{dt^k} u(t). \quad (2.12)$$

That is to say, a linear combination of the output of a system and its derivatives is equal to a linear combination of the inputs to that system and its derivatives.

When applying a Laplace transform to derivatives, we get

$$\mathcal{L} \frac{d^n f(t)}{dt^n} = s^n F(s) - \sum_1^n s^{n-k} \frac{d^{k-1} f(0)}{dt^{k-1}}. \quad (2.13)$$

Though the properties of the function at $t = 0$ are necessary to understand the exact behavior of the system, it is not strictly necessary to understand the behavior of the input compared to the output and we can assume that it is 0. This property allows us to take the Laplace transform of Equation 2.12 to get

$$\sum_{k=0}^n a_{n-k} s^k Y(s) = \sum_{k=0}^m b_{m-k} s^k U(s) \quad (2.14)$$

which can be re-arranged as

$$\frac{Y(s)}{U(s)} = H(s) = \frac{\sum_{k=0}^m b_{m-k} s^k}{\sum_{k=0}^n a_{n-k} s^k} \quad (2.15)$$

in which the transfer function, $H(s)$, is a m -order polynomial in the numerator and an n -order polynomial in the denominator. The only restriction on the order is on the relative degree, which is that $n - m \geq 0$ which is imposed by the realizability of the system which we will discuss in Section 2.3. Another way to represent the transfer function in Equation 2.15 is to factor the numerator and denominator

$$H(s) = \frac{\sum_{k=0}^m b_{m-k} s^k}{\sum_{k=0}^n a_{n-k} s^k} = K \frac{\prod_{k=1}^m s - z_k}{\prod_{k=1}^n s - p_k} \quad (2.16)$$

where $K = b_0/a_0$. The roots of the numerator are known as zeros because the transfer function goes to zero when $s = z$ and the roots of the denominator are known as poles because the transfer function goes to infinity when $s = p$. Zeroes and poles are useful building blocks when designing a control system. Low-pass filters, notch filters, integrators, differentiators, etc can all be easily implemented in analog electronics, and are all described by zeros and poles.

Poles and zeros can be complex numbers. That is to say $z = x + iy$ and $p = x + iy$, with some complications if $y \neq 0$ that will be discussed shortly. The magnitude of the pole or zero describe the frequency at which the effect, i.e. low pass corner frequency, notch filter center frequency, is located. A purely real, negative pole is a low pass filter that applies a $1/f$ slope at frequencies much higher than the corner frequency, and a purely real, negative zero is a differentiator that applies an f slope at frequencies higher than the corner frequency.

With complex poles and zeros, a second one is always needed. The reason for this is that $H(s)$ must be real, so for a complex pole introduced at $p = x + iy$, another one at $p = x - iy$ ensures that the resulting product is real. A complex pole pair results in resonant gain at the frequency determined by the magnitude, and the relative size of the imaginary part describes the bandwidth. Similar to a complex pole, a complex zero is a notch with the parameters being determined the same way as with a complex pole.

In addition to frequency-domain representation using transfer functions or zeroes and poles, there are a number of time-domain representations. One such representation is state space, which models a number of variables that keep track of the state of the system. These variables evolve depending on the other state variables and inputs to produce an output. A number of the control systems in this thesis are realized using a state space system and this representation is discussed in Chapter A, but the analysis is done using frequency-domain analysis.

Since the models are equivalent, a system that is described with a transfer function can be equally described by a state space model. In transferring between the two systems, it is clear that the model order of the systems is also the same. That is to say, a system described by m poles and zeros produces a m -order transfer function, which is equivalent to an $m \times m$ state space system.

2.3. Control Stability

In order to implement an effective control system, it needs to be stable and realizable. This ensures that, given some input, it will not end up increasing output infinitely, require infinite energy to generate the output, or introduce an excessive amount of noise. There are several important criteria in order to achieve these goals.

The first is that the real part of every pole needs to be less than zero. That is, in the complex number plane where the real part is the x-axis and the imaginary part is the y-axis, all poles must exist in the left half of this plane. This requirement can be seen by examining the time-domain behavior of a system with no input. That is to say, if the $u(t)$ in Equation 2.12 were zero we get

$$\sum_{k=0}^n \frac{a_{n-k} d^k y(t)}{dt^k} = 0. \quad (2.17)$$

We know that the solution to the homogenous version of this differential equation involves finding the roots of the characteristic polynomial [49] given by

$$\sum_{k=0}^n a_{n-k} d^k = 0, \quad (2.18)$$

which we already know to be the poles of the system in Equation 2.16, which is to say

$$\sum_{k=0}^n a_{n-k} d^k = \prod_{k=1}^n s - p_k = 0. \quad (2.19)$$

In the end, the solution to the differential equation has the form

$$y(t) = \sum_{k=1}^n c_n e^{p_k t} = \sum_{k=1}^n c_n e^{x_k t} e^{iy_k t}, \quad (2.20)$$

and we can see that any pole with a positive real part, which is any $x_k > 0$ will grow exponentially with time and is therefore unstable, whereas any pole with a negative real part will decay exponentially with time. We can also see that if the real part of the pole is zero, then the result will neither grow nor decay with time. As such, any poles that lie directly on the imaginary axis are called marginally stable.

The second requirement, not purely for stability but for realizability, is that the order of the numerator cannot exceed the order of the denominator, which was already mentioned in Section 2.2. This is known as a proper transfer function, whereas one with a relative degree less than zero would be known as an improper transfer function. If the relative degree is larger than zero, then the transfer function is called strictly proper. An improper transfer function can be written

$$H(s) = \frac{\sum_{k=n+1}^m b_{m-k} s^m + \sum_{k=0}^n b_{n-k} s^k}{\sum_{k=0}^n a_{n-k} s^k}, \quad (2.21)$$

and can be factored into poles and zeroes as

$$H(s) = K \frac{(\prod_{k=n+1}^m s - z_k) (\prod_{k=1}^n s - z_k)}{\prod_{k=1}^n s - p_k}, \quad (2.22)$$

where all z_k and p_k are finite. As such, the behavior at very high frequencies, when $\lim_{\omega \rightarrow \infty} H(i\omega)$, the values of each z_k and p_k are small compared to $i\omega$, and can be neglected. Thus we get

$$\lim_{\omega \rightarrow \infty} H(i\omega) = K \frac{s^{m-n} s^n}{s^n} = K s^{m-n}, \quad (2.23)$$

which is $m - n$ pure differentiators, and pure differentiators are not realizable [50]. This restriction is already present in the construction of the state matrices as we can see in the result in Equation A.17 where the relative degree is always ≥ 0 .

The final stability criterion has to do with the phase of the transfer function. This can be intuitively examined by examining the Bode plot of the open-loop transfer function [48]. The important point to look at in the Bode plot is where $|H(i\omega_{ug})| = 1$, known as the unity gain frequency. At the unity gain frequency, the amount by which the phase lags less than 180° , given by

$$\phi_m = \phi[H(i\omega_{ug})] + 180^\circ \quad (2.24)$$

where ϕ_m is known as the phase margin. A system that has any phase margin larger than 0° is technically stable, but it would not be very robust and would be prone to oscillation. A larger phase margin is a more robust system with less oscillation. Two significant contributors to phase lag are a steeper slope in the gain curve, which results

in a larger phase lag, and any time delays in the system result in larger phase lags at higher frequency. As such, the two ways of increasing the phase margin are reducing the slope of the gain and reducing the unity gain frequency, ω_{ug} . Reducing the slope of the gain means the gain will be smaller at frequencies under the unity gain frequency, and reducing the unity gain frequency means reducing the overall gain of the system, which reduces the gain at all frequencies. As such, it becomes important to balance the robustness and oscillation with the gain of the system.

2.4. Discrete Time

The techniques used in continuous time analysis can also be applied to discrete time systems. However, some modifications need to be made in order to accomplish that. In order to determine what those modifications are, we should start with how to convert signals from continuous time to discrete time. An ideal case would be taking the instantaneous value of a continuous time function every T period of time. An infinite series of Dirac Delta functions separated in time would be able to extract this value. Such a series, or impulse train, would look like

$$p(t, T) = \sum_{n=-\infty}^{\infty} \delta(t - nT), \quad (2.25)$$

and would be applied to a continuous time function to result in

$$p(t; T)f(t) = \sum_{n=-\infty}^{\infty} \delta(t - nT)f(t) = \sum_{n=-\infty}^{\infty} f_n(t). \quad (2.26)$$

This results in a series of pulses, $f_n(t)$, that are scaled such that they result in the values of $f(t)$ at each sample point when integrated

$$\int_{-\infty}^{\infty} p(t; T)f(t)dt = \int_{-\infty}^{\infty} \sum_{n=-\infty}^{\infty} \delta(t - nT)f(t)dt = \sum_{n=-\infty}^{\infty} f(nT) = \sum_{n=-\infty}^{\infty} f_n, \quad (2.27)$$

where f_n is simply the value of $f(nT)$ and no longer has any dependence on t .

Just as it is convenient to do analysis and design of continuous time systems in the complex frequency domain by using the Laplace transform, it can be convenient to do the same things with discrete time systems. As such, we need a discrete time analog to the Laplace transform. This is what is known as the Z transform. It can be calculated by starting off with a continuous time system, apply our impulse train, and then take the Laplace transform. That gives us

$$\mathcal{L} \left\{ \sum_{n=-\infty}^{\infty} \delta(t - nT)f(t) \right\} = \int_0^{\infty} \sum_{n=-\infty}^{\infty} \delta(t - nT)f(t)e^{-st}dt = \sum_{n=0}^{\infty} f_n e^{-nsT}. \quad (2.28)$$

We can then define a variable, $z = e^{sT}$ thus giving us a Z transform of f_n to be

$$Z\{f_n\} \equiv F(z) \equiv \sum_{n=0}^{\infty} f_n z^{-n}. \quad (2.29)$$

If we use this substitution to move between the continuous time s-domain and the discrete time z-domain, we can see what would happen with the poles and zeros in the Equation 2.16. If we are applying the relationship in Equation 2.28 to s , we must also apply it to the zeros and poles, as they are defined in relationship to s . As such, our z-domain poles and zeros would look like

$$H(z) = K \frac{\prod_{i=1}^m z - e^{z_i T}}{\prod_{i=1}^n z - e^{p_i T}}. \quad (2.30)$$

As long as we are careful about whether we are in the s-domain or z-domain, we can merely re-define our coefficients based on the converted poles and zeros and otherwise apply the same math. In the z-domain, we will be using α and β instead of a and b for the coefficients to more clearly differentiate the two. As such, we can see that a transfer function in the z-domain would look very similar to a transfer function in the s-domain. Multiplying the poles and zeros give us a transfer function of a similar form to that in Equation 2.15 merely with different coefficients. Additionally, for much the same reasons as we are able to do in Equation A.18, we can set the order of the numerator equal to the order of the denominator with no loss of generality. This transfer function in z space looks like

$$H(z) = \frac{\sum_{k=0}^m \beta_{m-k} z^k}{z^m + \sum_{k=0}^{m-1} \alpha_{m-k} z^k}. \quad (2.31)$$

One important note here is that there is one change to the stability criteria discussed in Section 2.3. The criterion that the transfer function must be proper, i.e. the relative degree of the transfer function cannot be less than 0, remains unchanged. Additionally, the criterion that the phase margin of the transfer function must be positive remains the same. However, the criterion that the real part of poles must be negative changes, as the poles are calculated differently in the z-domain. If we calculate the new criterion for the z-domain poles from the poles in the s-domain, then we see that the pole $p_k = x_k + iy_k$ becomes

$$e^{(x_k + iy_k)T} = e^{x_k T} e^{iy_k T}, \quad (2.32)$$

and the criterion that $x_k \leq 0$ becomes $e^{x_k T} \leq 1$. Thus, the region of stability for poles in the z-domain is the unit circle, with points on the unit circle being marginally stable.

It can be seen in Equation 2.30 that the sampling period, T , or alternatively the sampling frequency, $f_s = 1/T$, plays a big part in the behavior of poles and zeros, and thus the transfer function. If one defines the poles and zeros for the transfer function at one sampling frequency and then changes the sampling frequency, the features will be located at a different frequency than initially intended.

There is another effect from changing the sample frequency, which is that the phase lags more. This phase lag is due to the amount of time it takes the signal to propagate through the digital system. A digital system can only do actions every clock cycle. So when digital data needs to pass through different parts of the code, each action costs time. Additionally, controllers frequently require several clock cycles to complete the calculations necessary to output a control signal.

2.5. Quantization in Digital Systems

Changing from continuous to discrete time is not the only change necessary when moving to digital systems. The quantization of numbers is also necessary to consider. Rather than a number being able to take any value and change by amounts that are infinitesimally small, digital systems can only represent a discrete number of values. These values are represented by the number of bits assigned to that number, which is known as the word length. These bits combine to represent a number in base 2 rather than base 10. As such, a number represented by n bits can take 2^n unique values. The first quantization takes place on the input of the digital system. The analog to digital converter (ADC) measures the value of the input (usually a voltage) and converts it to a number that represents the value of the range of the input. For example, a 16-bit ADC that has a ± 1 V input range would represent the range of 2 V with $2^{16} = 65536$ unique values. In this representation, the smallest change able to be represented by n bits, known as the least significant bit (LSB), is directly proportional to the range of values represented and inversely proportional to 2^n . This LSB is calculated by

$$\text{LSB} = \frac{N_{pk-to-pk}}{2^n}, \quad (2.33)$$

where $N_{pk-to-pk}$ is the the difference between the largest and smallest value able to be represented by our number. In our example ADC, the smallest voltage change able to be represented is $2\text{ V}/2^{16} \approx 30.5\ \mu\text{V}$. The difference between the ideal signal and a quantized signal is shown in Figure 2.2 where we see that instead of a smooth line, the signal looks like a staircase. This example is created by rounding the input value. Some quantization is done by truncating the number such that the quantized value is always less than the input value. Though truncating is not usually desired for the quantization of signals, it can be useful for the quantization of control coefficients.

This quantization of the signal can affect different parts of a digital servo. The first is that there is some noise introduced by the quantization. The distribution of this noise is considered to be uniform, with a value ranging over $\pm\text{LSB}/2$. Since the error is uniform and centered around zero, its mean is zero. Thus, when we look at the rms variance, σ , defined as

$$\sigma = \sqrt{\int_{-\infty}^{\infty} (x - \mu)^2 f(x) dx}, \quad (2.34)$$

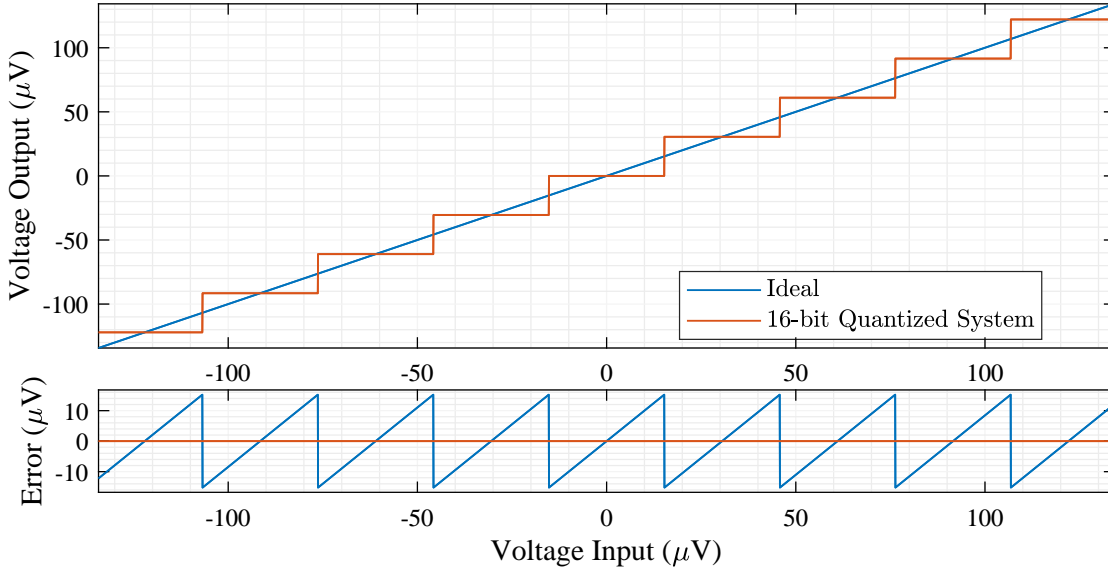


Figure 2.2.: An example of the quantization of an ideal, linear signal from an ADC with a range of ± 1 V and 16 bit word length. In the upper part, the blue curve is the ideal, analog signal and the orange curve is the quantized signal. The lower part is the error due to the quantization. The blue curve is the error between the ideal and quantized signal and the orange curve is a reference line at 0.

where μ is the mean and is zero, and $f(x)$ is the probability density function. This $f(x)$ integrates to 1 over the range $\pm\text{LSB}/2$, and is zero everywhere else, thus

$$1 = \int_{-\infty}^{\infty} f(x)dx = \frac{1}{\text{LSB}} \int_{-\text{LSB}/2}^{\text{LSB}/2} dx, \quad (2.35)$$

and so we see that the equation for σ is

$$\sigma = \sqrt{\frac{1}{\text{LSB}} \int_{-\text{LSB}/2}^{\text{LSB}/2} x^2 dx} = \sqrt{\frac{\text{LSB}^2}{12}} = \frac{\text{LSB}}{\sqrt{12}}, \quad (2.36)$$

which gives us the rms variance of the noise introduced by the quantization of the signal [51]. The power spectral density can be obtained by integrating this variance from 0 to the Nyquist sampling frequency (which is half the sampling frequency, $f_s/2$) with the assumption that the noise is present only in the band of interest rather than infinitely across all frequencies. The amplitude spectral density of this noise, $A(\Omega)$ is given by the square root of the power spectral density, which is

$$A(\Omega) = \frac{\text{LSB}}{\sqrt{6f_s}}, \quad (2.37)$$

where f_s is the same sampling frequency in Section 2.4.

Another way that quantization can affect a system is by changing to coefficients determining the behavior of the servo. This quantization means that different representations of the same system are no longer identical. It can therefore be important to identify a way to distribute coefficients such that quantization has the least effect on the system. An appropriately balanced realization of a state space model contains more coefficients than the canonical forms, presented in Appendix A, and thus increases the required processing power, but results in less quantization. Alternatively, one could break a transfer function model into sets of second order systems to reduce the effect of quantization on controller coefficients [52]. There are a number of methods to accomplish these tasks, but the MATLAB (used in versions 2016b and 2017b for this work) command 'balreal' for state space and 'tf2sos' or 'zp2sos' are effective at this task.

The final effect that quantization can have is that of overflow. If a number is represented by a fixed number of bits with a fixed range, then exceeding that range causes what is known as an overflow. Take an example of a four bit number that can represent numbers from 0 to 1. The LSB of this quantization is $1/16 = 0.0625$. In this instance, the base 2 representation 0000 is 0 and 1111 is 1. If we were looking at 0000 and added 0.0625 to it, we would get 0001, and doing so again would result in 0010. This sort of math is the same as with any other number until we get to the largest number we can represent: 1111, or 1. If we try to add 0.0625 to that number, the system would try to add 1 to the next largest digit to get 10000, but such a digit does not exist and is therefore truncated. The result is 0000, or 0. A similar problem can happen when subtracting 1 from 0000 to get 1111.

The problems posed with overflow need to be balanced with the additional noise and controller representation posed with having a larger LSB, as the range of numbers able to be represented is directly proportional to the size of the LSB, as shown in Equation 2.33. Ideally, the number of bits would be increased, but there is a practical limitation to the word size as digital systems have a finite amount of memory, and every bit takes up some of that memory.

With the fundamentals of LSW experiments, optical cavities, and control systems established, the next chapter will discuss the characterization of optical cavities and the baseline, mostly analog control systems of those optical cavities. The following chapters will cover the digital systems and compare them to the analog systems.

3. ALPS IIa Regeneration Cavity

In order to provide a comparison to digital systems and understand the performance of the baseline control systems, it is important to characterize the current control systems in the ALPS IIa Regeneration Cavity (RC). These systems include frequency control for an infrared beam in the cavity, frequency control for a green beam in the cavity, and length control for the cavity to match the green beam in the cavity. The two frequency control systems are entirely analog, and the length control system includes a digital filter to compensate for mechanical resonances.

3.1. Calibration

Calibration is vital to understanding the behavior of the cavities. A proper calibration allows for comparison to other, properly calibrated systems because we know the behavior of them in physical units. The motion of the cavities and the changes in the lasers can be in terms of the length of the cavity and wavelength of the laser, or in terms of the resonance frequency of the cavity and the frequency of the laser. In this thesis, we will be using frequency units, though Equation 1.34 shows that the two are directly proportional with only a multiplicative factor required to convert between them.

The first task is the calibration of the control signal. Applying a linearly increasing voltage to the frequency actuator gives us a linear change in the laser frequency over time. We then look at the PDH signal and note that the spacing of the sidebands in Figure 1.8 is the modulation frequency. This gives us a relationship, in Hz/V, between the voltage applied to the actuator, and the frequency change induced. Using this relationship, we can then express any control signal voltage in terms of frequency change.

Once the control signal is calibrated, that calibration can be used to calibrate the error signal. By looking closely at just the center band resonance, like in Figure 1.9, the change voltage of the error signal due to the change of frequency induced by the control signal allows us to calibrate the linear portion of the error signal. This tells us how a given read-out voltage change corresponds to a frequency change in the cavity.

This error signal is calculated in Equation 1.47 and depends on the input power, the mirror parameters, the cavity loss, and the strength of the modulation. Additionally, the error signal depends on the relative alignment between the resonant cavity field and input field in all three dimensions, which determines how the input field couples into the cavity field. This alignment can change over time periods generally on the order of days as it will drift. Even after correcting for the bulk of these drifts, small misalignments may persist, which would require a new calibration of the error signal for every measurement.

Using the above calibration methods for the green beam produced by frequency doubling the reference laser, we get that the calibration for the control signal (of the fre-

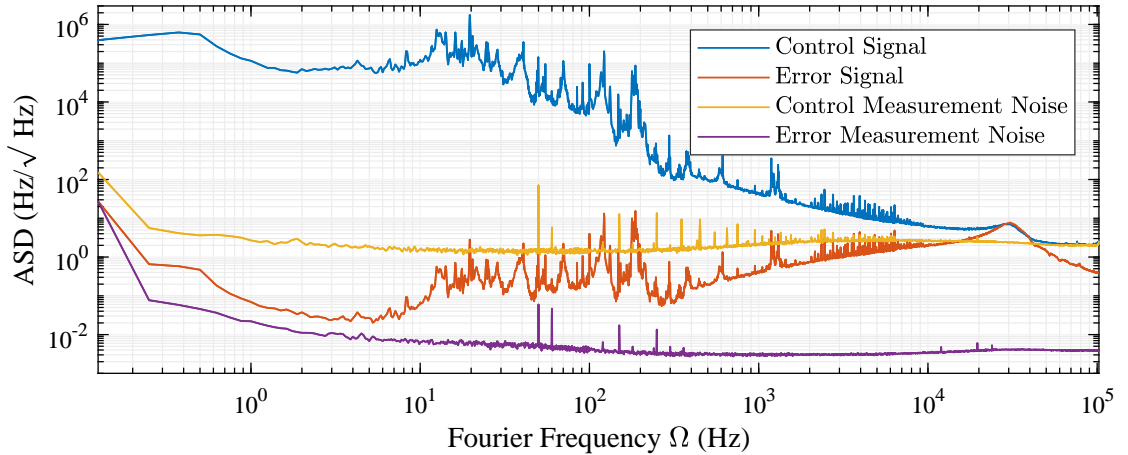


Figure 3.1.: An example of a calibrated control and error signal of a green frequency control system. The control signal is the signal sent to the laser piezo and the error signal is the signal sent to the control electronics. The control signal calibration was performed by applying a voltage ramp to the laser piezo and measuring the voltage required to shift the laser frequency between the PDH side-bands at a known frequency and the center band. The error signal calibration was performed by comparing the slope of the PDH error signal to the control signal.

quency doubled green beam) is (5.2 ± 1.4) MHz/V. We then calibrated the error signal also as described above to get that calibration as (370 ± 120) kHz/V with the uncertainty being driven primarily by the uncertainty in the control calibration, which is correlated between the two measurements. This correlation is important, as we will see that we are mostly interested in the ratio between the control and error signal spectra, which has a much lower uncertainty.

A measurement of the amplitude spectral density of the control and error signal calibrated in this manner is found in Figure 3.1. The features in this and similar plots will be discussed later in this chapter, as well as the details of the experimental setup used to obtain these measurements. What is important here is the point at which the control signal and error signal meet. At this point, the error signal and the control signal are equal, and the suppression of the loop is 1. This means that the frequency at which this happens is the unity gain frequency of the open-loop transfer function. If we look at a Bode plot of this transfer function in Figure 3.2, then we see that the unity gain frequency is the same as the crossover point of the control and error signal in Figure 3.1.

Using this behavior, we can calibrate the error signal by using the unity gain frequency of the open-loop transfer function. As this transfer function is for the full system, all factors that affect the size of the error signal are accounted for. We can adjust the calibration such that the crossover point is where we expect it to be from the open-loop transfer function to obtain the same result as a more direct calibration of the error signal. This is much quicker than the first technique described in this section, especially as the transfer function also provides other desirable information about the performance of the

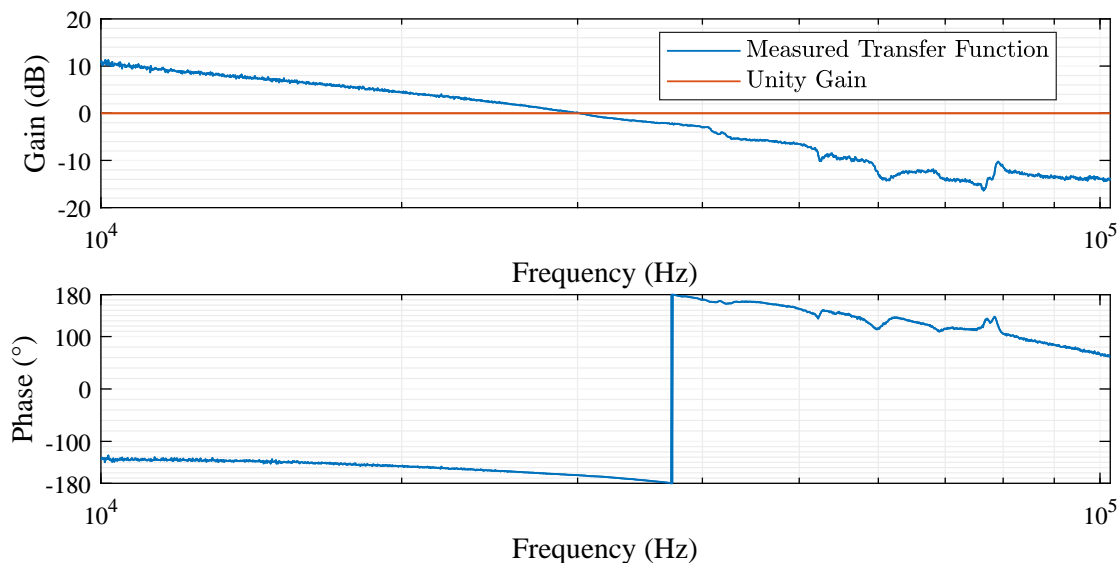


Figure 3.2.: An example of an open-loop transfer function for the green frequency control system. This was measured by injecting a swept sine on the control signal and comparing the control signal with the swept sine to the control signal right before the swept sine was injected. The measurement was made with an averaging factor of 100 and an input of between 0.1 mV and 5 mV peak-to-peak. The unity gain frequency of this system is 30 kHz.

loop, such as the phase margin, and will therefore be taken whether or not it is used for calibration. Additionally they are very useful for the design and optimization of control systems as discussed in Chapter 2.

Since the open-loop transfer function already needs to be taken and can provide a good calibration of the error signal without having to measure it directly, this thesis will use that method to calibrate all error signals in relationship to the control signals.

3.2. Infrared Frequency Control

With the intention that the high power laser (HPL) will have the frequency driven to match the cavity resonance frequency, i.e. frequency locked to the cavity, we must investigate the performance of the ALPS IIa HPL under frequency control. The schematic of this system is shown in Figure 3.3 with frequency of modulation to be 2.5 MHz. This phase modulation is applied to the laser beam incident on the cavity, generating sidebands that are reflected when the center band is resonant in the cavity. The promptly reflected sidebands are mixed with the light coming out of the cavity as well as the promptly reflected center band on a photodetector, encoding any changes of the laser relative to the cavity resonance on the interference between the center band and the sidebands. This signal is demodulated with the original modulation frequency to generate

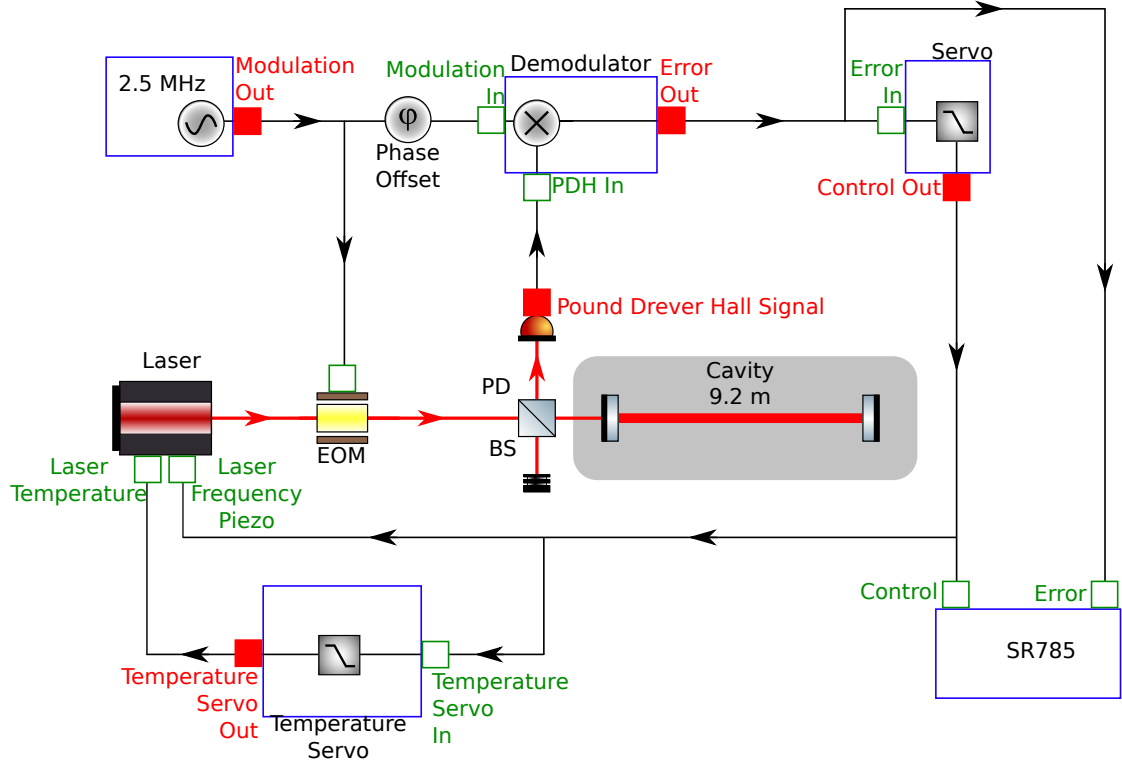


Figure 3.3.: Feedback control system to match infrared high power laser to the ALPS IIa regeneration cavity and measure the performance of this control. The modulation frequency is 2.5 MHz. This modulation is applied to the EOM and used to demodulate the signal from the error photodetector. That signal is then sent through a servo to produce a control signal that is sent to the laser frequency as well as a temperature servo to provide additional actuation range at low frequencies. The control and error signal are also measured by a Stanford Research Systems SR785 network analyzer.

the PDH error signal. This error signal is then fed through a servo to generate the control signal which is both applied to the piezo that controls the laser frequency and fed through a servo that generates a slow control signal which is applied to the laser temperature control. The error signal before the servo and the control signal before the piezo are split off to be measured by the Stanford Research Systems SR785 network analyzer.

We can also use the network analyzer to inject a swept sine wave to the control signal and compare the control signal before injecting the swept sine to the same signal after the swept sine to measure the response of the system to disturbances at specific frequencies and generate an open-loop transfer function. This open-loop transfer function is presented in Figure 3.4 and shows that the unity gain frequency is 40 kHz with a phase margin of 23°.

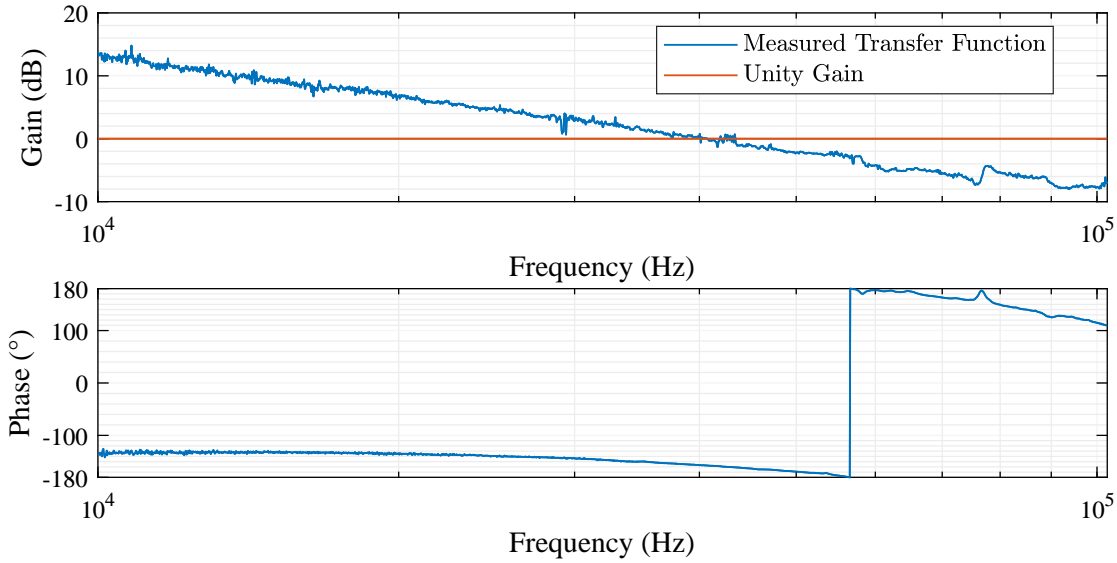


Figure 3.4.: Open-loop transfer function for the high power laser frequency control system. The unity gain frequency is 40 kHz with a phase margin of 23° . This transfer function was measured by injecting a swept sine on the control signal and comparing the control signal with the swept sine to the control signal right before the swept sine was injected. The measurement was made with an averaging factor of 100 and an input of between 0.1 mV and 5 mV peak-to-peak.

As discussed in Section 2.3, changing the proportional gain of the system also changes the unity gain frequency of the system, and thus the phase margin, as it does with all systems investigated in this thesis. The choice of where to set the proportional gain can be arbitrary beyond the criterion that the system remain stable over at least a long enough period to take a measurement. The two competing effects are that a lower proportional gain reduces the overall noise suppression of the system, while a higher proportional gain results in less phase margin, which induces more oscillation given the same disturbance close to the unity gain frequency. This oscillation is due to the reduction of the phase margin in the control loop, and thus adds noise to the system, which may result in a system with more total noise than a system with a lower proportional gain. It is referred to as a servo bump, as it appears as a bump in the noise spectra of both the error signal and the control signal.

The light circulating in the cavity is affected by the cavity pole discussed in Section 1.5 [53]. This means that the promptly reflected light and the light coming out of the cavity do not just differ in accumulated phase, but also by this filtering. As such, the measured error spectrum is not exactly the same as the spectrum of light in the cavity. This difference between the two spectra is given by

$$A_{f,measured}(\Omega) = A_f(\Omega) \frac{1}{\sqrt{1 + \left(\frac{2\Omega}{\Delta f_{peak}}\right)^2}}, \quad (3.1)$$

where $A_f(\Omega)$ is the amplitude spectral density of the offset between the laser frequency and the cavity resonance frequency as a function of the Fourier frequency, Ω (in Hz), which is measured in units of $\text{Hz}/\sqrt{\text{Hz}}$. $A_{f,measured}(\Omega)$ is the amplitude spectral density of the measured PDH signal. This relationship can be re-arranged to see how to convert the measured spectrum to the spectrum in the cavity

$$A_f(\Omega) = A_{f,measured}(\Omega) \sqrt{1 + \left(\frac{2\Omega}{\Delta f_{peak}}\right)^2}. \quad (3.2)$$

We can see that the cavity pole must be taken into account when analyzing the error signal for a cavity where the pole is within the frequency range under consideration.

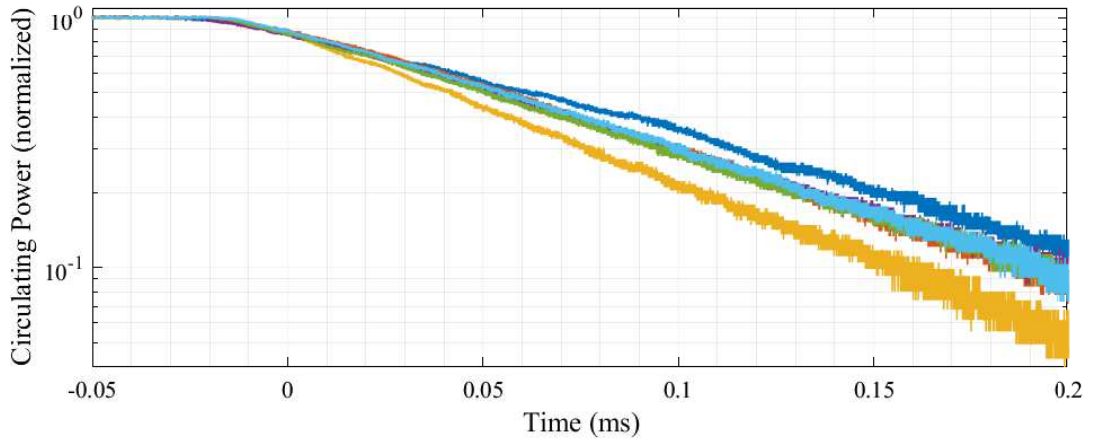


Figure 3.5.: IR ring-down measurement of ALPS IIa RC. The displayed plots are of the transmitted power. The control system was deactivated and the rate at which the power decreased is fit to determine the cavity storage time. The storage time of the cavity is (0.18 ± 0.02) ms. Six measurements are shown on this plot.

Based on the linewidth calculated in Section 1.5 from previously measured data, the cavity pole of the ALPS IIa RC for infrared light is 90 Hz. However, a more current measurement would yield better information about the current state of the internal losses. As these internal losses can have a large effect on the cavity pole, it must be measured. One method for determining the cavity parameters is using the storage time of the cavity, which is the time that it takes for the cavity field to decay by a factor of $1/e$, given by [54]

$$\tau_{storage} = \frac{2nL\mathcal{F}}{\pi c} = \frac{\mathcal{F}}{\pi f_{FSR}}. \quad (3.3)$$

The relationship between the storage time and the cavity pole, which is half of the cavity linewidth, is given by

$$f_0 = \frac{\Delta f_{peak}}{2} = \frac{1}{2\pi\tau_{storage}}. \quad (3.4)$$

This storage time was measured by shutting off the control system, which suddenly changes the laser frequency away from the cavity resonant frequency, then fitting an exponential decay function to the data, and determining the $1/e^2$ time from that fitted function [54]. The results of six of these ringdown measurements are shown in Figure 3.5, and show a storage time of (0.18 ± 0.02) ms. This corresponds to a linewidth of (1.8 ± 0.2) kHz and a cavity pole of (900 ± 100) Hz, additional losses of (700 ± 100) ppm, and a finesse of 9000 ± 1000 . The additional losses are significantly larger than the (33 ± 1) ppm of losses and the cavity finesse is significantly smaller than the $101\,300 \pm 500$ measured from a storage time of (1.99 ± 0.01) ms [46]. This increase of propagation losses is likely due to mirror contamination, as the mirrors are not kept in a fully clean-room environment when the vacuum tanks are open or when the mirrors need to be handled.

Once the appropriate proportional gain and cavity pole are determined and the open-loop transfer function is taken, we can take and calibrate a control and error spectrum. This tells us the spectral density of the noise at different frequencies. The calibration of the control signal for the high power laser is (1.4 ± 0.2) MHz/V. Setting the calibration of the error signal as described in Section 3.1 gives us a calibration of (31 ± 4) kHz/V for the error signal. The uncertainty is only from the uncertainty in the calibration of the control signal, as the signals used for this calibration were averaged many more times than the measurements used to calibrate the control signal, and the uncertainty for the number of averages, N , decreases as $1/\sqrt{N}$, the uncertainty of those values is much smaller.

The control and error spectra are taken using the SR785 as shown in Figure 3.3 and the calibrated results are shown in Figure 3.6. Also shown are the internal noise spectra for the SR785, which represent the measurement limits of the SR785. These were generated by terminating the inputs and taking the spectra to show the contribution from the internal electronics. For each measurement, the internal gain of the instrument is set to maximize the signal without exceeding the measurement limits. Since each measurement has potentially different voltage levels present in the measured signals, this gain will be different. Therefore, the contribution from the measurement noise can be different from measurement to measurement. For this and most measurements, measurement noise is significantly contributing to the control signal at very high frequencies, and measurement noise is contributing to the error signal at very low frequencies. At all other frequencies, the measurement noise is orders of magnitude smaller than the measured signal and can therefore be ignored.

These spectra can be examined to determine the disturbances on the cavity, as well as by how much those disturbances are suppressed. These disturbances are suppressed by applying the control signal to the actuator, and result in the error signal that is left over after the disturbances are suppressed. Nominally, the total disturbances to the cavity are the control spectrum for the disturbances for which the control system

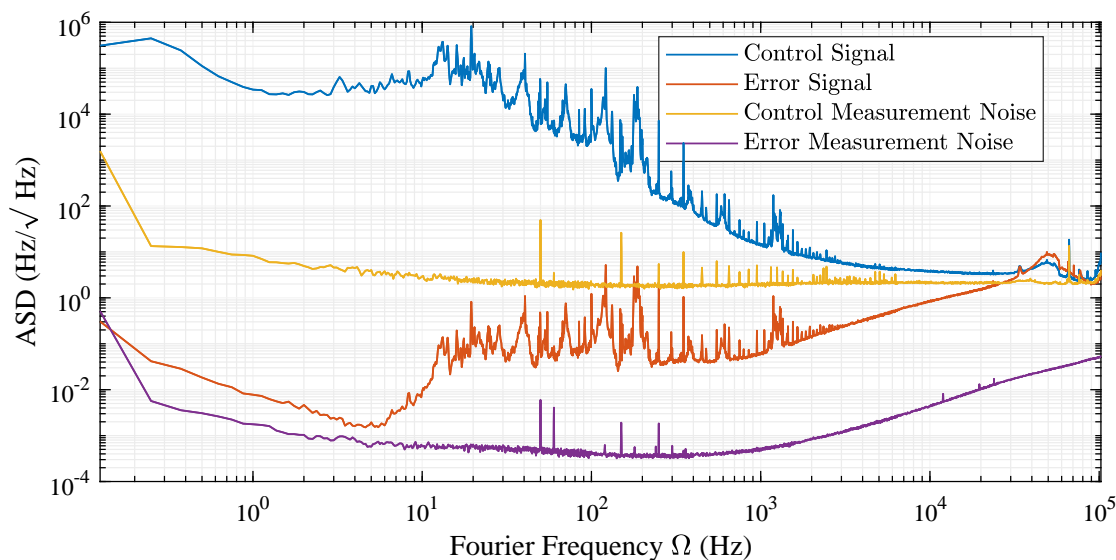


Figure 3.6.: Control and error signal amplitude spectral density for frequency control of the high power laser to match the ALPS IIa RC. The calibration of the control signal is (1.4 ± 0.2) MHz/V and the calibration for the error signal is (1.3 ± 0.2) MHz/V. The control signal is the signal sent to the laser piezo and the error signal is the signal sent to the control electronics. The noise seen at lower frequencies in the control signal is primarily caused by movements of the cavity mirrors, whereas the higher frequency noise is caused by laser frequency noise. The unity gain frequency is where the signals cross. The rise near that frequency is known as a servo bump and is due to oscillations in the control loop. The internal noise of the SR785 measurement system is also shown and limits the measurement of the control signal at high frequencies and error signal at low frequencies.

is compensating, and the error spectrum for the disturbances not compensated by the control system. However, some approximations can be made for certain frequency ranges. At frequencies well below the unity gain frequency, the error signal is much smaller than the control signal due to the high noise suppression in the loop. Thus, the disturbances of the cavity can be approximated as only the control signal. Close to the unity gain frequency, the control signal and the error signal are of similar sizes, and the combination of these signals shows the disturbances. Finally, at frequencies much higher than the unity gain frequency, the control signal is much smaller than the error signal as the control loop does not imprint the disturbances on the control signal, and as such the disturbances of the cavity can be approximated as just the error signal. In the spectra in Figure 3.6, the frequencies much higher than the unity gain frequency are omitted, and the measurement of the control signal is limited by the measurement noise of the SR785 in frequencies just higher.

The disturbances in the cavity can be separated into three categories: those due to mechanical vibrations, those due to laser frequency noise, and those due to the control

loop. The disturbances caused by the control loop include the so-called servo bump, which can be seen centered around 50 kHz, sensing noise, and control noise. The sensing noise is very small compared to the other noise sources, as we will see shortly. The control noise in the region of interest is generally neglected as it is quite small, and suppressed by the loop gain. The laser frequency noise of an NPRO laser is mostly smooth with a roughly $10 \text{ kHz}/\sqrt{\text{Hz}} \cdot (1 \text{ Hz}/f)$ behavior [55], which can be seen generally at frequencies above 250 Hz except for the contribution from the control noise. Finally, the mechanical noise includes the seismic motion of the ground and any mechanical resonances in the optical table, opto-mechanical components, thermal expansion and contraction, and other ways that couple physical motion into the optical system. Since this includes a collection of resonances, it is characterized by a collection of different resonance peaks. These peaks can be seen at frequencies from approximately 10 Hz to 250 Hz. At frequencies lower than that, individual peaks are not seen, but rather a longer-term seismic and thermal drift. These regions are seen similarly in previous measurements with additional measurement of seismic noise confirming the primary source of the motion in the lower frequency region [56].

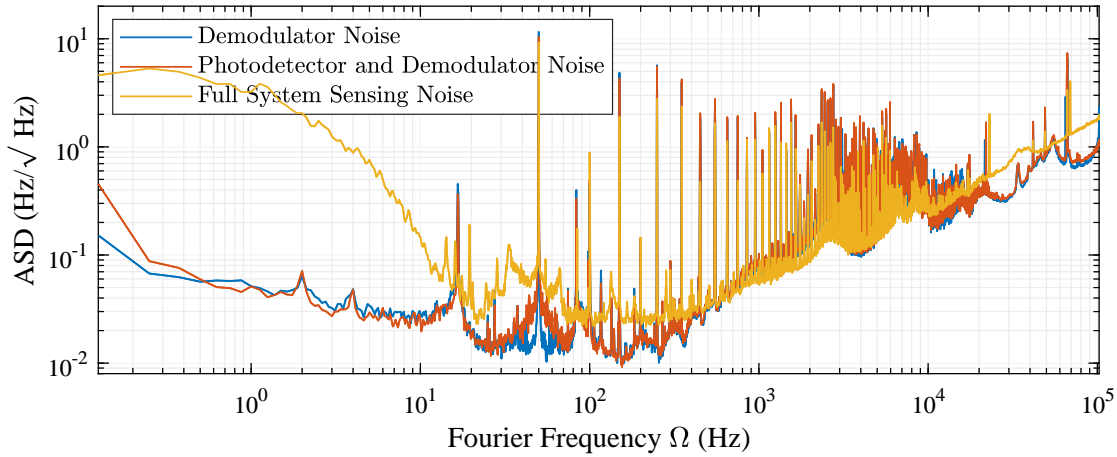


Figure 3.7.: Sensing noise of different components of the HPL sensing system. The blue curve represents noise only due to the demodulation electronics. This was measured by terminating the photodetector input of the demodulator and taking a spectrum of the output. The orange curve is taken with the photodetector plugged into the demodulator, but no light in the system. This represents the full electronic noise of the system. Finally, the yellow curve is taken with the laser on, but the cavity significantly misaligned so that no light is resonant in the cavity. This shows the noise on the light reflected from the cavity, which includes optical sources of noise as well as the same electronic sources measured in the previous curves. This is the full sensing noise of the system. This noise has been converted into frequency spectral density by applying the calibration and the cavity pole of the cavity.

As discussed in Chapter 2, sensing noise is the noise that the sensing system sees that is not present in the optical cavity. This includes noise that is purely electronic in origin,

as well as optical sources of noise, which will be examined in more detail in the following section. Noise detected with different sensing system components connected are shown in Figure 3.7. The blue curve represents noise only due to the demodulation electronics. This was measured by terminating the photodetector input of the demodulator and taking a spectrum of the output. The orange curve is taken with the photodetector plugged into the demodulator, but no light in the system. This represents the full electronic noise of the system. Finally, the yellow curve is taken with the laser on, but the cavity significantly misaligned so that no light is resonant in the cavity. This shows the noise on the light reflected from the cavity, which includes optical sources of noise as well as the same electronic sources measured in the previous curves. This is the full sensing noise of the system. This noise has been converted into frequency spectral density by applying the calibration and the cavity pole of the cavity.

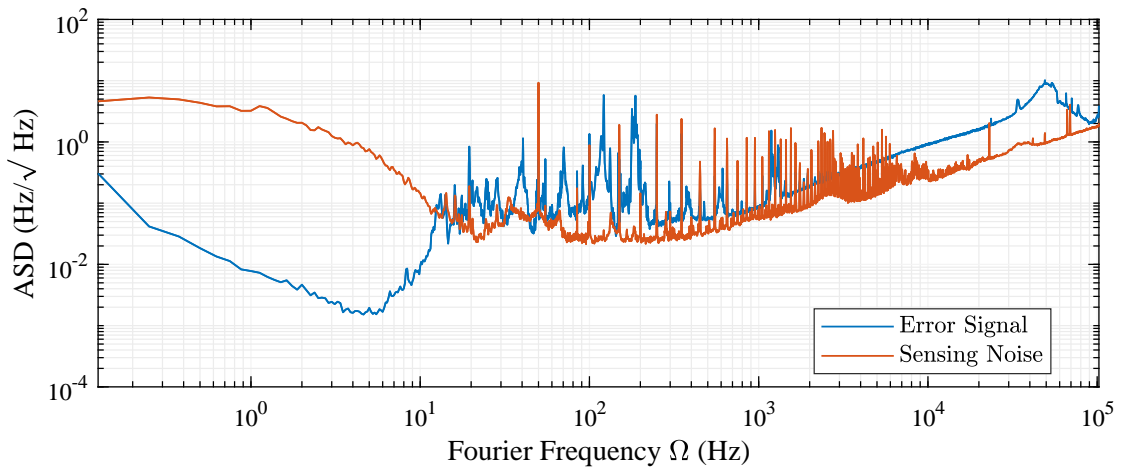


Figure 3.8.: Error compared to sensing noise amplitude spectral density for frequency control of the high power laser to match the ALPS IIa RC. The error spectrum is the same as shown in Figure 3.6 and the sensing noise is the same as shown in Figure 3.7. The regions where the error signal is below the sensing noise are regions where the control loop is suppressing noise that is present only in the sensing system, and thus imprinting that noise on the cavity.

The sensing noise compared to the error signal ASD is shown in Figure 3.8. The sensing noise exceeds the error signal spectrum only at a few points between 10 Hz and 100 Hz, then at all frequencies below 10 Hz. At higher frequencies, other than the harmonics of 50 Hz, the sensing noise is lower than the error signal, though never becoming negligible. This indicates that some of the noise being suppressed is noise present only in the sensing system. This noise is not actually present in the cavity and is thus being imprinted on the difference between the laser frequency and the resonant frequency of the cavity. In this way, the sensing noise represents a limit on the noise suppression of the cavity, and also a limit of using the in-loop error signal to sense the mis-match between the laser frequency and the cavity resonant frequency. A more detailed discussion of the source

and effects of this noise is present in the following section.

3.3. Green Frequency Control

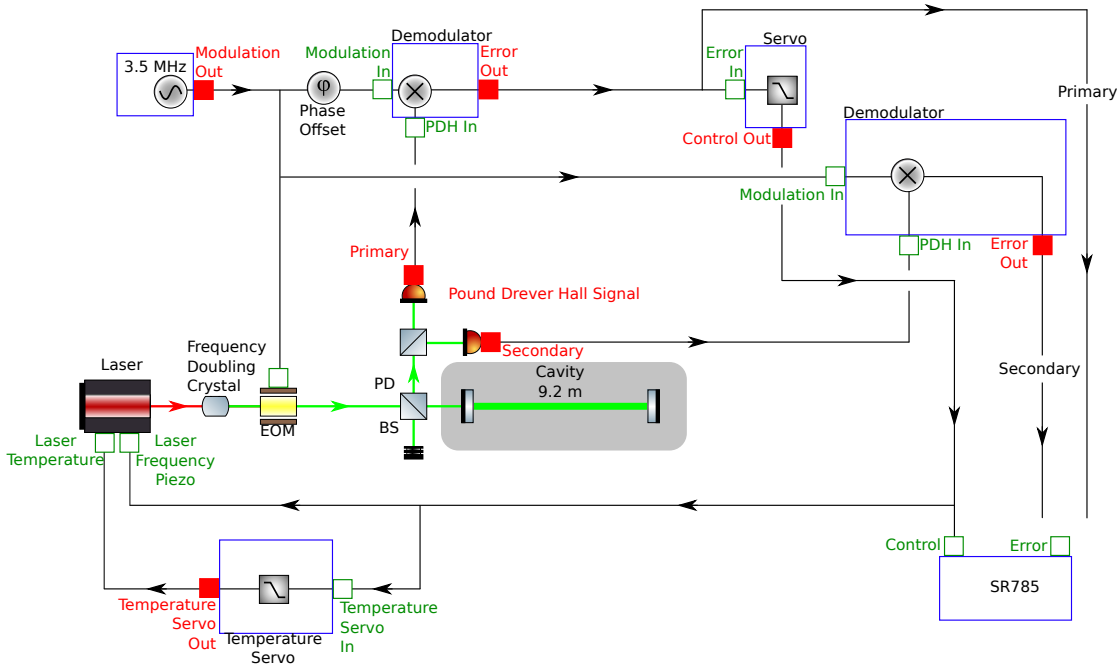


Figure 3.9.: Feedback control system to match frequency doubled reference laser to the ALPS IIa regeneration cavity and measure the performance of this control. This system is similar to the system in Figure 3.3. The first difference is that the modulation frequency is 3.5 MHz. The second difference is the inclusion of a frequency doubling sub-system to convert the IR light into green light. The final difference is the inclusion of a secondary error sensing path.

As discussed in Section 1.5, since no infrared light can be used for sensing the cavity resonant frequency in the TES detection scheme, a scheme to generate green light by frequency doubling an infrared laser and then probe the cavity length with that laser is necessary. After the frequency doubling of the laser beam, the method for control is identical to the control system for the HPL as shown in Figure 3.3 with the addition of another error signal path for measurement purposes. The total schematic is shown in Figure 3.9.

In this system, the reflected light carrying the interference between the light resonating in the cavity and the sidebands is split between two photodetectors: the primary that senses the signal sent to the control loop, and the secondary that is only used to measure the light interacting with the cavity. Either the primary or the secondary sensing path can be measured using the SR785. The reason for having two measurement signals is that the primary and secondary error signal paths do not experience noise from exactly the

same sources, so a lot of the noise measured by the sensing paths will be uncorrelated. Since at least the electronic noise is different between the two, mostly independent, sensing paths, any sensing noise that is imprinted on the cavity by the control loop should appear clearly on the secondary sensing path. This is not a true out-of-loop sensing method, as there may be sources of noise that affect the PDH error signal such that this signal does not accurately describe the behavior of the light in the cavity and its relationship with the resonance of the cavity. However, even having a secondary sensing path that is not electronically in the same loop will give us a better idea as to the true behavior of the light and cavity than the in-loop signal. This is especially important when measuring systems in Chapters 4 and 5, where in-loop signals are not available, and we will see that there are a number of difference between the in-loop primary sensing path to the secondary sensing path.

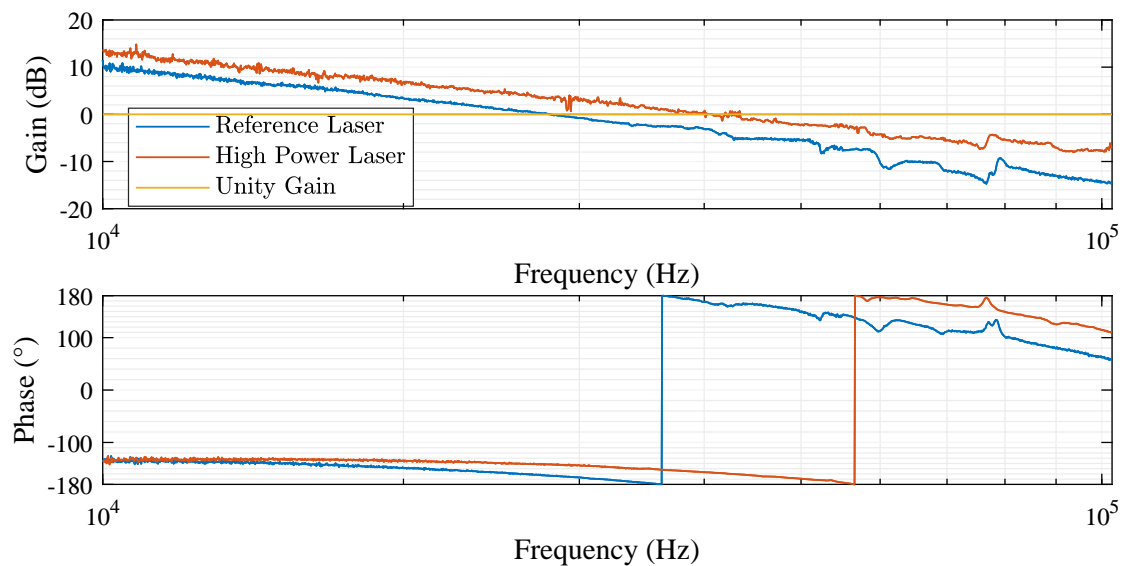


Figure 3.10.: Open-loop transfer function for the frequency-doubled reference laser frequency control system compared to the high power laser frequency control system. The unity gain frequency of the reference laser system is 28 kHz with a phase margin of 17° and the system parameters for the high power laser system are in Figure 3.4. Both transfer functions were measured by injecting a swept sine on the control signal and comparing the control signal with the swept sine to the control signal right before the swept sine was injected. The measurements were made with an averaging factor of 100 and an input of between 0.1 mV and 5 mV peak-to-peak.

Figure 3.10 shows the open-loop transfer function of the frequency-doubled RL frequency control system compared to the HPL frequency control system. There is more phase loss in the RL control system, and as such we were unable to set the proportional gain as high as the HPL system. This phase loss could be due to an additional time delay in the RL control system or an additional control feature such as a low-pass or notch in the RL system that is not immediately apparent in the magnitude of the transfer func-

tion at these frequencies. As these and other analog control systems were already in-use and optimized independently of this work, they are mostly treated as black boxes for the purposes of this thesis. The unity gain frequency for the RL system is 28 kHz with a phase margin of 17° compared to the HPL system which has a unity gain frequency of 40 kHz and a phase margin of 23° .

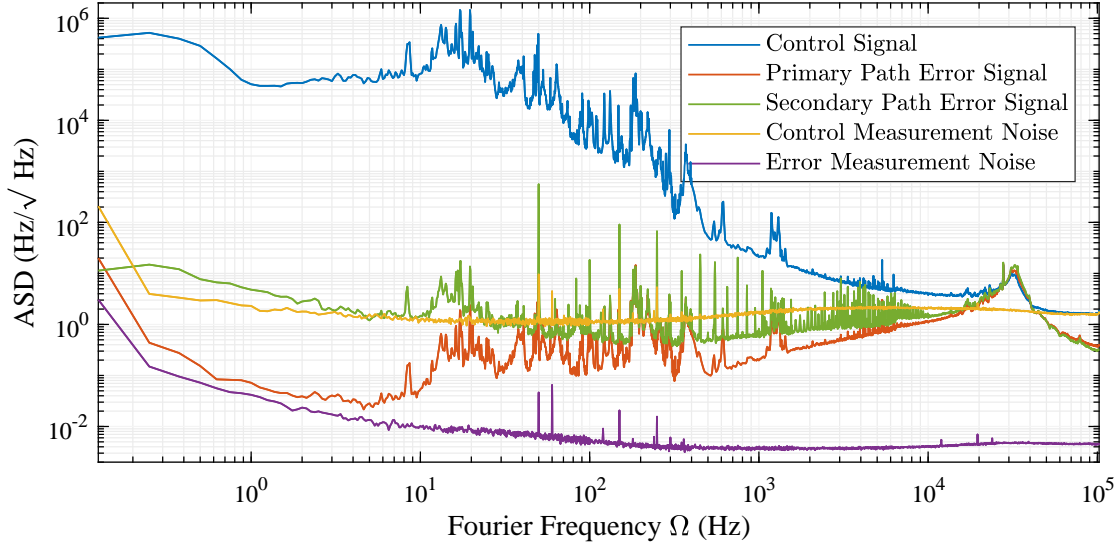


Figure 3.11.: Control and error spectra for green frequency control. The control signal is the signal sent to the laser piezo. One of the error signals is the signal sent to the control electronics and the other one is processed in the same way but measured by a separate photodetector as shown in Figure 3.9. The noise seen at lower frequencies in the control signal is primarily caused by movements of the cavity mirrors, whereas the higher frequency noise is caused by laser frequency noise. The unity gain frequency is where the signals cross. The rise near that frequency is known as a servo bump and is due to oscillations in the control loop. The internal noise of the SR785 measurement system is also shown and limits the measurement of the control signal at high frequencies and the primary path error signal at low frequencies.

The control and error signal are similar to those presented for the HPL frequency control in Figure 3.6. They can be seen in Figure 3.11. Just as with the HPL, the control spectrum is shown in blue, with the measurement limits of the SR785 shown in yellow. The primary PD measurement is shown in orange, with the measurement limits in purple. The measurement of the control spectrum is limited by the noise of the SR785 above the unity gain frequency, and the error spectrum through the primary PD is limited at low frequencies by the measurement noise in that channel. The significant addition to this plot is the inclusion of the secondary PD error spectrum, which is not part of the control loop. The secondary detection path shows more noise than the primary path at almost all frequencies. The cavity pole is not included for the analysis of any green measurements as the corner frequency is close to the maximum frequency measured and has a minimal effect on the spectrum.

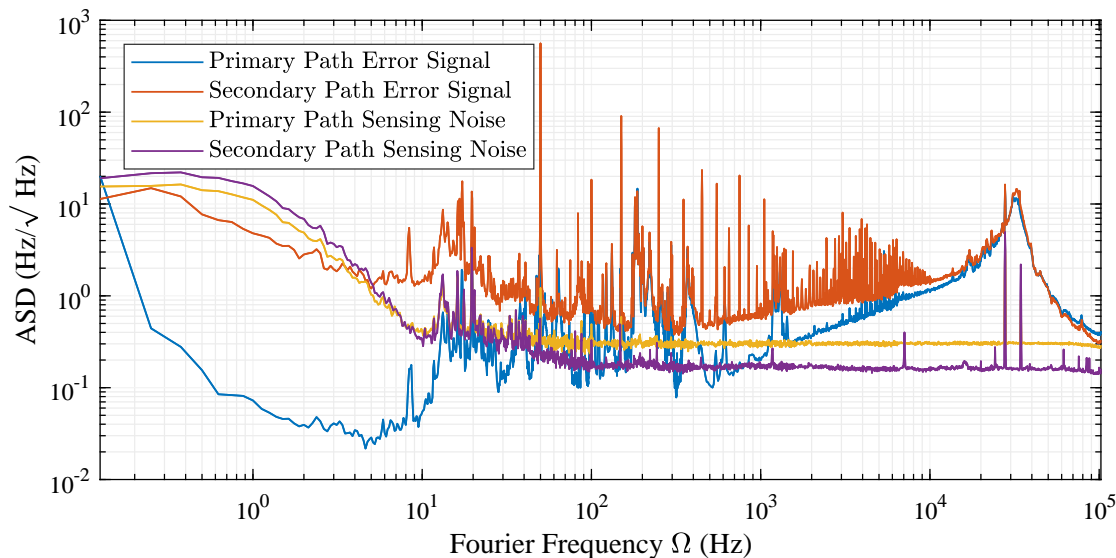


Figure 3.12.: Primary and secondary sensing path error compared to sensing noise amplitude spectral density for frequency control of the reference laser. The primary and secondary path error signal are the same as shown in Figure 3.11. The sensing noise will be discussed more thoroughly in Figures 3.13 and 3.14.

This difference between the primary and secondary sensing paths is particularly interesting. These signals are shown in Figure 3.12 compared with the sensing noise. The primary sensing path spectrum is lower than the sensing noise spectrum in that path. As with the HPL frequency control in Figure 3.8, this is because the sensing noise is suppressed just as if it were a disturbance of the cavity, leading to extra noise in the cavity. As previously discussed, the noise in the secondary sensing path is mostly uncorrelated with the noise in the primary sensing path, and so it can more accurately show the noise present on the light in the cavity than the primary sensing path. The secondary sensing path also has sensing noise that is added to the noise measured by that path, so the sensing noise in that path must also be considered for its contribution to the measurement.

For the most part, the error spectrum from the secondary path is not exactly what would be expected from the combination of the primary sensing path spectrum, the primary sensing noise spectrum being imprinted on the cavity, and the secondary sensing path noise. At high frequencies when the suppressed noise is much larger than the sensing noises, the primary and secondary have very similar spectra as the sensing noise does not have a significant effect on these frequencies. Going lower in frequency, however, the error spectra from the primary and secondary spectra diverge in a way that is more than what would be the result from the sensing noise shown, except for peaks where the suppressed noise is significantly larger than the sensing noise. At lower frequencies, the spectra start to diverge in the opposite direction. At frequencies below 10 Hz, the sensing noise is of each sensing channel is larger than the error spectrum in the secondary

sensing channel. In order to understand these regions, we must look at the source of the sensing noise.

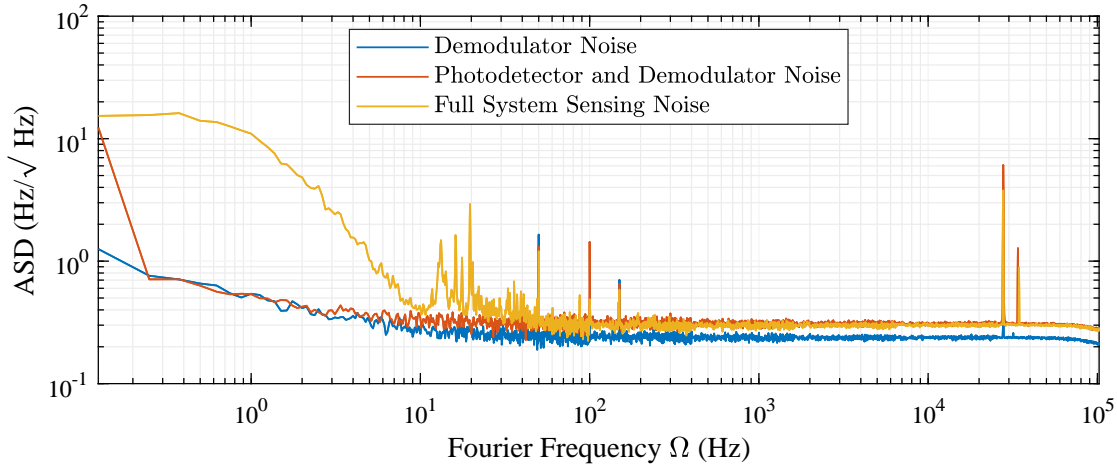


Figure 3.13.: Sensing noise of different components of the primary RL sensing system. The blue curve represents noise only due to the demodulation electronics. This was measured by terminating the photodetector input of the demodulator and taking a spectrum of the output. The orange curve is taken with the photodetector plugged into the demodulator, but no light in the system. This represents the full electronic noise of the system. Finally, the yellow curve is taken with the laser on, but the cavity significantly misaligned so that no light is resonant in the cavity. This shows the noise on the light reflected from the cavity, which includes optical sources of noise as well as the same electronic sources measured in the previous curves. This is the full sensing noise of the system. This noise has been converted into frequency spectral density by applying the calibration of of the error signal.

Figure 3.13 shows the sensing noise of the primary detection path as the configuration gets closer to the full detection system. The blue curve is the noise output of the demodulator with the input terminated. This is relatively flat except at low frequencies where it does show a smooth rise at frequencies lower than approximately 10 Hz. The orange curve is with the photodetector plugged into the demodulator, but there is no laser light incident on the cavity or on the photodetector. This shows a slightly higher flat behavior at frequencies larger than 10 Hz, but lower than that the demodulator noise dominates. This represents the electronic noise of the system. The final, yellow curve is with the photodetector plugged into the demodulator with the laser on. In order to not have any signals due to light briefly resonating in the cavity as the laser and cavity drift, the second mirror of the cavity was significantly misaligned so as not to allow a closed beam path between the two mirrors. This curve shows a significant amount of additional noise at frequencies under 50 Hz. Between 10 and 50 Hz, there are some peaks and below 10 Hz, there is a significant rise. This rise in noise is entirely optical in nature as the only difference between the red and yellow curves is the laser light.

The behavior is very similar with the secondary detection path in Figure 3.14. The

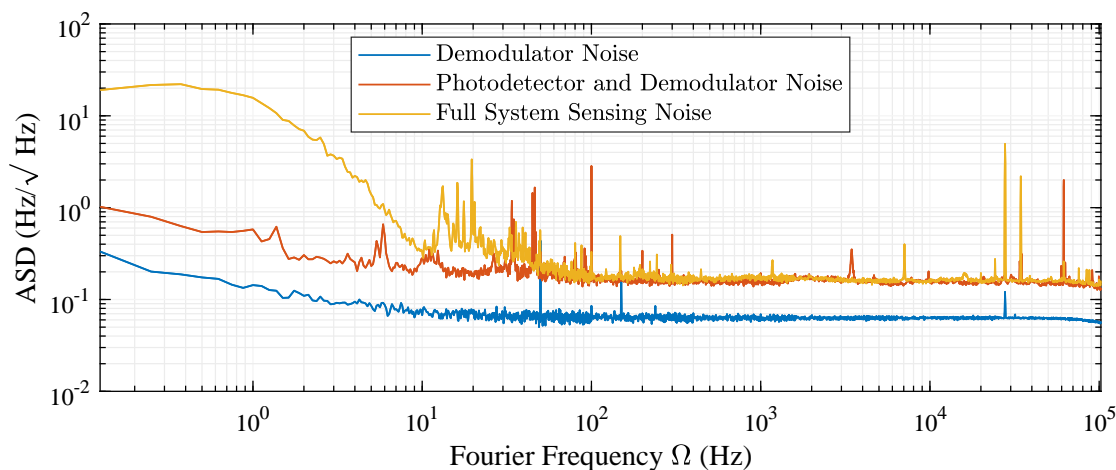


Figure 3.14.: Sensing noise produced at different parts of the secondary detection path. The blue curve represents noise only due to the demodulation electronics. This was measured by terminating the photodetector input of the demodulator and taking a spectrum of the output. The orange curve is taken with the photodetector plugged into the demodulator, but no light in the system. This represents the full electronic noise of the system. Finally, the yellow curve is taken with the laser on, but the cavity significantly misaligned so that no light is resonant in the cavity. This shows the noise on the light reflected from the cavity, which includes optical sources of noise as well as the same electronic sources measured in the previous curves. This is the full sensing noise of the system. This noise has been converted into frequency spectral density by applying the calibration of of the error signal.

primary difference is that the photodetector has a higher level of gain. As such, the electronic signal from the photodetector for the same measured frequency noise is much larger. This changes the calibration of the error signal such that the contribution to the sensing noise due to the demodulator is smaller, even though the electronic noise from the demodulator is the same for both sensing paths. However, the behavior at low frequencies is the same for both sensing paths as this noise is from an optical source.

The sensing noise from the detection electronics is not the only source of electronic noise. In addition to the electronics used for detection and demodulation of the error signal, there is an additional device used to ensure that the error input to the servo is centered around the ideal operating point. Though the ideal error signal always is at zero when the cavity is a perfect resonance, different effects can cause changes to this and the easiest way to cancel out these effects is to change the offset voltage of the signal going into the servo with a device known as an offset box. However, the use of additional electronics can introduce the possibility of extra noise from interference loops from power sources, or a number of other effects. The noise seen from the demodulator compared with the demodulator directly plugged into the servo and the demodulator signal running through the offset box is shown in Figure 3.15. Since this noise is electronic in nature, it depends on the exact electronic setup and these measurements were not done at either

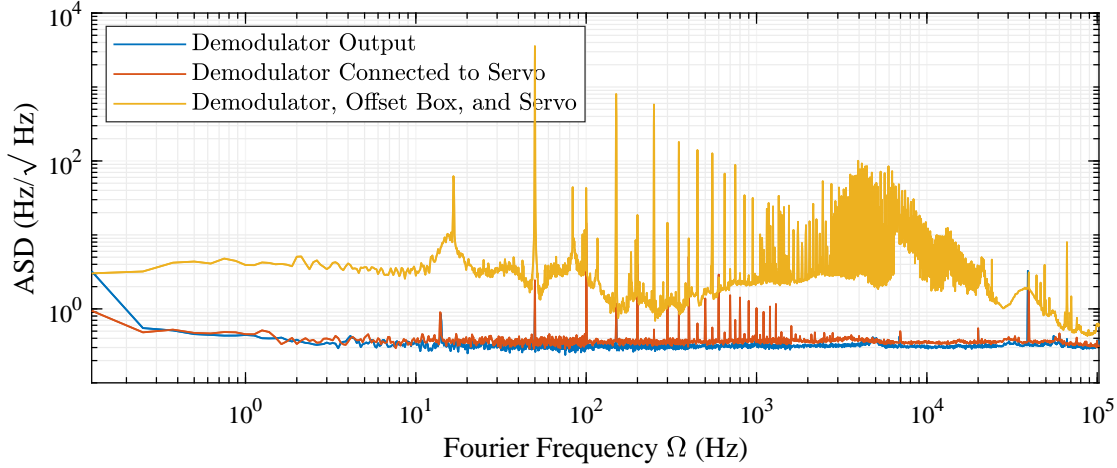


Figure 3.15.: Electronic noise from electronics to control the offset of the error signal. These devices are known as offset boxes. All measurements were made with the input of the demodulator terminated. The blue curve is measuring the output of the demodulator only, and the orange curve is measuring the input of the servo with the terminated demodulator connected to it. The yellow curve is measured by plugging the output of the terminated demodulator into the input of the offset box, and the output of that offset box to the input of the servo. This shows that the offset box can add a significant amount of electronic noise when used in a setup similar to the one used for controlling the optical cavities. This noise has been converted into frequency spectral density by applying the calibration of of the error signal.

the same time or with the setup used to make the other measurements in this section. As such, the noise measured here cannot be directly compared with the noise measured in Figure 3.12. The noise shape is similar in many ways to the additional noise, though it does not exactly match, and the magnitude of the noise is much larger than would produce the measured frequency noise. The additional noise in that figure could be due to this offset box, but it is not definitive.

As a note, the power at the photodetector for all measurements of green light was between $30 \mu\text{W}$ and $50 \mu\text{W}$, corresponding to a shot noise level $<0.01 \text{ Hz}/\sqrt{\text{Hz}}$, which is well below the other sources of noise.

One potential optical cause of sensing noise is residual amplitude modulation (RAM) from the EOM applying the phase modulation sidebands for the PDH sensing system. The EOM should have no effect on the amplitude of the beam. However, a number of effects can cause an amplitude modulation at the same frequency as phase modulation [57]. This causes changes on the signal present on the photodetector for a perfect PDH scheme shown in Equation 1.44. The most important change for frequency measurements is that the terms that are DC in that equation actually have some amplitude modulation at the modulation frequency applied to the EOM. When the demodulation is applied, these oscillating terms that are not part of the perfect PDH signal still remain. By this mechanism, any modulation on the incident power can couple into the error signal. This

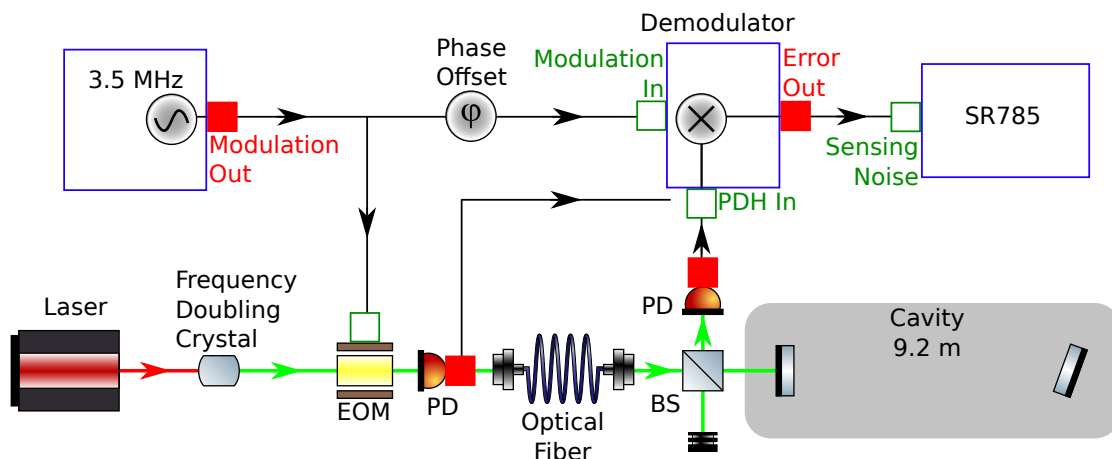


Figure 3.16.: Experimental setup to investigate RAM as an optical source of sensing noise. This setup compares the optical sensing noise with the photodetector in the nominal PDH position with the light directly after the EOM. Any RAM should be present at all points after the EOM.

can be investigated by comparing the sensing noise of the system to the demodulated input of the optical system. In the case of RAM being the source of the sensing noise, we would expect this noise to be present at all points after the EOM. An experimental setup to investigate this is shown in Figure 3.16. A photodetector is placed before the optical fiber that couples the light into the optical system and compared to the result when the photodetector is placed in the normal position for PDH sensing.

Figure 3.17 shows the results of the full system sensing noise compared to the demodulated noise measured before the optical fiber. The blue curve is the sensing noise of the full system with the photodetector in the nominal position for PDH sensing. The orange curve is measured with the photodetector before the fiber input to the system with similar power on the photodetector for a direct comparison. The yellow curve is the same as the orange curve, but with significantly more power on the photodetector. As the optical signal is proportional to the power on the beam, we expect a higher power to produce a larger signal for all effects, including RAM, which would help any effects of RAM to exceed the electronic noise of the system that is independent of optical power. The purple curve is the electronic noise of the photodetector and demodulator with no light in the system for comparison.

This measurement shows that, though there is some RAM present in the beam from the EOM, it is significantly smaller than the noise seen in the system. Another possible noise source is stray light producing interference on the photodetector at very low levels compared to the interference from the light in the RC. As the surfaces from which this stray light is reflecting move, the optical path length changes, which leads to phase changes between the stray light and the light interacting with the cavity. These phase changes show up as the frequency noise seen in these measurements. This stray light

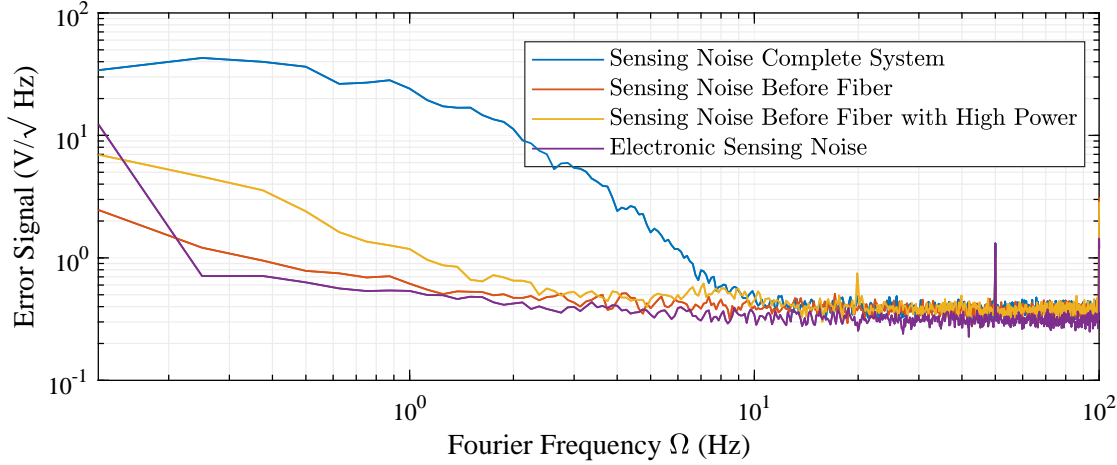


Figure 3.17.: Optical sensing noise before and after sensing system. The sensing noise of the complete system is measured with the photodetector in the standard position for PDH sensing but the cavity misaligned so light cannot be resonant with the cavity. The two curves of the noise before the fiber are measured with the light directly on the photodetector before the fiber to look for RAM from the EOM. The orange curve is the same amount of power on the photodetector as when it is in the nominal position for PDH sensing and the yellow curve is with 3-4 times that amount of power incident on the photodetector so that any optical effects are larger while the electronic noise stays the same. The electronic sensing noise is with all of the electronic elements in the setup, but no light in the system.

is reflecting off of many surfaces, and therefore not all of the noise due to this light is be correlated between the two detectors. All noise present in the primary sensing path is suppressed, including this stray light noise, which will be imprinted on the light incident on the cavity. Any of that suppressed noise that is correlated with the noise on the secondary path will also be suppressed on both paths. Though it is present on the cavity, the secondary sensing path will not detect it. For noise on the primary sensing path that is not correlated with the noise on the secondary path, the imprinted noise will be detected by the secondary path. Finally, noise that is present on the secondary sensing path that is not correlated with noise on the primary sensing path will be detected by the secondary sensing path, though it is not present on the light incident on the cavity. It is possible this light that is correlated between the two paths that causes the noise detected by the secondary path to be smaller than the noise in either sensing path.

3.4. Green Length Control

The frequency control of the HPL to match the PC allows light to build up to enhance the probability of axion-like particle generation, and the frequency control of the RL to match the RC enables sensing of the resonant frequency of the RC. To match the resonant frequency of the two cavities requires actuating on the length of at least one

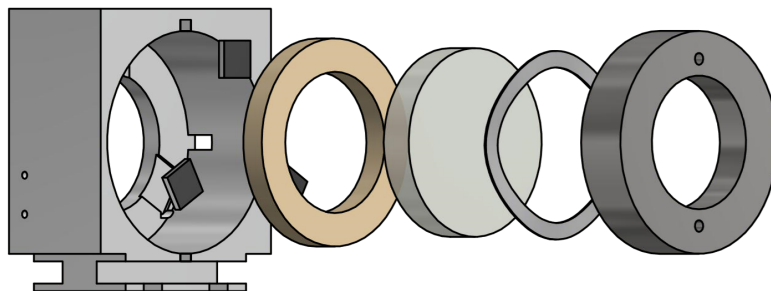


Figure 3.18.: A schematic drawing of the components of the mirror actuator. It includes from left to right, the mirror mount, three small piezos, a large ring piezo, the cavity end mirror, a wave washer to provide restoring force, and the retaining ring to compress the wave washer.

cavity. To this end, it is important to be able to control the length of the cavity, and optimize that control scheme.

The biggest challenge for length actuation is that the end mirror needs to be relatively large to accommodate the large beams in the cavities of ALPS IIc. Moving this mirror requires imparting more inertia than applying a stress to the laser crystal, and therefore responds much more slowly than similar changes for the NPRO laser frequency. The mirror being used for ALPS IIa is similar to the one that will be used in ALPS IIc and is 50.8 mm in diameter with a mass of 43 g [46]. The system used to mount the mirror with a large piezo electric actuator is shown in Figure 3.18 and was custom designed for use in ALPS IIa and ALPS IIc. The mount is designed to hold three small piezos that were intended to actuate on the pitch and yaw of the mirror. Next in the stack is the ring piezo element for length actuation. Directly next to the piezo is the mirror which is held against the piezo with a wave washer providing restoring force to the mirror so that the mirror is constantly pressed against the piezo element both when it expands and when it contracts. Finally, all of the elements are held in place with a retaining ring that is screwed into place to provide an initial compression of the wave washer to increase the restoring force. These elements provide actuation of the cavity mirror for use in the length control system. Further discussions of the design of this actuator and an iteration on this design can be found in Section 3.5.

Since it is larger and more massive, thus making it much slower, it is likely that this actuator will limit the performance of the system much more than the frequency actuator did. Understanding how much it will limit the performance requires measuring its transfer function in the relevant environment. In order to achieve this, we used the frequency control system as a probe for the cavity length. The control signal of this system below the unity gain frequency reflects the majority of the cavity disturbances. So by inducing a length disturbance at different frequencies by driving the mirror actuator at those frequencies and comparing the control signal to the signal driving the mirror, we are able to know what the motion of the mirror actuator induced by the input signal is.

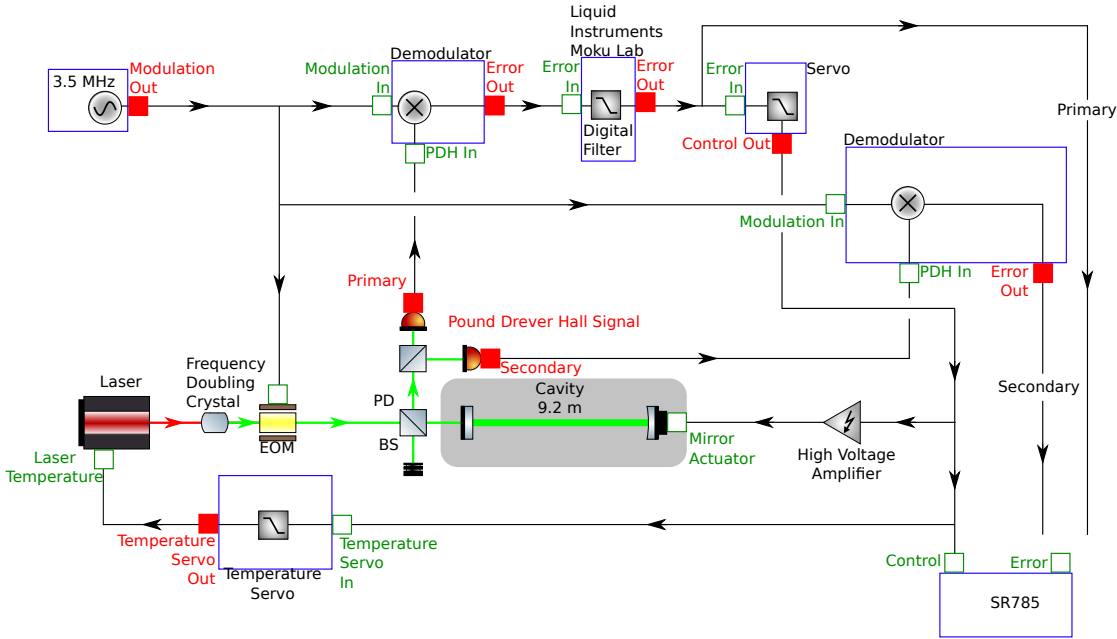


Figure 3.19.: Schematic of length control with digital filtering. This is similar to the schematic shown in Figure 3.9 with a few differences. The first difference is the inclusion of the Liquid Instruments Moku Lab between the demodulator output and the servo input. This filters the error signal to reduce the effect of cavity resonances. The second major difference is that the control signal is being sent through a high voltage amplifier to the mirror actuator rather than being sent to the laser frequency actuator.

The results of this measurement are shown in the blue curve in Figure 3.20. The first resonance in this transfer function is located at 4.88 kHz with a larger one at 5.3 kHz. These resonances significantly limit the proportional gain of the system. Using a servo with a $1/f$ gain slope near the unity gain frequency, the best unity gain frequency achieved with these resonances is 900 Hz. However, there is a significant phase margin. This phase margin remains at much higher frequencies, which allows additional filtering to allow us to increase the proportional gain and achieve a higher unity gain frequency. In this instance, the significantly higher granularity and precision available in digital filters over analog electronics makes a digital system the preferred option for this application.

For this control system, we defined the filter in a Moku Lab FPGA-based system produced by Liquid Instruments which filtered the error signal before being fed to the length servo which provided the additional filtering necessary to generate the control signal. The schematic of this control scheme is shown in Figure 3.19. After generating the control signal, it is split and sent to the temperature frequency-actuator of the laser control as with the frequency control schemes in Figures 3.3 and 3.9, which should increase the dynamic range but will not be possible in the length control system in ALPS IIc which must actuate entirely on length. A system for high dynamic range

length actuation was not installed in ALPS IIa at the time of these experiments, so the temperature was used instead. The control signal path that is not sent to the temperature control system is sent through a high voltage amplifier in order to generate the voltages required to generate motion of the end mirror.

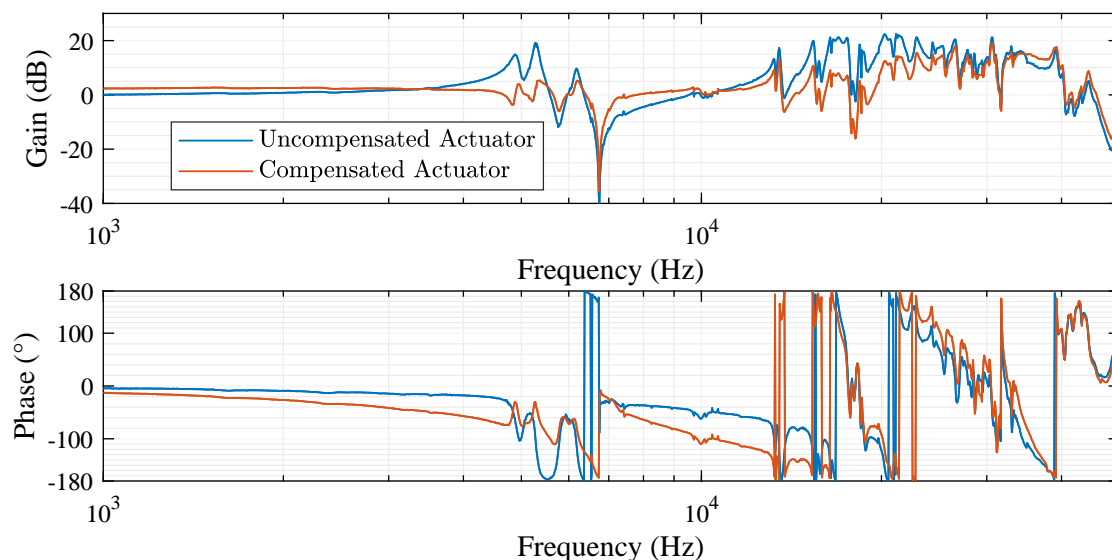


Figure 3.20.: The transfer function of the mirror actuator resonance compensation. The uncompensated transfer function has the first resonance located at 4.88 kHz with a larger one at 5.3 kHz. The filter was uploaded to the Liquid Instruments Moku Lab and applied to the error signal before being sent to the length control servo, and results in the orange transfer function. The resonances are much smaller and there is some phase loss from the compensation. Both transfer functions were measured by engaging the control loop discussed in Section 3.3 and comparing a swept sine sent to the high voltage amplifier connected to the mirror actuator to the control signal of the frequency control loop at those frequencies. The measurements were made with an averaging factor of 100 and an input of between 0.1 mV and 50 mV peak-to-peak.

Zeros	Poles
-4850 Hz(0.010 - 1.000 <i>i</i>)	-5000 Hz(0.021 - 1.031 <i>i</i>)
-5250 Hz(0.008 - 1.000 <i>i</i>)	-5750 Hz(0.038 - 1.095 <i>i</i>)
-6150 Hz(0.018 - 1.000 <i>i</i>)	-6500 Hz(0.084 - 1.054 <i>i</i>)
-17 700 Hz(0.100 - 0.995 <i>i</i>)	-17 700 Hz(0.981 - 0.196 <i>i</i>)

Table 3.1.: Zeros and poles for mirror actuator resonance compensation. The complex conjugates are omitted.

The filtering provided by the Moku should reduce the gain at resonances to counteract the increased response at those frequencies, and use any parts where there is lower

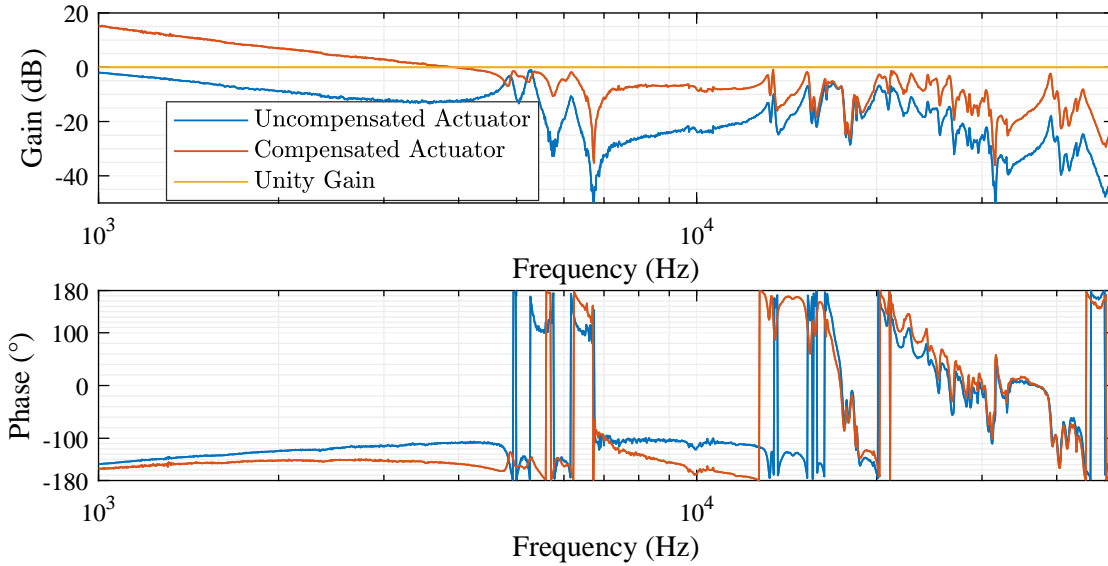


Figure 3.21.: Comparison of length control open-loop transfer function with and without compensation. The uncompensated system was able to achieve a unity gain frequency of 900 Hz and the compensated system was able to achieve a unity gain frequency of 3.9 kHz. Both transfer functions were measured by injecting a swept sine on the control signal before the high voltage amplifier and comparing the control signal with the swept sine to the control signal right before the swept sine was injected. The measurements were made with an averaging factor of 100 and an input of between 0.1 mV and 5 mV peak-to-peak.

response to introduce an additional resonance to limit the phase lag. The poles and zeros used to define this filter are shown in 3.1 with the complex conjugates omitted. They were determined by tuning the frequency and the size of the real part of the coefficients in order to achieve the maximum suppression of the resonances while still maintaining enough phase margin at the unity gain frequency. When the driving signal to the piezo is fed through this filter, we end up with a much flatter transfer function compared to the original. Both transfer functions are shown in Figure 3.20. There is some phase loss from the compensation, but there is still enough phase for a $1/f$ slope at the unity gain frequency. Using this compensation, we are able to achieve a unity gain frequency of 3.9 kHz with a phase margin of 32° . The open-loop transfer functions of the uncompensated and compensated control systems are shown in Figure 3.21. The compensation of the resonances is not completely perfect, so though the size of them is greatly reduced, they are not completely eliminated. This means that the proportional gain cannot be turned up past the point where these resonances end up above unity gain in the transfer function without introducing a significant amount of noise due to uncontrolled oscillations at these resonance frequencies. As such, the proportional gain cannot be turned up to the point where the phase margin available at the unity gain frequency results in a noticeable servo bump. For this reason, the phase margin is larger

than it would otherwise need to be in order to prevent the oscillations around the unity gain frequency because we are limited instead by the resonances of the mirror actuator that are not perfectly compensated by the Moku filtering.

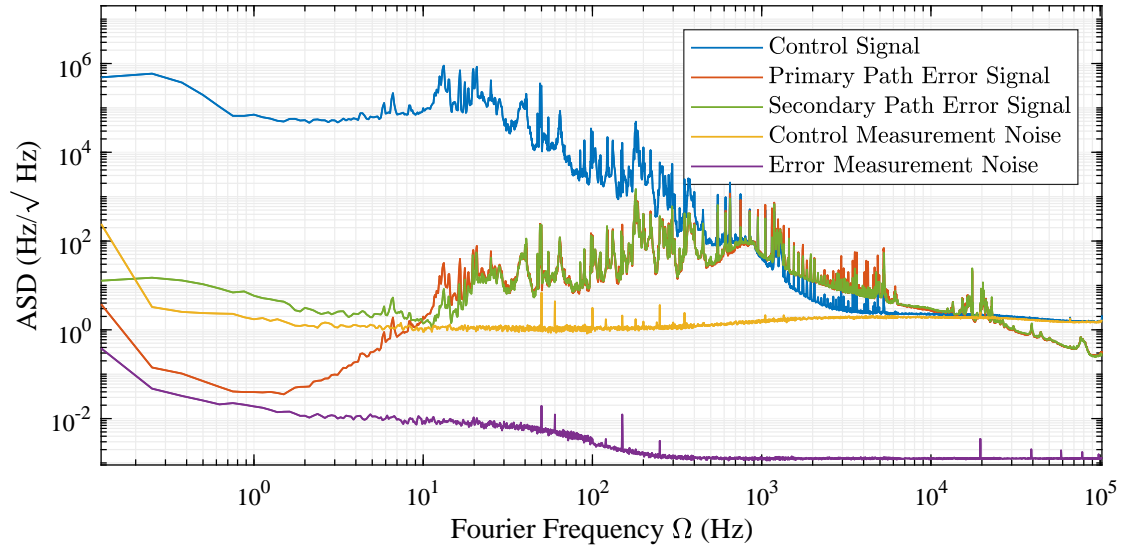


Figure 3.22.: Control and error spectra for length control without compensating for actuator resonances. The control signal is the signal sent to the high voltage amplifier that is then sent to the mirror actuator. One of the error signals is the signal sent to the control electronics and the other one is processed in the same way but measured by a separate photodetector as shown in Figure 3.19. The noise seen at lower frequencies in the control signal is primarily caused by movements of the cavity mirrors, whereas the higher frequency noise is caused by laser frequency noise. The unity gain frequency is where the signals cross. The uncompensated mirror actuator resonances in Figure 3.20 can be seen in both the control and error signal. The internal noise of the SR785 measurement system is also shown and limits the measurement of the control signal at high frequencies and the primary path error signal at low frequencies.

The control and error spectra for the uncompensated system are shown in Figure 3.22. Just as in Figure 3.11, the blue curve shows the control spectrum, and the orange and green curves show the primary and secondary PD error spectra, respectively. Finally, the measurement limits of the SR785 for the control spectrum are shown in yellow and the error spectrum are shown in purple. Since there is not as much gain as with the frequency control system in Section 3.3, the sensing noise does not limit the suppression seen in the secondary sensing path except at frequencies below 20 Hz.

The Moku adds noise to the system both from its ADC and digital to analog converter (DAC). Unlike the DAC noise for a completely digital control system, this DAC noise is on the error point of the servo and is therefore not suppressed by the control system but is instead imprinted on the plant. It is important to understand the noise of a system using the Moku as a filter compared to the analog system noise as well as any extra noise that it introduces. The noise from each source is shown in Figure 3.23.

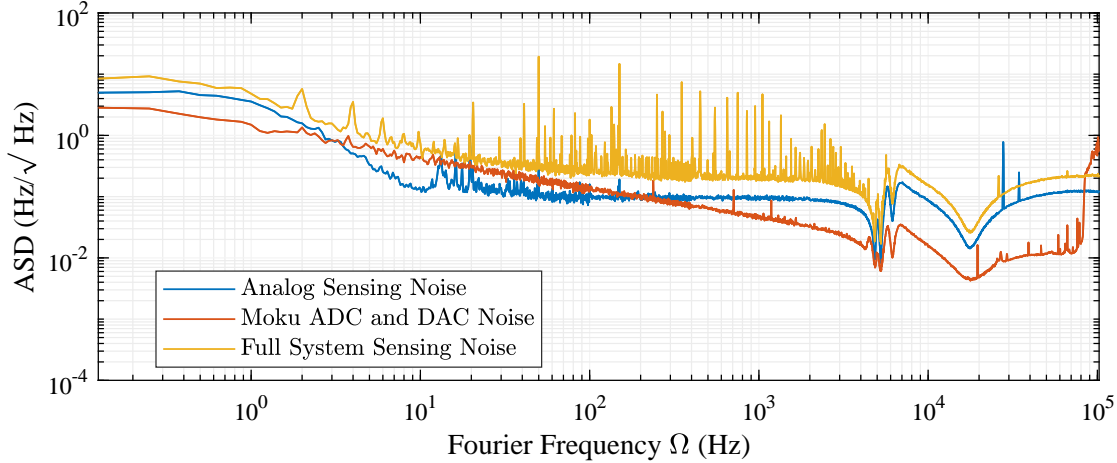


Figure 3.23.: Sensing noise produced by the analog and digital parts of the error path. The blue curve is the full analog sensing noise measured by taking the output of the demodulator with the laser on, but the cavity significantly misaligned so that no light is resonant in the cavity. This shows the noise on the light reflected from the cavity, and all electronic sources of noise. The orange curve is the noise of the Moku including the ADC, DAC, and any internal noise sources. This was taken by terminating the input to the Moku and measuring the output. Finally, the yellow curve is the combination of all noise sources. This was taken by connecting the full sensing primary path, including the Moku, and measuring the output with the laser on, but the cavity significantly misaligned so that no light is resonant in the cavity. This should include all optical and electronic sources of noise. This noise has been converted into frequency spectral density by applying the calibration of of the error signal.

These noise measurements are for the noise on the input of the control servo, after any Moku filtering. For this reason, the analog sensing noise has the filtering and some gain applied to it to simulate what the sensing noise would look like for an analog filter implementation. The full noise of the system, however, exceeds the noise of the Moku combined with the analog sensing noise at frequencies above approximately 10 Hz. This is likely due to the same offset box discussed in the previous section.

The control and error spectra for the compensated system are shown in Figure 3.24. The curves shown are very similar as those in Figure 3.22, but with more gain provided by the higher proportional gain available with the reduction of the resonances. Just as with the uncompensated system, the secondary path spectrum only diverges from the primary path spectrum at frequencies below 20 Hz. For all other frequencies, the system is limited by gain more than it is limited by the sensing noise of the system. This can be more clearly seen in Figure 3.25, comparing the error spectra from the different detection paths with the sensing noise of those paths. We can see that both error spectra are much larger than the sensing noise for all frequencies above 20 Hz.

The higher proportional gain achieved with digital filtering more than counteracts the increased noise by using the Moku, as the noise added by the Moku does not significantly

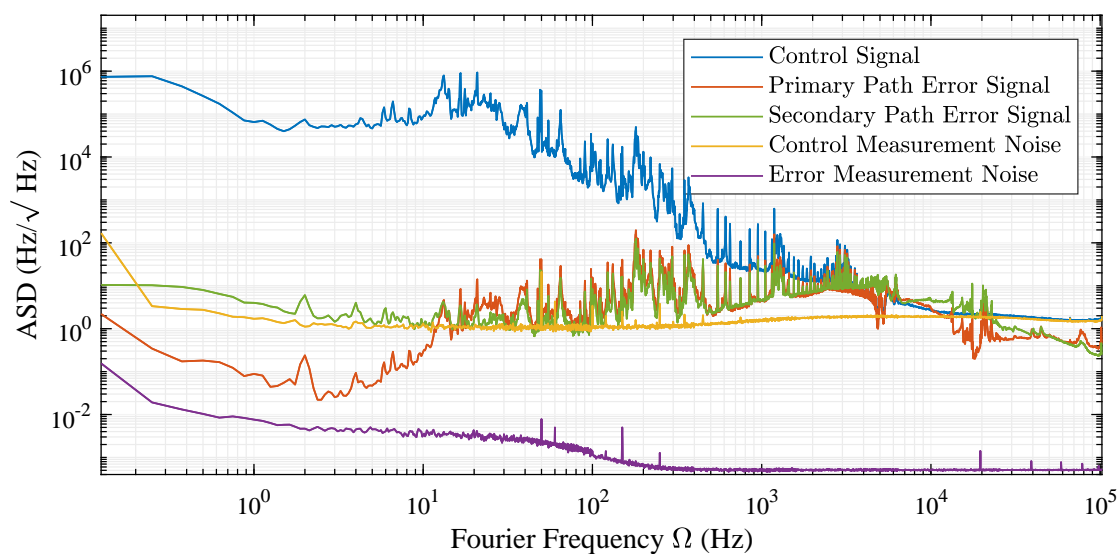


Figure 3.24.: Control and error spectra for length control after compensating for actuator resonances. The control signal is the signal sent to the high voltage amplifier that is then sent to the mirror actuator. One of the error signals is the signal sent to the control electronics and the other one is processed in the same way but measured by a separate photodetector as shown in Figure 3.19. The noise seen at lower frequencies in the control signal is primarily caused by movements of the cavity mirrors, whereas the higher frequency noise is caused by laser frequency noise. The unity gain frequency is where the signals cross. The differences above the unity gain frequency between the primary and secondary error signals is due to the compensation being applied only to the primary path signal. The internal noise of the SR785 measurement system is also shown and limits the measurement of the control signal at high frequencies and the primary path error signal at low frequencies.

contribute to the error spectrum measured with the compensated system. The error spectra from the secondary detector for the systems with and without digital filtering along with the RMS calculated from these spectra are shown in Figure 3.26. This RMS is calculated from the spectral density by numerically integrating the spectrum with respect to the frequency. This integration can be done to only include frequencies from ∞ down to the Fourier frequency, Ω , giving the RMS as a function of frequency. The physical significance of this frequency is that it is the RMS over a duration of $1/\Omega$. Additionally, this method can provide information on what features in the amplitude spectral density contribute the most to the RMS. The RMS of the spectrum for the system without any filtering for compensation is 5.1 kHz. When filtering is applied using the Moku, the RMS of the spectrum is 1.1 kHz. This represents a reduction of more than a factor of four by introducing digital compensation. Both systems are primarily limited by the amount of gain that they are able to provide except at frequencies below 20 Hz.

Though these measurements were conducted using the ALPS IIa RC, the ALPS IIc

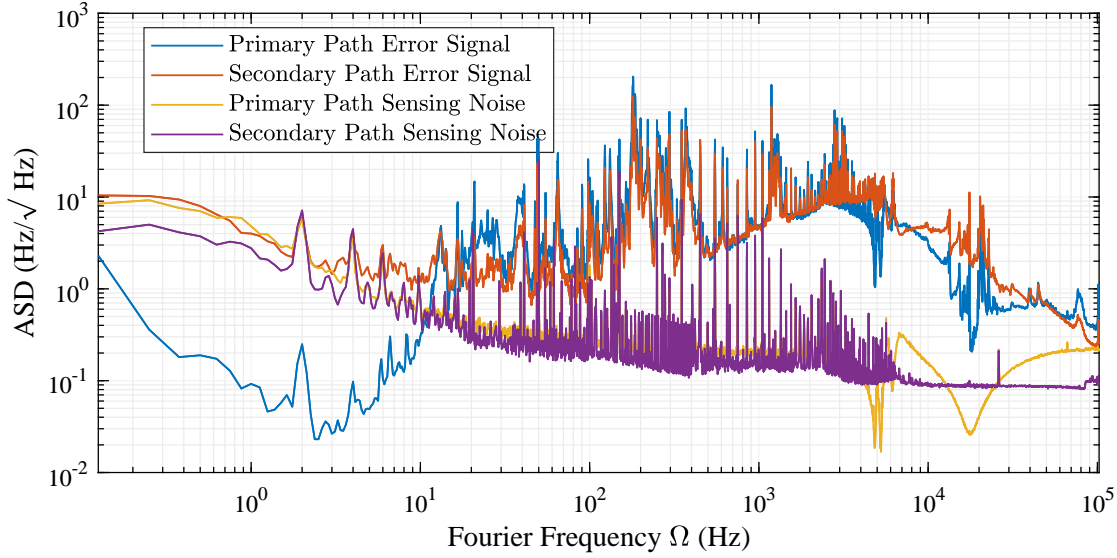


Figure 3.25.: Sensing noise compared to primary and secondary error spectra for compensated length control system. The error spectra are the same as shown in Figure 3.24 and are measured the same way. The primary sensing path noise is the same as shown in Figure 3.23 and is measured the same way. The secondary path sensing noise is the full noise measured by the secondary sensing path with the cavity significantly misaligned so that no light is resonant in the cavity. This should include all optical and electronic sources of noise. This noise has been converted into frequency spectral density by applying the calibration of of the error signal.

scheme intends to actuate on the length of the PC. In order to determine whether either of these systems are able to provide sufficient suppression for use in the ALPS IIc PC, we need to project the performance onto that system. The motion of the ALPS IIc site is similar to that of the ALPS IIa site [58], so the disturbances of the ALPS IIc cavities will be similar to those in ALPS IIa. Therefore, the noise of control systems in ALPS IIa can be projected onto the cavities of ALPS IIc. The first step is to apply the adjustment of the frequency noise of the ALPS IIa cavity to the ALPS IIc cavity in Equation 1.65. This shows the differential frequency noise expected between the ALPS IIc PC and RC if this were the system suppressing that differential noise in the PC. As the light circulating in the cavity is green light as a result of frequency doubling the IR light, any frequency noise for this light has an additional factor of two compared to the IR light that must be removed by dividing the spectrum by that factor of two.

Once the frequency noise of the frequency doubled RL circulating in ALPS IIa RC is projected onto the HPL light circulating in the ALPS IIc PC, we can then determine the power loss in the frequency overlap parameter due to the dynamic frequency noise measured. This is done by using Equation 1.61 where A is the spectrum of the frequency noise projected to be present in the ALPS IIc PC. Applying this equation is the same as calculating the RMS of the frequency noise filtered by the low-pass behavior of the

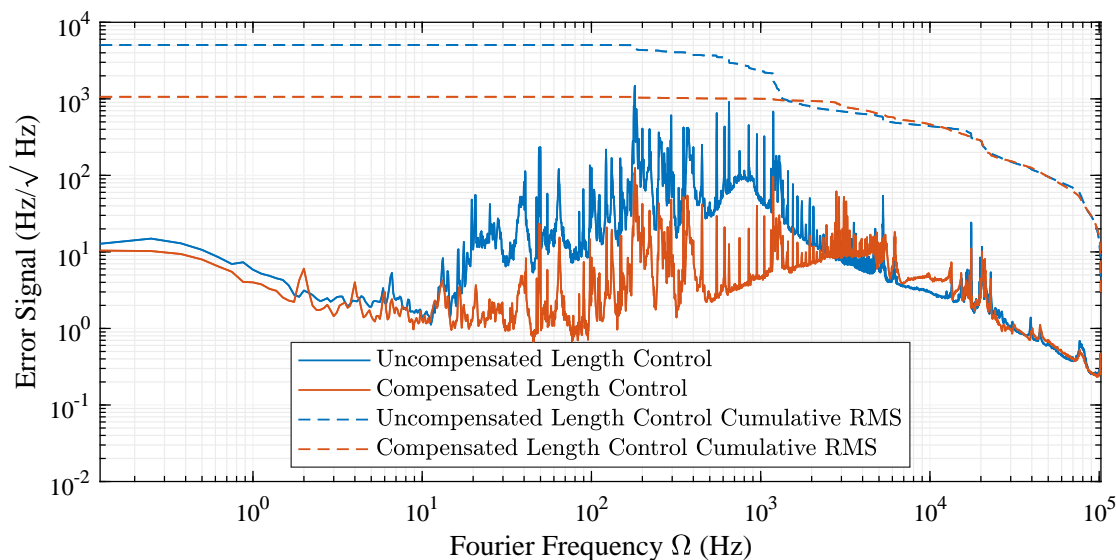


Figure 3.26.: Comparison of error spectra between compensated and uncompensated length control. The uncompensated spectrum is the secondary sensing path spectrum in Figure 3.22. The compensated spectrum is the secondary sensing path spectrum in Figure 3.24. The dashed lines are the cumulative RMS calculated for each spectrum. This RMS totals 5.1 kHz for the uncompensated system and 1.1 kHz for the compensated system.

cavity, so this RMS can be calculated in the same way as in Figure 3.26 by numerically integrating from ∞ to Ω to show the impact of various features in the spectrum on the RMS.

The corner frequency of a cavity is $\Delta f_{peak}/2$, and Δf_{peak} for the ALPS IIc RC is calculated in Section 1.5 to be 30 Hz, making the corner frequency 15 Hz. In addition to applying the low-pass effects of the cavity pole, the frequency conversion from ALPS IIa to ALPS IIc is done, and the spectrum is divided by a further factor of 2 to give us the noise of the infrared light. The results are shown in Figure 3.27. As with Figure 3.26, the blue solid curve is the frequency noise of the uncompensated system and the blue dashed curve is the integrated RMS of that system. The orange curve is the frequency noise of the compensated system, and the orange dashed curve is the integrated RMS of that system.

The solid black line shows the ALPS IIc requirement of 3.0 Hz, as discussed in Section 1.5. The integrated RMS of the uncompensated system is 9.8 Hz, which is several times larger the requirement. The integrated RMS of the compensated system is 1.0 Hz, which exceeds the requirement by more than a factor of 2.

It is clear that the primary driver of the RMS of both systems is the peak at 180 Hz. This could be further improved by the implementation of resonant gain, at the cost of phase lag near the resonance. Since the unity gain frequency of the compensated system is more than an order of magnitude larger, this phase lag due to the resonance

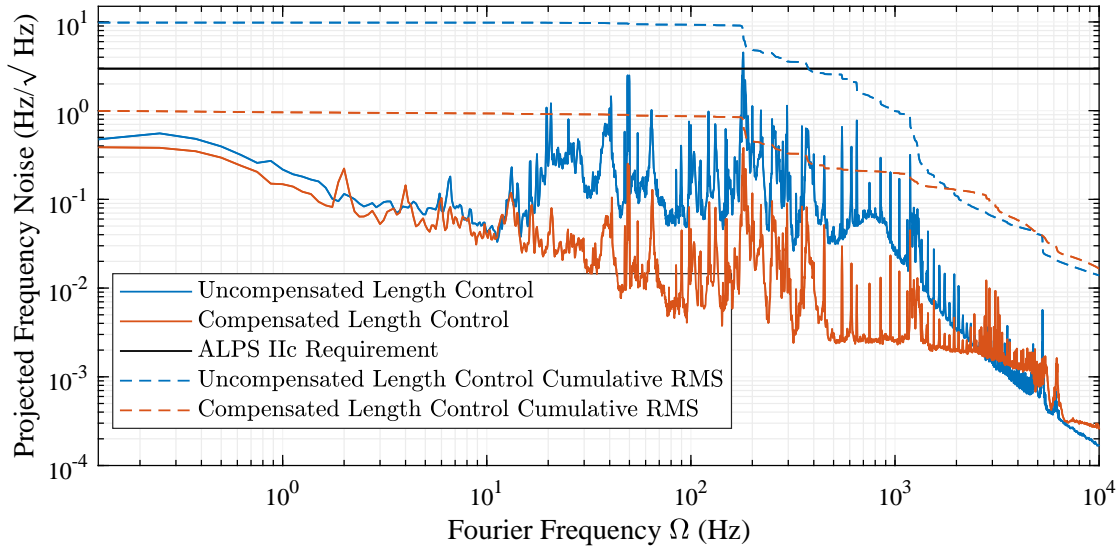


Figure 3.27.: Projection of compensated and uncompensated length control onto the coupling between the two cavities of ALPS IIC. The spectra projected are the two shown in Figure 3.26. The spectra are converted into the expected spectra for IR light by dividing by a factor of two, and then projecting the ALPS IIA RC noise onto the ALPS IIC PC by dividing by the ratio of the two cavity lengths. Finally, Equation 1.61 is applied where A is the spectrum of the frequency noise projected to be present in the ALPS IIC PC which is the same as calculating the RMS of the frequency noise filtered by the low-pass behavior of the cavity. As such, this cumulative RMS is displayed by the dashed lines. Additionally, shown in black is the ALPS IIC requirement of 3.0 Hz. The RMS for the uncompensated length control is 9.8 Hz which does not meet the requirement, but the RMS for the compensated length control is 1.0 Hz which does meet the requirement.

should not contribute significantly to the phase margin of the system. Additionally, this resonant gain is unnecessary for the compensated system as it exceeds the requirements without it, whereas the uncompensated system would not meet the requirements even with additional gain at 180 Hz.

3.5. Mirror Actuator Design

The requirements of the end mirror actuator for ALPS IIC include a large clear aperture on both sides of the mirror while maintaining a high bandwidth of actuation. There were no commercial mirror actuators that provided these requirements, so a custom one was required. As discussed in Section 3.4, the mirror used for the ALPS IIA system has a diameter of 50.8 mm and a mass of 43 g [46], with similar physical dimensions expected for the mirrors in ALPS IIC. The force for the actuation is provided by a custom ring piezo from PI with an outer diameter of 56 mm, an inner diameter of 38 mm, and a thickness of 7 mm. This ring piezo allows a laser to couple light into the cavity through

the center portion of the mirror.

For the first iteration of the mirror, it was planned to additionally have 3 rectangular piezos around the edge of the ring to actuate on the angle while the ring piezo actuates on the position. The concept of the actuator was that the smaller piezos would sit in pockets machined into the mount. The ring piezo would then be placed against those piezos and the mirror would be stacked directly against the ring piezo. The restoring force was provided by a wave washer that would be compressed by a retaining ring. The ring piezo is larger than the mirror, meaning the mount needed to be wide enough to accept the ring piezo. To ensure that the mirror was centered in the mount, the retaining ring also had a pocket machined into the inside that was just big enough for the mirror to fit into it.

The schematic drawing of this stack, as well as the results from using this actuator are found in Section 3.4 and will be referred to as the 3-axis actuator, as it was intended for motion in three axes. Unfortunately, the small piezos included to actuate on the angle did not have sufficient actuation range to produce useful angular actuation, so that functionality was not continued in the second actuator design.

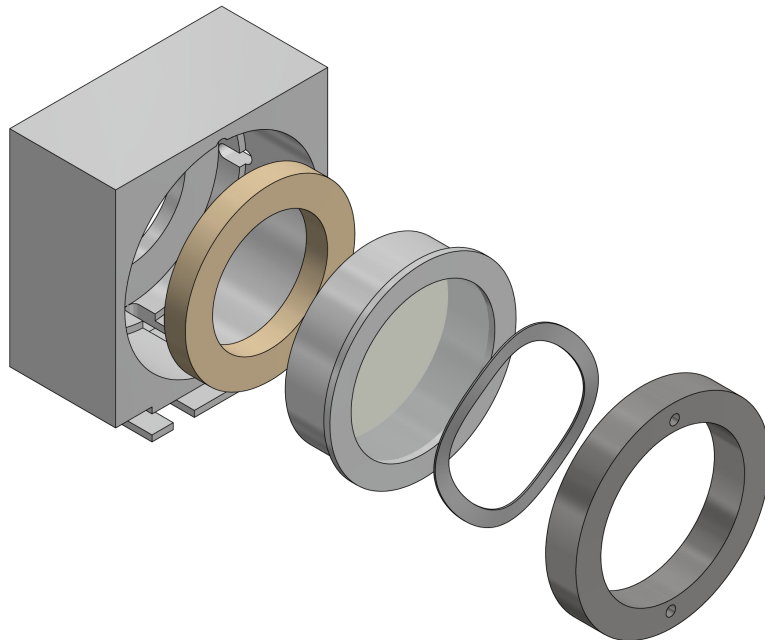


Figure 3.28.: A schematic drawing of the components of the mirror actuator with a mirror holder. It includes from left to right, the mirror mount, a large ring piezo, the mirror holder assembly, a wave washer to provide restoring force, and the retaining ring to compress the wave washer.

A second actuator was designed to test whether force being exerted directly onto the mirror was causing deformations or other effects and generally to minimize the amount

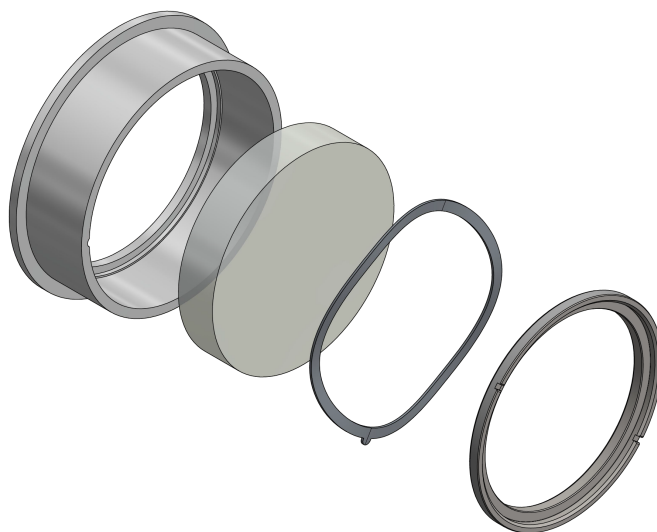


Figure 3.29.: A schematic drawing of the components of the mirror holder assembly. It includes from left to right, the mirror holder, the cavity end mirror, a wave washer to avoid wavefront distortion in the mirror, and the retaining ring to hold the assembly in place.

of force directly on the mirror in order to protect it from damage. For this mount, it was important that the mirror was insulated from the actuation force. The actuator is shown in Figure 3.28, which includes a mirror holder assembly shown in Figure 3.29. The piezo element in this case now rests directly against the mount, and pushes on the mirror holder assembly. A retaining ring still provides restoring force, but against the mirror holder rather than the mirror itself. Finally, a retaining ring provides the initial compression. The mirror holder assembly features a cup for the mirror, the cavity mirror itself, a wave washer, and a retaining ring. The key feature is the mirror holder that insulates the mirror itself from the direct pressure of the piezo and the restoring wave washer. There is another wave washer in the mirror holder assembly, but rather than providing the restoring force, it transfers the force of the mirror holder retaining in a more controlled and gentle manner than if this retaining ring were pressing directly against the mirror to prevent distortions of the mirror surface. Additionally, as the mirror is insulated from the direct forces of the piezo and the restoring wave washer, the force applied to the mirror is a constant one and does not depend on the position of the actuator. This actuator will be referred to as the mirror holder actuator.

As the mirror holder is heavier than just a mirror, the system will not be able to achieve the same level of performance. The mass of the mirror holder assembly is 74.8 g, compared to the 43 g of the mirror itself. Figure 3.30 shows the first resonances of each actuator. We see that the first resonance of the 3-Axis actuator was 4.88 kHz, while the first resonance of the mirror holder actuator is 3.0 kHz. The expectation of a simplified mass on a spring is given by

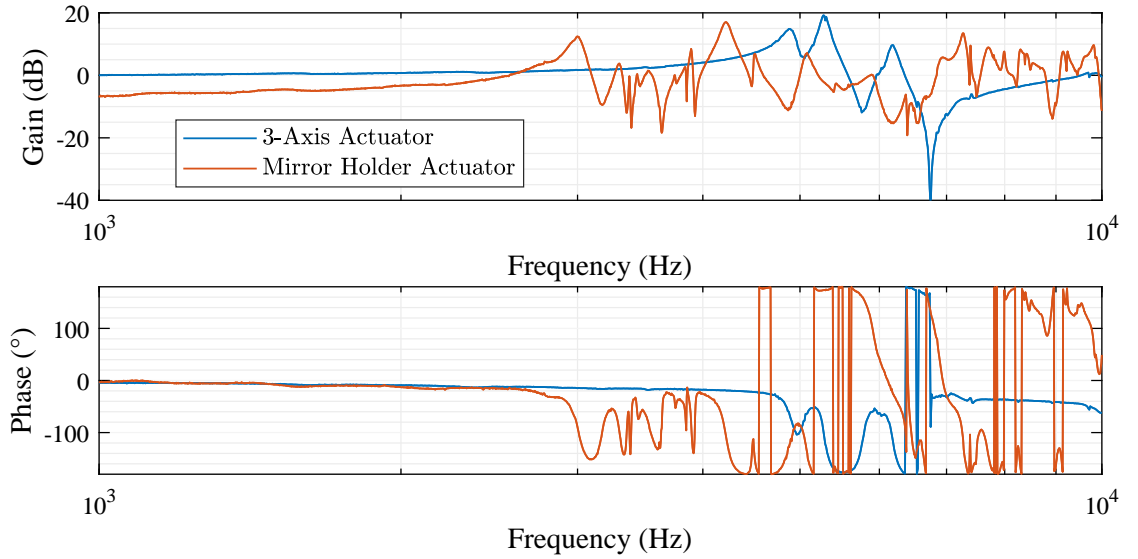


Figure 3.30.: Transfer function of 3-axis and mirror holder actuators. The first resonance of the 3-axis actuator is 4.88 kHz, while the first resonance of the mirror holder actuator is 3 kHz. Both transfer functions were measured by engaging the control loop discussed in Section 3.3 and comparing a swept sine sent to the high voltage amplifier connected to the mirror actuator to the control signal of the frequency control loop at those frequencies. The measurements were made with an averaging factor of 100 and an input of between 0.1 mV and 50 mV peak-to-peak.

$$\omega = \sqrt{\frac{k}{m}}, \quad (3.5)$$

where k is the spring constant, and m is the mass. From this model, one would expect a change of only the square root of the mass ratio, which would lead to a first resonance of the mirror holder of ≈ 3.7 kHz. The second resonance change is much closer to the expectation, with the second resonance of the 3-Axis mount being located at 5.3 kHz and the second resonance of the mirror holder mount located closer to the expected ≈ 4.0 kHz at 4.2 kHz, which is slightly higher. Since the first resonance has shifted much more than the second, it is unlikely that both of these shifts were solely due to the extra mass.

As we examined in Section 3.4 with the 3-Axis actuator, this resonance limits the unity gain frequency of length control. The unity gain frequency of the 3-Axis actuator with the resonance at 4.88 kHz was 3.9 kHz. We should expect a similar relationship between the achievable unity gain frequency and the location of the first resonance with the mirror holder actuator. This unity gain frequency change can be accomplished with new filtering coefficients for the actuator resonances and a reduction of proportional gain. A factor of 2 decrease in proportional gain should lead to a factor of 2 increase in the suppressed noise of the system. The projected RMS noise of the compensated length control system in the previous section is 1.0 Hz, so the mirror holder actuator should

be able to achieve 2.0 Hz RMS projected noise. More investigation using this mirror actuator in a length control system would provide more concrete results. The benefit of this actuator is that the mirror will not experience any differences in pressure due to the actuation, which will limit any deformation of the surface and any other effects due to the forces involved, as well as limiting the potential for any damage to the mirror from these large forces.

3.6. Conclusions

In this chapter, the existing, analog systems in the ALPS IIa RC are characterized. These systems all maintain resonance between the cavity and the input laser, either by actuating on the laser frequency, or the length of the cavity. The frequency control systems are for the IR light from the HPL, and for the green light from the frequency-doubled RL. The length control system uses a custom designed actuator to ensure that the green light from the RL is resonant in the cavity.

Direct comparison between the frequency control systems and the ALPS IIc requirements is not possible as the control architecture will feature higher bandwidth loops using additional actuators for further suppression [43]. Loops using electro-optic modulators have demonstrated significant additional suppression compared to those using only the piezo-driven frequency control systems [59]. The understanding of these loops is most important in understanding their limitations and the noise present. The performance of these loops can be an excellent point of comparison with digital frequency control systems.

In addition to the frequency control loops, the length control loop is important for the frequency overlap between the two cavities in the ALPS IIc experiment. In this case, the actuator and control system implemented in ALPS IIa is very similar to the actuator and control system that will be used for ALPS IIc and the noise suppression possible with this system can be projected onto the ALPS IIc system. This length control system should meet the requirements discussed in Section 1.5, with either of the two presented actuator concepts.

With a baseline established, the next chapter will discuss the use of digital systems for frequency control of the RL to match the resonance of the cavity and will compare those results with those presented in Section 3.3.

4. Digital Frequency Control

With the cavities and current control systems of ALPS IIa characterized for the mostly analog control systems, the difference in performance of the cavities with a digital control system can also be investigated. In this chapter, we will discuss the digital architecture used for the control systems, as well as a digital system replacing the servo and a digital system replacing most of the sensing system as well as the servo.

4.1. Digital Architecture

Implementation of a digital system requires hardware, firmware, and software. The hardware is necessary to digitize signals, execute any calculations necessary to implement the desired servo, and generate a signal afterwards. Firmware instructs the hardware what actions to take, including any algorithms so that the hardware can complete the calculations as quickly as possible. Finally, the software allows the user to interface with the system to define certain parameters in the firmware to change the behavior of the hardware.

The requirements for the hardware include analog to digital converters to read-in data, high input and output rates, and a digital to analog converter to output data. These requirements are all fulfilled by a field programmable gate array (FPGA), which are very well suited to digital signal processing. The Moku Lab mentioned in Section 3.4 is a commercial FPGA with a number of user-friendly filtering options. However, with commercial devices, it is often difficult to address any problems that are unique to the ALPS experiment and it can often be difficult to determine exactly what the device is doing without collaboration with the developers. As such, all digital control systems used in this thesis are implemented on an FPGA system with software and firmware developed by Deutsches Elektronen-Synchrotron (DESY) personnel.

Standalone FPGAs are available commercially, and often excellent for some applications. However, with the possibility of needing several FPGAs to implement full control of the ALPS II experiment that each would need to communicate with each other in real time at high speed, a solution easily providing this communication was needed. Several FPGA-based control systems at DESY use the MicroTCA (mTCA) standard, which features a number of communication options between cards in the same crate as well as cards in other crates [60]. This standard and the FPGA systems available for it is well-understood by the firmware development group at DESY. As a modular, open system architecture, it allows for many different customization and future replacement options without the need for expensive, custom hardware development. As such, this architecture was chosen for digital control systems.

The primary functional component of the mTCA architecture is the advanced mezzanine card (AMC), with the other components providing housing, communication, power, control, etc. of the AMCs. The AMC selected for this control system is the Struck SIS8300 digitizer, which has high speed ADCs and DACs, and an optional FPGA. In addition to the FPGA, ADC, and DACs in the AMC, the MTCA.4 version of the standard allows for each AMC to have a rear transition module (RTM) that interfaces only with it [61]. The function of these RTMs is to provide enhanced functionality to the AMCs, such as signal conditioning, analog demodulation, and high voltage supply for driving piezos. For this system, we use the Struck SIS8900 RTM to provide a physical interface for LEMO cables carrying the signals to the FPGA.

The firmware for the controllers using this FPGA largely re-uses modules developed for other FPGA-based control systems at DESY. These modules are combined in ways that are unique to the ALPS II experiment. Despite the many advantages of this re-use, not all functions required were provided by existing modules, and as such there are some new modules developed specifically for use with ALPS II. Any development necessary to combine existing modules as well as programming new ones for the firmware used was done by Lukasz Butkowski of the Maschine Strahlkontrollen department at DESY.

This firmware allows for the change of some register values to change the behavior of the controller. For example, the input gain and controller parameters can be changed by writing new values to the relevant registers. The controller architecture is almost exclusively a 6x6 state space model. Both continuous and discrete time state space models are discussed in Appendix A. As mentioned in Chapter 2 and Appendix A, this corresponds to a maximum of 6 poles and zeros or a sixth-order transfer function to set the frequency-dependent behavior.

The software for interfacing with the firmware in order to turn the control on or off, adjust the proportional gain, upload new coefficients to the system, or any other actions that a user might wish to do was done in MATLAB App Designer. This allows interaction simply by changing the values in user-editable fields, clicking on digital switches, and loading external files containing controller parameters. This also allows input and output data to be read from the FPGA and displayed on the screen, giving the user some insight as to the current behavior of the control system. This software was run on a computer on an AMC that was housed in the same mTCA system as the FPGA.

4.2. Frequency Control with a Digital Servo

The first test of a digital control system is simply replacing the analog servo with a digital system. A schematic for this system is shown in Figure 4.1. The only difference between this and the green frequency control system in Figure 3.9 is that the servo is now an FPGA in a mTCA system. Not pictured in this schematic is an analog amplifier necessary to expand the dynamic range of the control signal. The DAC can only output ± 1 V, which is not sufficient to drive the laser frequency piezo enough to compensate for the cavity disturbances. The amplifier used is a SR560 low noise voltage amplifier which can provide ± 5 V output. Therefore, the control signal was amplified by a factor of 5

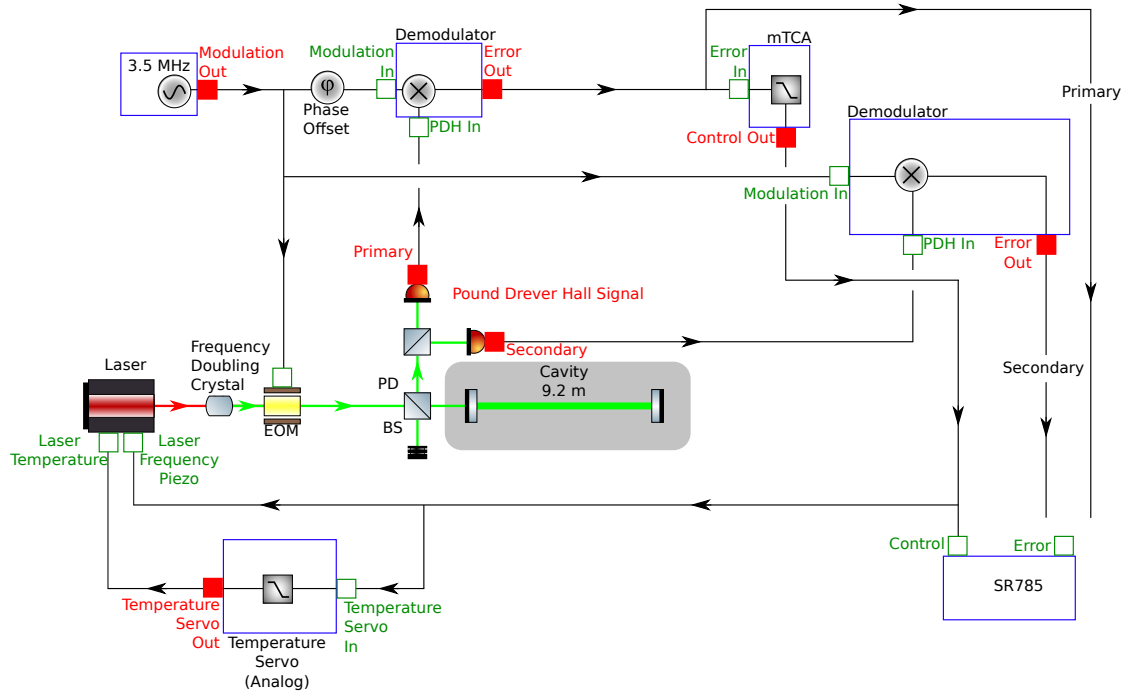


Figure 4.1.: Schematic of a feedback control system with a digital servo. This setup is otherwise identical to the feedback control system in Figure 3.9.

to generate sufficient output to control the cavity. This amplifier is used for all systems where a digital system is generating the control signal. Additionally, though the control signal is generated by a digital servo, the temperature control signal is still generated by an analog temperature control servo.

The open-loop transfer function of this system compared to the open-loop transfer function of the analog green frequency control system is shown in Figure 4.2. The slope of the transfer function for the digital servo is slightly shallower than the slope of the analog servo, netting less phase lag. However, these differences are not very large and demonstrate a very similar performance of both systems. The additional phase lag from the processing time of the digital servo does not cause a large loss of performance at the frequencies used for this control system.

The control and both error spectra, as well as measurement limits are shown in Figure 4.3. The blue control spectrum is very similar to that of the analog frequency control system shown in Figure 3.11, as the plant in both control systems is the same. In this case, though, both the primary and secondary error sensing paths are well above the measurement limits shown in purple, which does not contribute much to the measurement of the error spectra. Both sensing paths are very similar, which is due in large part to the source of the sensing noise for this system.

The sensing noise at different points in the system from different sources is shown in Figure 4.4. We see the electronic noise from the demodulator and photodetector exceeds

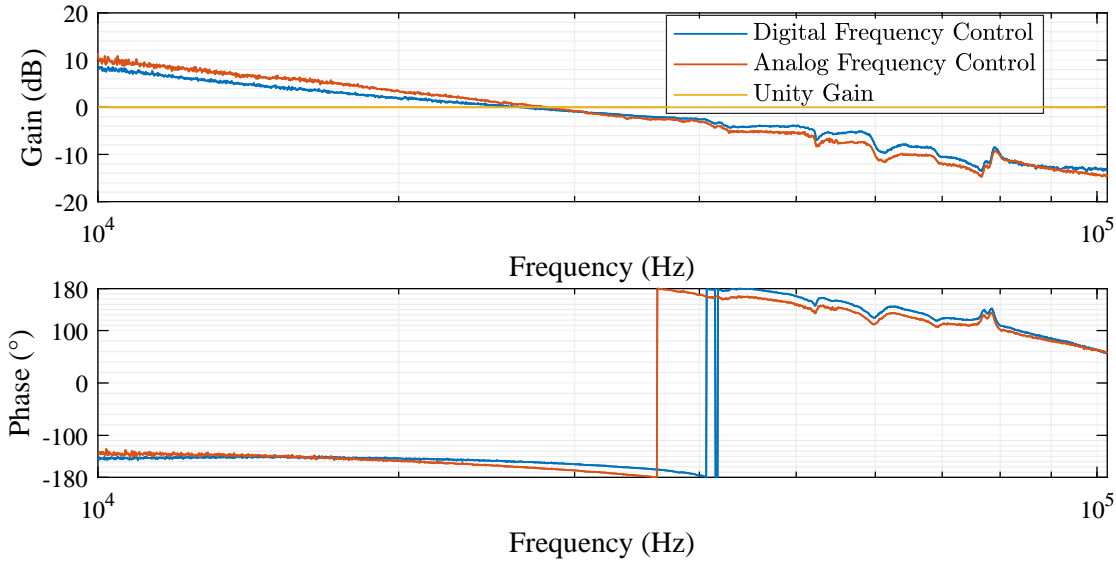


Figure 4.2.: Open-loop transfer function of green frequency control with analog and digital servos. The unity gain frequency of the analog frequency control system is 28 kHz with a phase margin of 17 $^\circ$ compared to the digital servo system that has a unity gain frequency of 27 kHz and a phase margin of 29 $^\circ$. Both transfer functions were measured by injecting a swept sine on the control signal and comparing the control signal with the swept sine to the control signal right before the swept sine was injected. The measurements were made with an averaging factor of 100 and an input of between 0.1 mV and 5 mV peak-to-peak.

the noise from the FPGA ADC at frequencies over 100 Hz, with the ADC having an approximately $2 \text{ Hz}/\sqrt{\text{Hz}} \cdot (1 \sqrt{\text{Hz}}/\sqrt{f})$ slope across the whole frequency range. This indicates that the ADC will only contribute significant noise at lower frequencies, since at 1 kHz, the noise contribution from the ADC is an order of magnitude lower than the noise contribution from the analog sensing electronics. However, we see that the full system electronic noise is much larger than the demodulator noise and the ADC noise. This excess is seen across the full frequency spectrum recorded except extremely low frequencies (< 1 Hz) and very high frequencies (> 20 kHz) and is possibly due to the offset box discussed in Section 3.3 that was also a part of this setup. This electronic noise is the dominant contributor to the sensing noise of the system, as the purple curve showing the full sensing noise including optical sources is identical to the electronic noise at all frequencies except a small difference at frequencies below 5 Hz.

This electronic noise is added after the error spectrum in the primary sensing path is measured. This measurement was made immediately after the demodulator and before other electronics as their contribution to sensing noise was not considered until much later. As such, that error point noise is not present on the measured spectrum. So when the loop suppresses the electronic noise, imprinting it onto the cavity, this imprinted noise is measured despite it being the in-loop sensing path. If the digital error spectrum

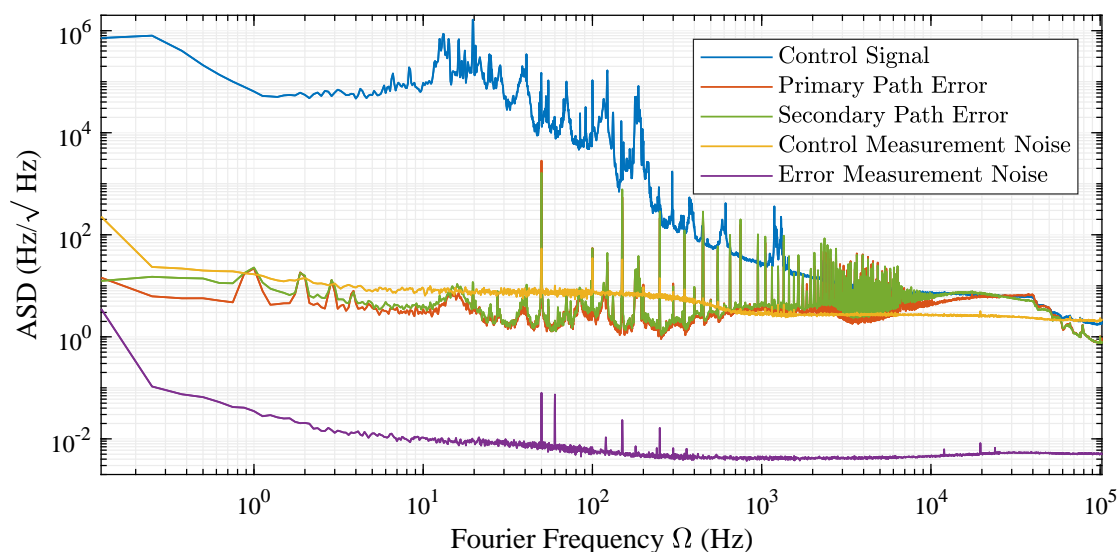


Figure 4.3.: Control and error signal with FPGA as digital servo. The control signal is the signal sent to the laser piezo. One of the error signals is the signal sent to the control electronics and the other one is processed in the same way but measured by a separate photodetector as shown in Figure 4.1. The noise seen at lower frequencies in the control signal is primarily caused by movements of the cavity mirrors, whereas the higher frequency noise is caused by laser frequency noise. The unity gain frequency is where the signals cross. The rise near that frequency is known as a servo bump and is due to oscillations in the control loop. The internal noise of the SR785 measurement system is also shown and limits the measurement of the control signal at high frequencies but does not limit the measurement of the error signal.

were measured, it would be much lower as all of the electronic noise would be suppressed by the gain of the control system. Unfortunately, the FPGA is not able to store long data strings and continuous read-out of the digital data is a significant technical challenge.

One final source of error is the quantization error discussed in Section 2.5. Calculated according to Equation 2.37, using an input range of ± 1 V, a 16-bit ADC, and an effective sample rate of 3.5 MHz, the quantization noise should be at a level of $6.7 \text{ nV}/\sqrt{\text{Hz}}$ across the full spectrum. When the conversion between voltage and frequency for this setup is applied, the frequency noise is $3.7 \text{ mHz}/\sqrt{\text{Hz}}$, which is well below all of the other noise sources.

Figure 4.5 shows a comparison between the error spectra for the primary and secondary path, as well as the sensing noise for each path. The secondary path is entirely analog and has no offset box between the demodulator and the measurement system, and therefore does not have any extra noise from either the offset box or the FPGA system. The main contributor to both the primary and secondary error spectrum for the majority of frequencies is the sensing noise in the primary sensing path. Some noise peaks are above the primary path sensing noise, but the majority of the spectra are nearly identical.

The main region where the spectra are larger than the sensing noise is close to and

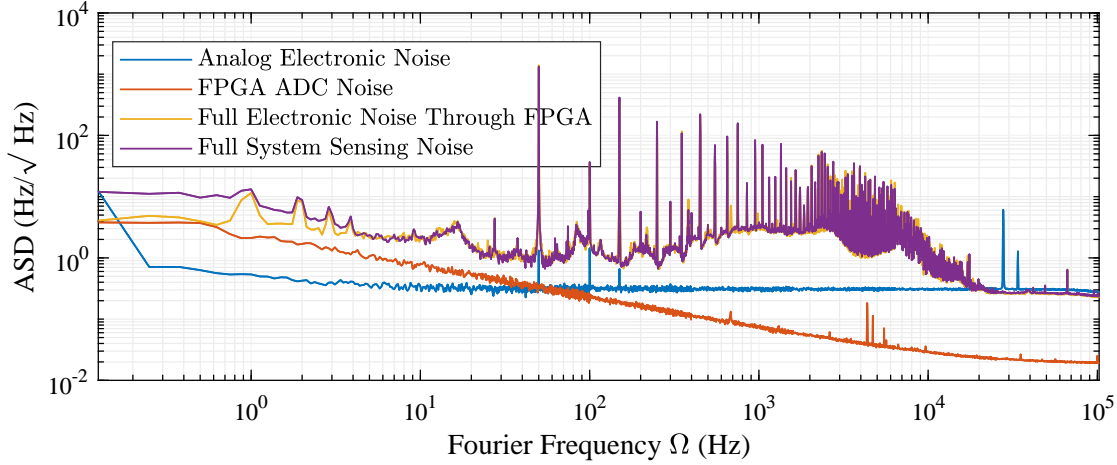


Figure 4.4.: Sensing noise of primary error signal path with FPGA as digital servo. The blue curve is the same electronic noise measured in Figure 3.13 with the photodetector and demodulator. The orange curve is measured by terminating the input to the FPGA system and measuring the output with a large amount of gain in the digital system. This is so that the amplified FPGA noise of the ADC is much larger than the DAC noise so that both are not measured. The yellow curve is with the system connected but no light in the system. The FPGA gain is again large to minimize the effects of the DAC. The purple curve is the same electronic setup as the yellow curve, but with light in the system and the cavity significantly misaligned so there is no resonance. Just as with the yellow and orange curves the FPGA gain is again large to minimize the effects of the DAC. The purple curve represents the full electronic and optical sensing noise of the system. This noise has been converted into frequency spectral density by applying the calibration of of the error signal.

above the unity gain frequency. Above 10 kHz, the primary path sensing noise falls off dramatically, and the error spectra are both suppressed by a much smaller amount than at lower frequencies as this is where the transfer function gain is close to 1. Additionally, the servo bump adds additional noise in the error spectra that drives it well above the sensing noise. At low frequencies, the secondary path error spectrum is not exactly as expected if all of the noise sources were perfectly uncorrelated. This is the likely same effect as is found in the green analog frequency control in Section 3.3.

Figure 4.6 shows these error spectra of the two systems through the secondary sensing path as well as the RMS of this error signal starting at 10 kHz. The most notable differences are the higher noise floor and peaks due to the sensing noise of the digital servo system, indicating that the offset box is adding significantly more noise at the input of the digital servo compared to the analog servo. Both the noise floor and the peaks are approximately a factor of five larger between 100 Hz and 10 000 Hz. Though the offset box is believed to be the cause of this noise for both systems, it contributes much more to this digital servo. One potential cause of this is the sensitivity of the noise on the electrical connections of the system, and they are significantly different when

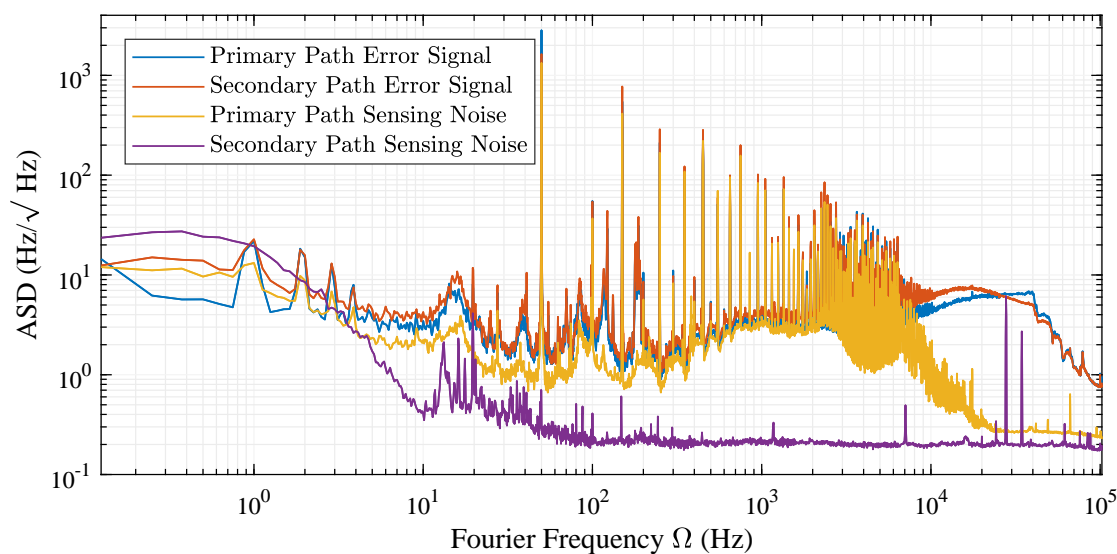


Figure 4.5.: Primary and secondary error spectra compared with sensing noise. The primary and secondary error spectra are the same as shown in Figure 4.3 and the primary sensing path noise is the same as shown in Figure 4.4. The secondary sensing path is the noise measured by the secondary sensing path with light in the system but the cavity misaligned such that light cannot be resonant with the cavity. This should represent the full electrical and optical sensing noise for the secondary sensing path. This noise has been converted into frequency spectral density by applying the calibration of of the error signal.

using a digital servo compared to an analog servo. The shape of the servo bumps are also significantly different. The RMS of the error signal with the fully analog system is 1100 Hz of suppressed frequency noise with the primary driver of this being the servo bump. The RMS of the error signal with the digital servo is 1900 Hz. The vast majority of the contribution to the RMS of the analog system is from the servo bump, while the digital servo system has much more contribution from the noise, despite attempts to keep the servo bump a consistent size between measurements. This result indicates that there is improvement to be made in optimizing the proportional gain level for each system. For this reason, the RMS shown is only calculated starting at 10 kHz to reduce the effect of the servo bump. The RMS for the analog system starting at this frequency is 310 Hz, which further underscores that the servo bump is the dominant contributor. The main contributors to the RMS other than the servo bump are the noise peaks at 50 Hz and its harmonics. The RMS for the digital servo without the servo bump is 1500 Hz, which shows that the total RMS is mostly driven by noise sources below 10 kHz. Just as with the analog system, these are mostly 50 Hz noise peaks and harmonics, and the approximate factor of five difference between the two spectra shows up in this RMS calculation. Reducing the sensing noise would provide a performance increase and contribute to closing the performance gap between the two systems. Even

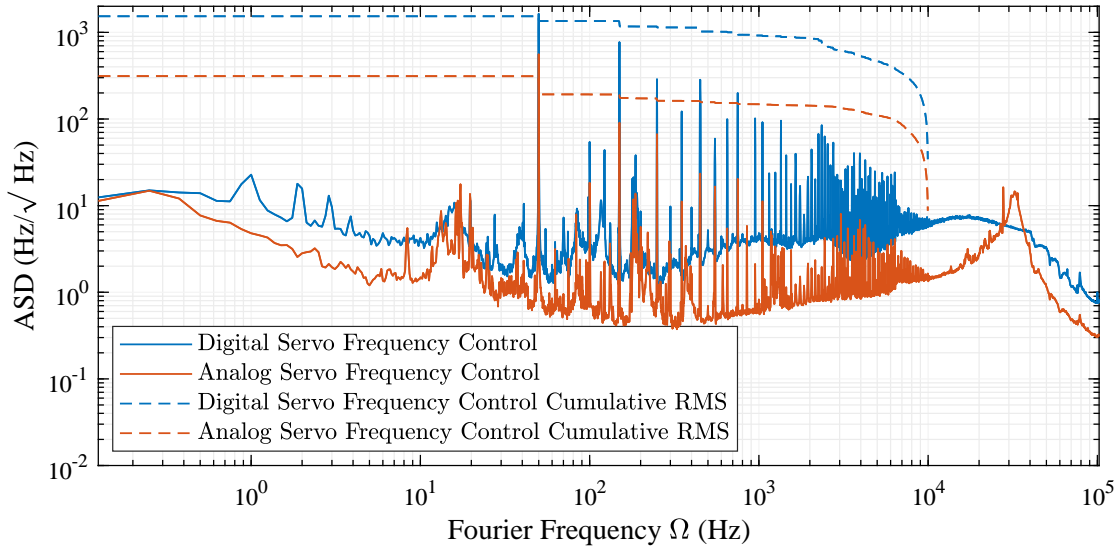


Figure 4.6.: Error spectra of secondary sensing path comparing analog servo to digital servo performance. The digital servo spectrum is the secondary sensing path spectrum shown in Figure 4.3 and the analog servo spectrum is the secondary sensing path spectrum shown in Figure 3.11. Additionally shown are the calculated RMS of each curve without including the servo bump, which is very sensitive to the exact phase margin of the system. The RMS of the system with a digital servo is 1500 Hz, which is primarily driven by large peaks at 50 Hz and harmonics. The RMS of the system with a analog servo is 310 Hz, also driven mostly by the noise peak at 50 Hz.

without that improvement, the two systems have similar performance.

4.3. Fully Digital Frequency Control System

It is also possible to have most of the sensing system be digital. Given the electronic sensing noise seen with the hybrid system using analog demodulation and digital servo, doing this may provide a significant performance increase. In this case, the modulation generation, demodulation, and servo can all be provided by a digital system. A schematic of this setup is shown in Figure 4.7. In this setup, the modulation is output to both the EOM and to an analog demodulation system to be the secondary sensing path. The digital system then reads in the raw photodetector signal and performs the demodulation digitally, comparing it to the digital modulation to generate the demodulated error signal. This digitally-demodulated signal then goes into the digital servo to generate the control signal. As with the analog/digital hybrid system, extracting the in-loop signal being used by the digital system is a technical challenge that was beyond the scope of the work presented here. It could potentially be converted into an analog signal and measured by the SR785 the same way that the other signals are, but the FPGA only has two DACs, so another output card would be necessary to record the in-loop error signal.

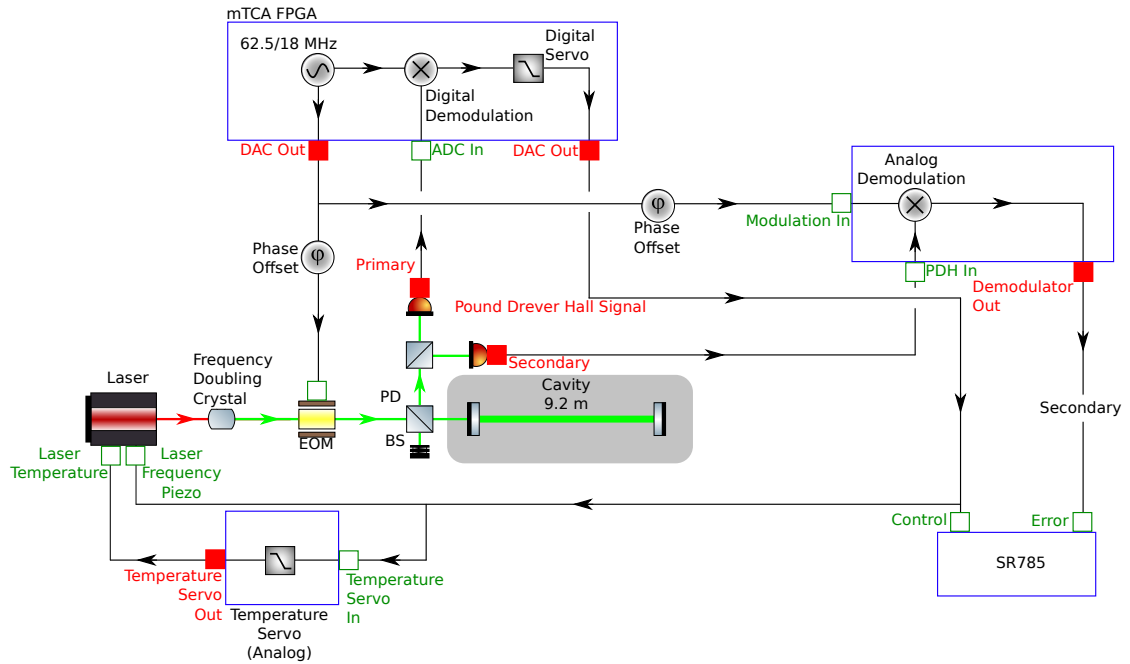


Figure 4.7.: Schematic of a fully digital feedback control system. In this system, modulation generation, demodulation, and the servo are all digital in the same FPGA. There is a separate, analog demodulation system for the secondary error signal path. The temperature servo is analog.

Similarly, the temperature servo must be analog because there is no additional DAC to generate the temperature signal digitally. Finally, just as with the system in Figure 4.1, an SR560 amplifier was used to generate the dynamic range necessary to compensate for cavity disturbances.

Figure 4.8 shows the open-loop transfer functions of the analog control and the digital control systems. The gain slopes of both systems are similar, yet the digital system has less phase lag at higher frequencies than the analog system. The changes are not significant enough to result in a large difference in performance. The unity gain frequency, which was determined based on the size of the servo bump at different proportional gain settings, of both systems is very similar with the fully digital system having a unity gain frequency of 30 kHz compared to the analog system's unity gain frequency of 28 kHz. This is despite the digital system having a phase margin of 28° versus 17° for the analog system.

Figure 4.9 shows the control and error spectra for the secondary sensing path, as well as the measurement limits for the control spectrum. The error spectrum measurement limits are well below the error spectrum, as they are similar to the previously-shown measurement limits, and do not contribute to the measured spectrum. Therefore, they have been omitted from this plot. Additionally, as discussed previously, the primary sensing path is entirely contained within the digital system and there is no ability to

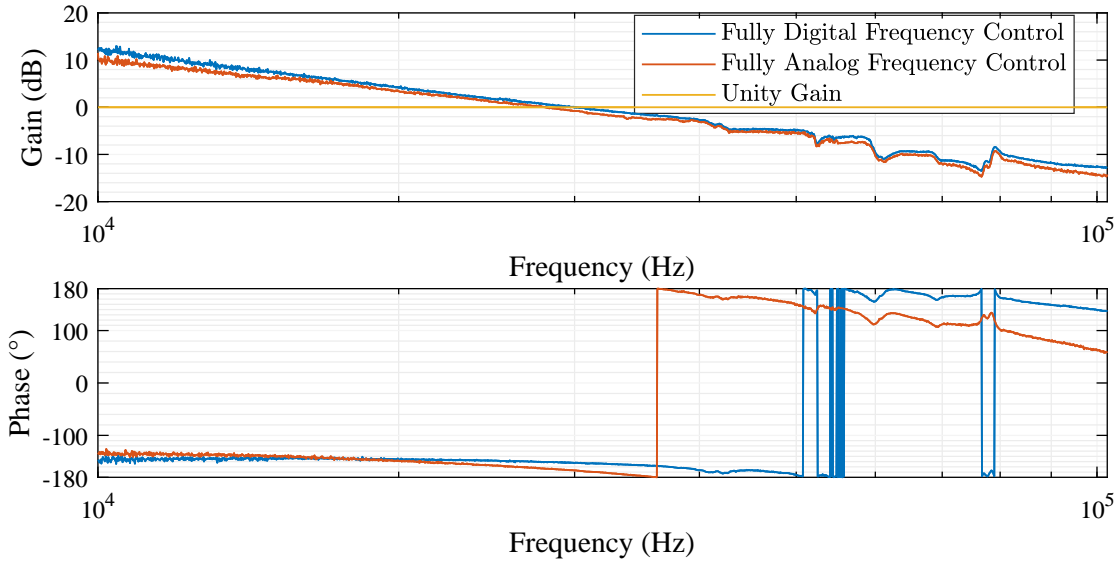


Figure 4.8.: Open-loop transfer function of green frequency control with fully digital control compared to fully analog control. The unity gain frequency of the fully analog frequency control system is 28 kHz with a phase margin of 17 $^\circ$ compared to the fully digital system that has a unity gain frequency of 30 kHz and a phase margin of 28 $^\circ$. Both transfer functions were measured by injecting a swept sine on the control signal and comparing the control signal with the swept sine to the control signal right before the swept sine was injected. The measurements were made with an averaging factor of 100 and an input of between 0.1 mV and 5 mV peak-to-peak.

perform an analog measurement of that path. Just as with the hybrid system measurements in Figure 4.3, the control spectrum is very similar to the analog frequency control measurements in Figure 3.11, because the plant for all three systems is the same.

Figure 4.10 shows the noise of the primary sensing system from different sources. The blue curve is the sensing noise of the FPGA ADC. Unlike in Figure 4.4 with the $2 \text{ Hz}/\sqrt{\text{Hz}} \cdot (1 \sqrt{\text{Hz}}/\sqrt{f})$ slope in the ADC noise, the ADC noise for this system is flat across the spectrum. This is because this curve is the ADC noise around the demodulation frequency of 3.5 MHz rather than starting at DC with the hybrid system. This $1/f$ shape does not continue indefinitely and eventually reaches a constant noise across the rest of the spectrum. There is additional noise when the photodetector is plugged in that is flat across the spectrum. This spectrum is also seen at a lower level for the analog demodulators in Section 3.3. The final part is the low-frequency noise from the scattered light which was also seen in the analog system. This yellow curve shows the full sensing noise for the primary sensing path.

The error spectrum detected by the secondary sensing path compared with the sensing noise seen in those paths is shown in Figure 4.11. The electronic noise floor in the primary sensing path is apparent as a limit of the secondary path error spectrum, though not all of the noise of the cavity is suppressed to below the noise level. However, as with the

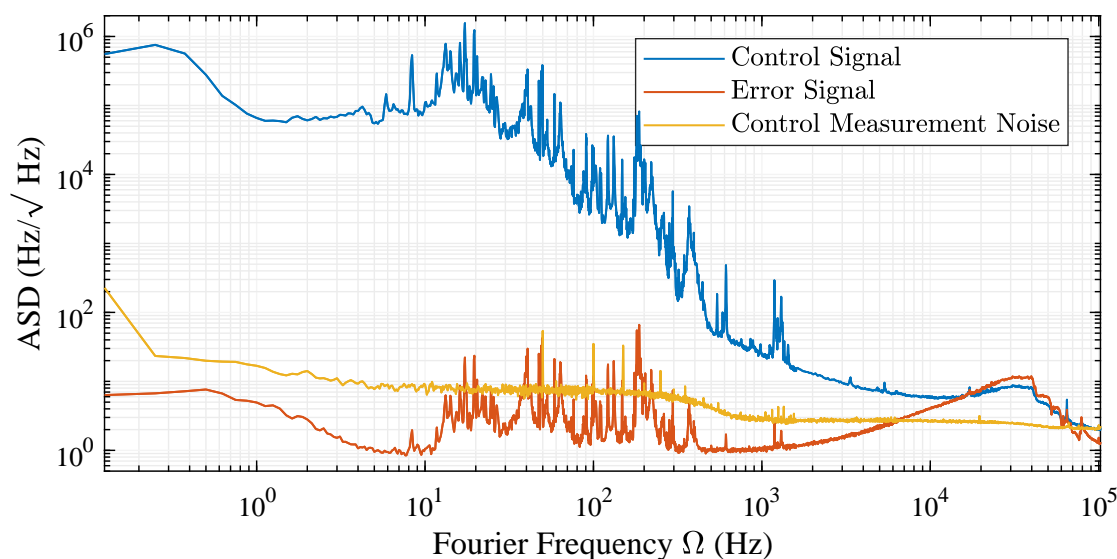


Figure 4.9.: Control and error signal with FPGA as full control system. The control signal is the signal sent to the laser piezo. The error signal used by the control loop is not pictured and only the error signal measured by the analog, secondary sensing path shown in Figure 4.7 is shown. The noise seen at lower frequencies in the control signal is primarily caused by movements of the cavity mirrors, whereas the higher frequency noise is caused by laser frequency noise. The unity gain frequency is where the signals cross. The rise near that frequency is known as a servo bump and is due to oscillations in the control loop. The internal noise of the SR785 measurement system for the control signal is also shown and limits the measurement of the control signal at high frequencies.

systems before, the low-frequency noise is lower than what would be expected from the sensing noise measurements if the sensing noise were uncorrelated.

Figure 4.12 shows the error signal spectra and RMS starting at 10 kHz from the secondary sensing path for the fully analog and fully digital system. The electronic noise floor is approximately a factor of two higher for the fully digital system as seen in the lowest measured noise between 10 Hz and 1 kHz. The servo bumps of the two systems are different as well, with the analog system being narrower and higher and the digital system being wider but lower. Finally, the fully digital system does not have large peaks at 50 Hz and its harmonics. Though the two systems are both using the same mains input, the error signal of the digital system is demodulated after it is digitized and is therefore never subject to this noise as it is not being transported through the control system as a voltage. Though there is some contribution through the DAC and the amplifier, these are much smaller as they are suppressed by the loop gain. The overall noise floor and lack of significant sensing noise peaks from the 50 Hz harmonics represent significant improvements over the hybrid system. The net RMS of the fully analog system is the same as before at 1100 Hz while the fully digital system

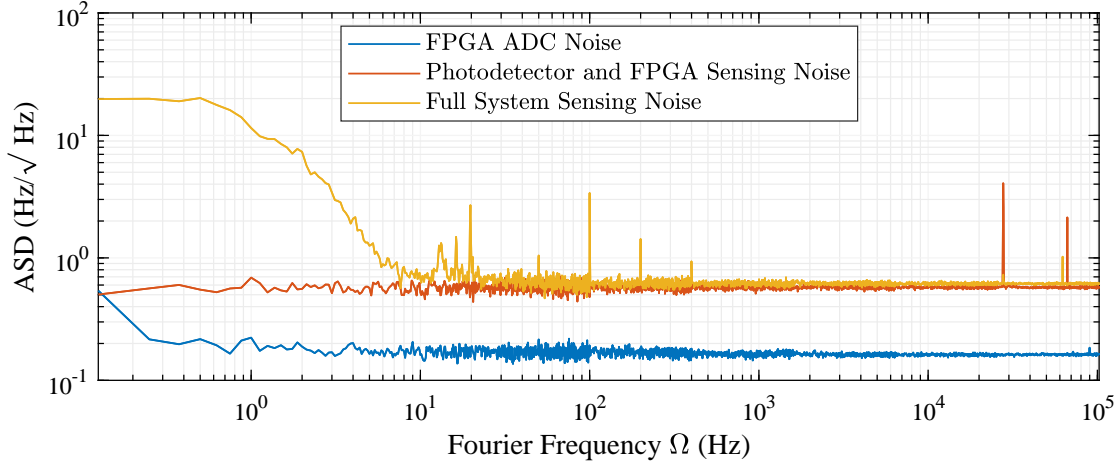


Figure 4.10.: Sensing noise of primary error signal path with FPGA as full control system. The FPGA ADC noise is measured by terminating the input to the FPGA system and measuring the output with a large amount of gain in the digital system. This is so that the amplified FPGA noise of the ADC is much larger than the DAC noise so that both are not measured. The photodetector and FPGA noise is measured by plugging the photodetector into the input of the FPGA and measuring the output again with a large amount of gain. This should represent the full electronic noise of the system. Finally, the full system sensing noise is measured with the same setup as the orange curve, but with the laser on and the cavity significantly misaligned so that light cannot be resonant in the cavity. This noise has been converted into frequency spectral density by applying the calibration of of the error signal.

is lower than the hybrid system at 1400 Hz with this RMS being almost entirely driven servo bump for both systems. As with the measurements with the hybrid system, the RMS is shown for frequencies below 10 kHz to minimize the contribution from the servo bump and understand other significant contributors to the noise of the system. The fully analog system measurements are identical to those in the previous section with this RMS being 310 Hz, but we can see here that the lack of 50 Hz and harmonics in the fully digital spectrum produces a lower RMS of 210 Hz. This is despite the higher noise floor, as the RMS is driven more by the peaks than the noise floor. The effects of the servo bumps cannot be discounted, but even with their contribution, the performance of the two systems is very similar.

4.4. Conclusions

In this chapter, digital systems were used to implement frequency control for the ALPS IIa RC. The systems presented used an FPGA on an AMC in mTCA architecture. The firmware was developed internally at DESY, and the software to interface with the firmware was created with MATLAB App Designer.

A digital control servo with analog demodulation electronics was able to suppress the

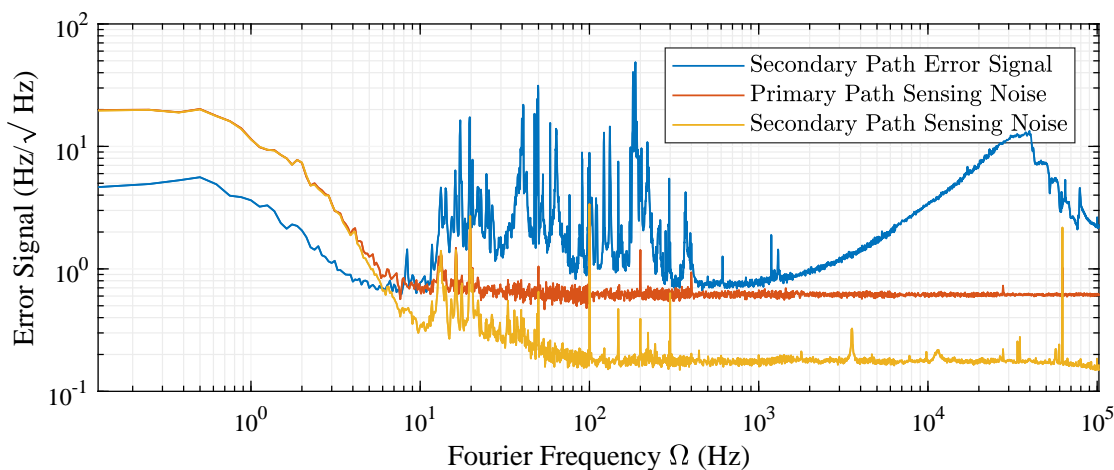


Figure 4.11.: Secondary error spectrum compared with sensing noise. The secondary error spectrum is the same secondary error spectrum from Figure 4.9 and the primary path sensing noise is the same full system primary path sensing noise from Figure 4.10. The secondary path sensing noise is the sensing noise measured with the same electronic setup as used in the measurement of the secondary error spectrum, and the laser on but the cavity misaligned such that the light could not be resonant with the cavity. This noise has been converted into frequency spectral density by applying the calibration of of the error signal.

frequency noise of the cavity to closer than a factor of two away from the analog system in Section 3.3. The additional noise is from the sensing noise of the digital system combined with the analog components. In order to limit the effect of some of those components, digital control with digital demodulation was also implemented with results that were much closer to those of the analog system and the noise performance in some regions was better than that of the analog system.

In both cases, the performance of the digital system compared to the analog system in the same task of the frequency control of the frequency-doubled RL shows the viability of digital systems. This demonstration is important when using the digital system to implement new control schemes to which there is no direct analog comparison. In the next chapter, we will discuss a fully digital system intended to compare the resonance of the two cavities in ALPS IIc.

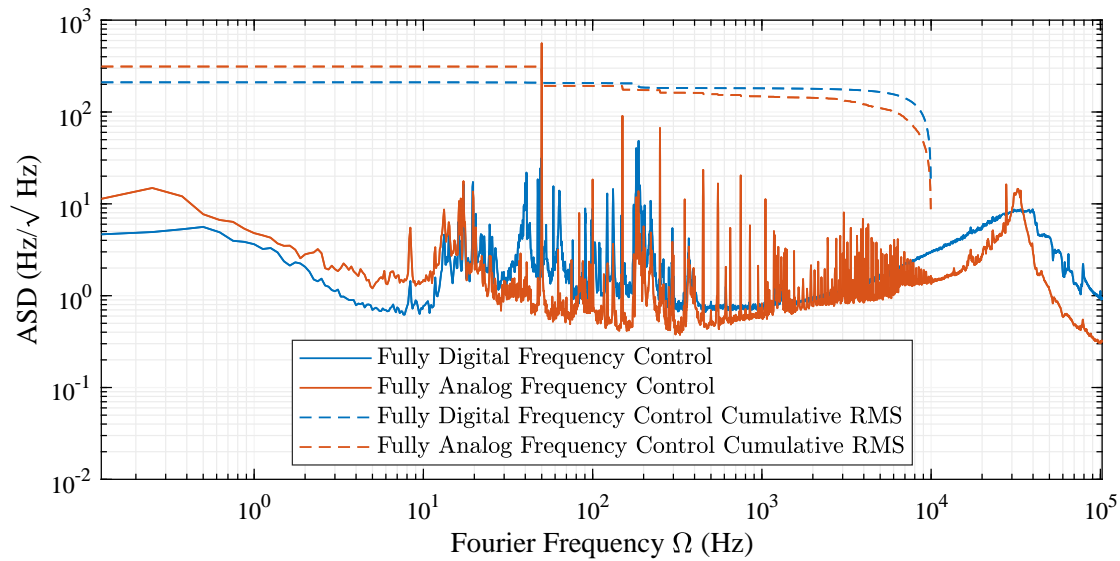


Figure 4.12.: Error spectra of secondary sensing path comparing fully analog system to fully digital system performance. The fully digital spectrum is the error spectrum shown in Figure 4.9 and the analog servo spectrum is the secondary sensing path spectrum shown in Figure 3.11. Additionally shown are the calculated RMS of each curve without including the servo bump, which is very sensitive to the exact phase margin of the system. The RMS of with the fully analog system is 310 Hz with a significant contribution from noise at 50 Hz and the RMS of the fully digital system is 210 Hz with no significant noise peak at 50 Hz or its harmonics.

5. Digital Phase-Locked Loop

In addition to keeping the lasers resonant with the optical cavities, the control systems for ALPS IIc must keep the light in the PC resonant with the RC. This involves measuring the frequency relation between the light fields resonating in both cavities, and then adjusting the length of one cavity in order to maintain a relationship between those fields that indicates this dual resonance condition. Rather than the PDH control systems used in the previous chapters, this system will use a phase-locked loop. This chapter will discuss the design of a digital system to perform this task and the testing performed in ALPS IIa to demonstrate the potential performance of this system in ALPS IIc.

5.1. Phase-Locked Loops

The general concept of a phase-locked loop (PLL) is that the system reads in an oscillating signal, compares it to a reference, and actuates on the plant generating the oscillating signal to match that signal to the reference. This oscillating signal, V_{signal} , is given by

$$V_{signal} = A_{signal} \sin(\phi_{signal}), \quad (5.1)$$

where A_{signal} is the amplitude, and ϕ_{signal} is the phase of the signal. For a constant frequency, ω_{signal} this phase is given by

$$\phi_{signal}(t) = \omega_{signal}t + \phi_{signal}(0), \quad (5.2)$$

but more generally for a frequency that is dependent on time, the phase is given by

$$\phi_{signal}(t) = \int_0^t \omega_{signal}(t') dt' + \phi_{signal}(0) \quad (5.3)$$

which simplifies to Equation 5.2 when the frequency is constant in time. Additionally, this can be calculated in comparison to a constant frequency by integrating the difference between instantaneous frequency and the constant frequency, ω_0 , by

$$\phi_{signal}(t) = \int_0^t \Delta\omega_{signal}(t) dt + \omega_0 t + \phi_{signal}(0), \quad (5.4)$$

where $\Delta\omega_{signal}(t) = \omega_{signal}(t) - \omega_0$. When $\omega_0 = 0$, this simplifies to Equation 5.3.

This signal is then mixed with the reference signal, $V_{ref} = A_{ref} \sin(\omega_{ref}t)$ to give

$$V_{mixer} = V_{ref} V_{signal} = \frac{A_{ref} A_{signal}}{2} [\cos(\omega_{ref}t - \phi_{signal}) - \cos(\omega_{ref}t + \phi_{signal})]. \quad (5.5)$$

If we consider $\omega_0 = \omega_{ref}$ and $\Delta\omega_{signal}(t) \ll \omega_{ref}$, we can apply a low-pass filter to remove the $\cos(\omega_{ref}t + \phi_{signal}) \approx \cos(2\omega_{ref}t)$ term, which leaves us with

$$\begin{aligned} V_{mixer} &= \frac{A_{ref}A_{signal}}{2} \cos\left(\int_0^t \Delta\omega_{signal}(t)dt + \phi_{signal}(0)\right) \\ &= \frac{A_{ref}A_{signal}}{2} \sin\left(\frac{\pi}{2} - \int_0^t \Delta\omega_{signal}(t)dt - \phi_{signal}(0)\right), \end{aligned} \quad (5.6)$$

and we can consider the initial phase offset to be $\phi_{mixer}(0) = \pi/2 - \phi_{signal}(0)$. So we have

$$V_{mixer} = \frac{A_{ref}A_{signal}}{2} \sin\left(\phi_{mixer}(0) - \int_0^t \Delta\omega_{signal}(t)dt\right). \quad (5.7)$$

If we consider that this is our error signal and the control system is driving this signal to be very close to zero, we can assume that the initial phase, $\phi_{mixer}(0)$ is quickly driven to $2m\pi$, and can use the approximation that $\sin(2m\pi + x) \approx x$ when $x \ll 1$ to get

$$V_{mixer} \approx \frac{A_{ref}A_{signal}}{2} \int_0^t \Delta\omega_{signal}(t)dt. \quad (5.8)$$

The input for our system is generated by interfering two lasers together to produce an oscillation, or a beat note, determined by the relative change in phase between the two beams

$$\begin{aligned} V_{signal} &\propto |E_1(t) + E_2(t)|^2 = |E_{1,0}e^{i(\int_0^t \Delta\omega_1(t)dt + \omega_{1,0}t - k_1z_1)} + E_{2,0}e^{i(\int_0^t \Delta\omega_2(t)dt + \omega_{2,0}t - k_2z_2)}|^2 \\ &= E_{1,0}^2 + E_{2,0}^2 + 2E_{1,0}E_{2,0} \cos\left(\int_0^t [\Delta\omega_1(t) - \Delta\omega_2(t)] dt + [\omega_{1,0} - \omega_{2,0}]t - [k_1z_1 - k_2z_2]\right). \end{aligned} \quad (5.9)$$

When the DC terms are filtered out, the phase is aligned, and the nominal frequency difference between the two lasers, $\omega_{1,0} - \omega_{2,0}$, is kept close to the reference frequency, the error signal is

$$V_{mixer} \approx A_{mixer} \left(\int_0^t [\Delta\omega_1(t) - \Delta\omega_2(t)] dt\right). \quad (5.10)$$

This error signal is the input to the PLL. This system actuates on the length of the PC. Because the frequency control loop of each laser is actuating on the frequency of the laser to match the resonance of the cavity, this results in a frequency change of the laser resonant in the PC. This ensures that $\int_0^t \Delta\omega_{PC}(t)dt$ tracks $\int_0^t \Delta\omega_{RC}(t)dt$, which is tracking the resonance of the RC, ω_{RC} . This is how light that is resonant in the PC will be kept resonant in the RC.

The way that the reference frequency, $\omega_{PC} - \omega_{RC}$, is set is different for the two detection methods. As mentioned in Section 1.5, the heterodyne system uses infrared light circulating in the RC both to sense the changes of the resonance of that cavity, and as the local oscillator for the heterodyne detection. As such, the offset frequency

for that laser would have to be an integer multiple of the RC FSR so that both the light field in the PC and the LO field are simultaneously resonant with the RC. For the TES system, the light is supplied by the RL and frequency doubled before being incident on the cavity. Because the properties of the mirrors are different for green light compared to infrared light, the resonance of the cavity for green light is not exactly double the resonance for infrared light. Therefore, it is necessary to empirically determined the offset between the light field circulating in the PC and the infrared RL light that will be frequency doubled and incident on the RC so that this green light and the infrared PC light are simultaneously resonant with the RC.

A simple schematic of the control concept for this PLL is shown in Figure 5.1 for the TES system. The heterodyne system uses a slightly different concept with infrared light.

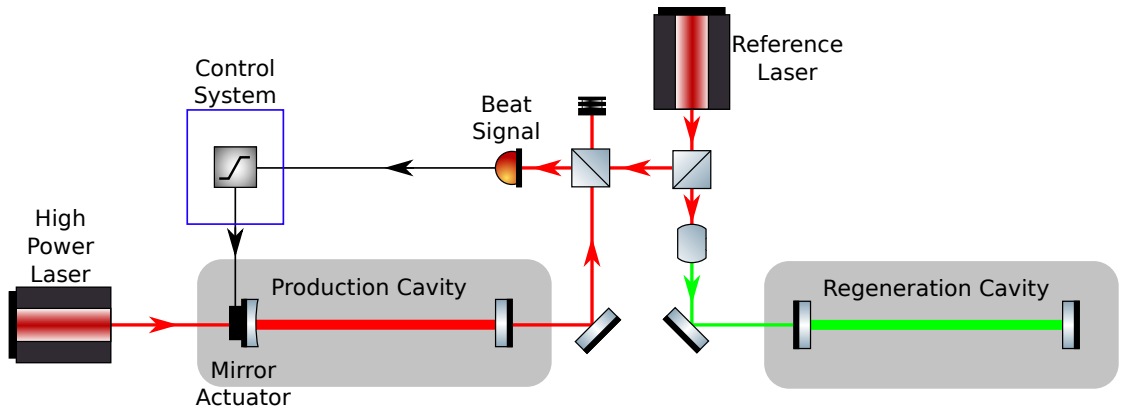


Figure 5.1.: Schematic of concept to ensure dual resonance between the PC and RC with the TES detector. The RL is kept resonant with the PC to track the resonance frequency of that cavity. The light before frequency doubling is compared with the light circulating in the PC provided by the HPL. This comparison allows the control system to adjust the length of the PC to keep the light circulating in that cavity resonant with the RC.

There are also some additional considerations for the control system for a PLL. With the frequency control systems, the input to the servo was proportional to frequency, and the output was proportional to frequency. In this control system, the input is phase and the output is length, which couples linearly to frequency. As such, the equation describing the PLL measurement and control system of is

$$\Delta\omega_{PC}(t) = V_{mixer}(t) * h_{control}(t) = \left(\int_0^t [\Delta\omega_{PC}(t) - \Delta\omega_{RC}(t)] dt \right) * h_{control}(t), \quad (5.11)$$

and when the Lapalace transform of this system is taken, this becomes

$$\mathcal{L}\{\Delta\omega_{PC}(t)\} = \frac{1}{s} [\mathcal{L}\{\Delta\omega_{PC}(t)\} - \mathcal{L}\{\Delta\omega_{RC}(t)\}] H_{control}(s). \quad (5.12)$$

To find the transfer function of this system the output is divided by the input to get

$$\frac{\mathcal{L}\{\Delta\omega_{PC}(t)\}}{\mathcal{L}\{\Delta\omega_{PC}(t)\} - \mathcal{L}\{\Delta\omega_{RC}(t)\}} = \frac{H_{control}(s)}{s}, \quad (5.13)$$

which shows that there is an extra pole at $s = 0$ added by sensing the phase rather than the frequency. This must be considered in the design of any control system for a phase-locked loop.

The final consideration has to do with one of the approximations made above, namely that the phase difference measured is always $\ll 1$. When the phase difference gets larger, the approximation breaks down and the input to the control system is smaller than the phase difference, meaning the system has less gain. When the phase difference gets larger than $\pi/2$, the input decreases with increasing phase, and when the phase difference is larger than π , the sign of the input is inverted, driving the system in the wrong direction. If this only happens occasionally, the system may stay generally controlled, but occasionally change the phase offset by 2π . Unfortunately, this can disrupt the measurement coherence for the heterodyne system [32], and even occasional disturbances of this nature can jeopardize the robustness of this system.

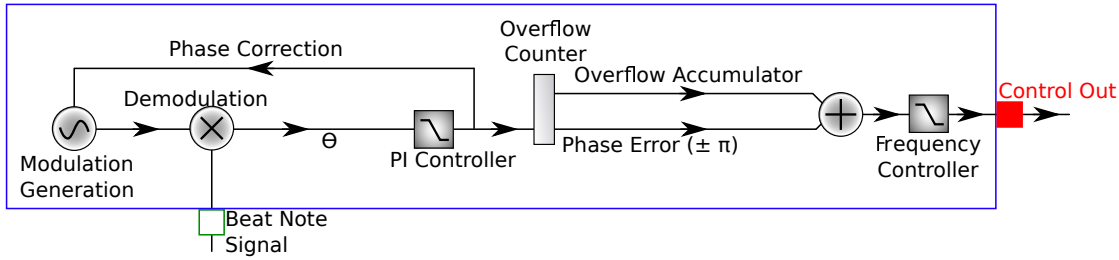


Figure 5.2.: Schematic of a phase-locked loop controller design with a numerically-controlled oscillator for high-speed phase tracking. The phase difference between the modulator and the input signal is fed back to the modulator, thus ensuring that the phase difference between the two is always small. This phase difference from the nominal phase is then tracked through the phase $\pm\pi$ and the number of waves and combined to give the total phase difference between the beat note and the original modulator phase. This net phase difference is the input to the frequency controller, which outputs the signal to control the frequency of the light in the PC.

With this in mind, a more robust system would be able to follow the phase changes with a much greater speed and accuracy than the relatively slow length control system discussed in Section 3.4 is capable of. A system with this capability includes a PLL that instead of actuating directly on the cavity length, actuates instead on a numerically-controlled oscillator (NCO) in an FPGA. This NCO is able to respond significantly faster than the cavity mirror, and is thus able to keep the phase difference between it and the input signal much smaller than would be possible actuating the cavity alone. This system tracks the net phase changes applied to that oscillator, which represents the net phase change away from the nominal phase over many waves and can be used

as the input signal for the frequency control that is linear, does not invert the sign of the input, and is much more robust against losing track of the initial phase position. A simple schematic of the FPGA system for the implementation of this system is shown in Figure 5.2. The control signal for the NCO has a range of $\pm\pi$. As sine waves have a period of 2π , $\sin(\pi + \delta) = \sin(-\pi + \delta)$. This requires the additional complication of a counter that keeps track of how many times this control signal has changed by $\approx \pm 2\pi$, and thus how many waves the phase is away from the nominal phase. The net phase, $\Delta\phi$, is therefore given by

$$\Delta\phi = 2\pi N + \delta\phi, \quad (5.14)$$

where $\delta\phi$ is the phase difference over the range $\pm\pi$, and N is the net overflows counted.

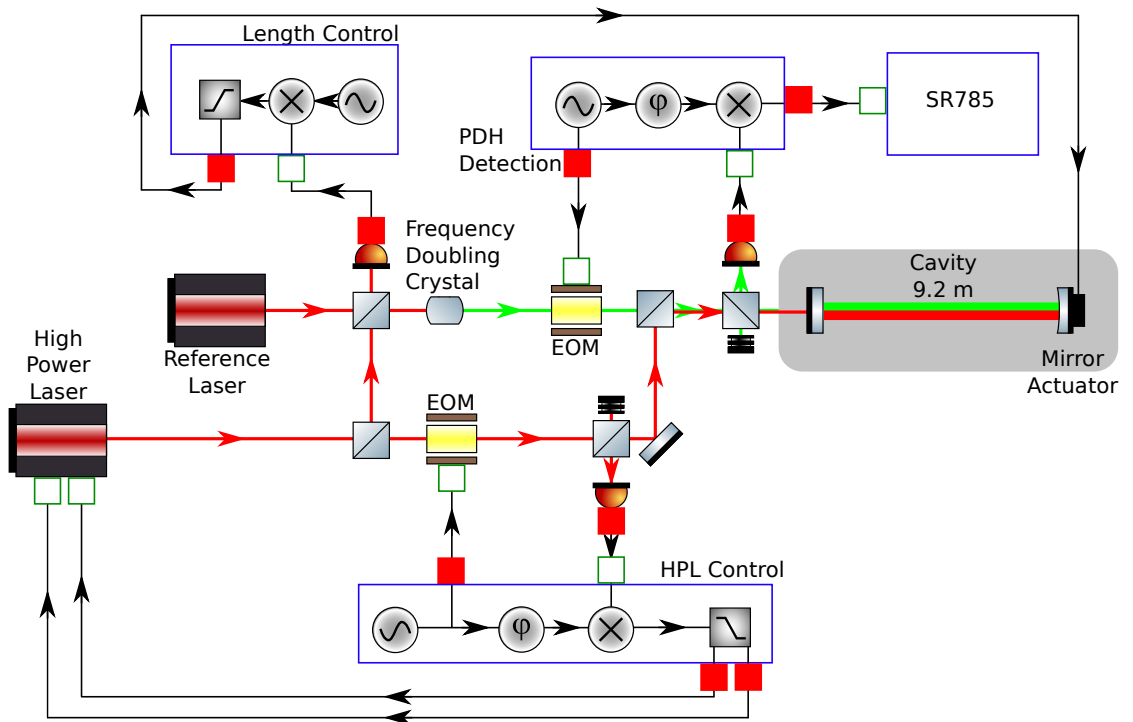


Figure 5.3.: Schematic of a one-cavity test of phase-locked loop length control. The HPL tracks the resonance of the cavity using a frequency control system. The length control system then compares the HPL with RL and actuates on the length of the cavity so that the HPL phase matches the RL phase. The PDH detection system senses the frequency mismatch between the RL and the cavity, which should be indirectly matched to each other.

Though the ALPS IIc control scheme is intended to be used with two cavities, with lasers tracking each resonance and the PLL actuating on the length of one cavity to ensure a constant frequency and phase relationship between the two, demonstrations of the PLL system can be done with only one cavity. A setup for this is shown in Figure 5.3.

The HPL tracks the cavity resonance and then the mirror actuates based on the beat note between the two lasers such that the cavity resonance is indirectly matched to the frequency doubled light of the RL. The frequency noise of the RL compared to the cavity can be tested using the Pound-Drever-Hall technique. This method is more convenient than attempting the full system with both cavities, as the beat signal is always present even when neither laser is resonant with the cavity, and only one frequency control system is necessary.

There are a some technical challenges for both the dual cavity and single cavity phase-locked loop-based length control system that have made length control with this system not yet possible. The largest and most difficult challenge to overcome is that of lock acquisition. When one laser is tracking the cavity resonance, there are large and rapid changes in the beat note frequency. Though the NCO is able to track $\approx \pm 800$ kHz changes in frequency, the beat note frequency often changes by more than that. Even when the phase-lock loop is engaged when the beat note is within the bandwidth that the NCO can track, the system cannot be engaged all at once. This is largely due to the word length of the NCO control, overflow counter, and frequency controller input. The NCO control signal is 18 bits covering the fractional range $\pm\pi$, the overflow counter is 32 bits covering $2\pi N$, making the full net phase $18 + 32 = 50$ bits. The frequency controller input is 18 bits. As such, some truncation of both the overflow counter and the NCO control signal is necessary. If all 18 bits of the input were used for the overflow counter, we could keep track of phase changes of up to $2^{18} = 262144$ waves, but then the minimum resolution would be ± 1 wave. This would introduce a significant amount of quantization noise, as the noise level calculated in Equation 2.37 is directly proportional to the LSB. Alternatively, if all 18 bits were used for the NCO control signal, the controller could only cover $\pm\pi$. Even if all 32 bits were able to be used, at a frequency difference between the nominal and actual beat note of 800 kHz, the maximum number of waves counted would exceed the capability of the input and overflow in 0.33 s. The number of waves able to be counted, and also the amount of time necessary to exceed that at a given frequency offset, is reduced by 2^M , where M is how many bits of the fractional wave phase resolution are introduced.

The solution that has been attempted is, when the beat note is close to the nominal offset frequency, turn up the gain slowly so that the system can start reducing the number of waves before truncating non-zero bits. While turning on the gain, the controller transfer function would need to be flat, producing a net $1/f$ slope. This is because turning on the proportional gain slowly means that the unity gain frequency slowly increases to the nominal unity gain frequency. The increased slope that is necessary to achieve higher gain at low frequencies means that there would be negative phase margin as the unity gain frequency went through these regions, resulting in an unstable control loop. Unfortunately, this also means that there is less gain at low frequencies than is necessary to prevent the beat signal from going beyond the range of the NCO or exceeding the number of waves able to be counted. If this process were to work, the low-frequency gain could be increased after the desired unity gain frequency was achieved with the proportional gain. Unfortunately, even automating this process to increase the speed of each steps has not produced the desired result.

The net result of these challenges is that lock acquisition is not a yet smooth process and results in large and sudden changes of the control signal as the limits of the system are reached, which the frequency control system would not be able to compensate for. Work is ongoing on developing methods for this, but these difficulties will not be as pronounced in the ALPS IIc system, as the frequency changes due to length changes are smaller by more than a factor of 10. There is also the possibility of gaining some understanding of the system by actuating on the frequency rather than the length.

5.2. Phase-Locked Loop for Frequency Actuation

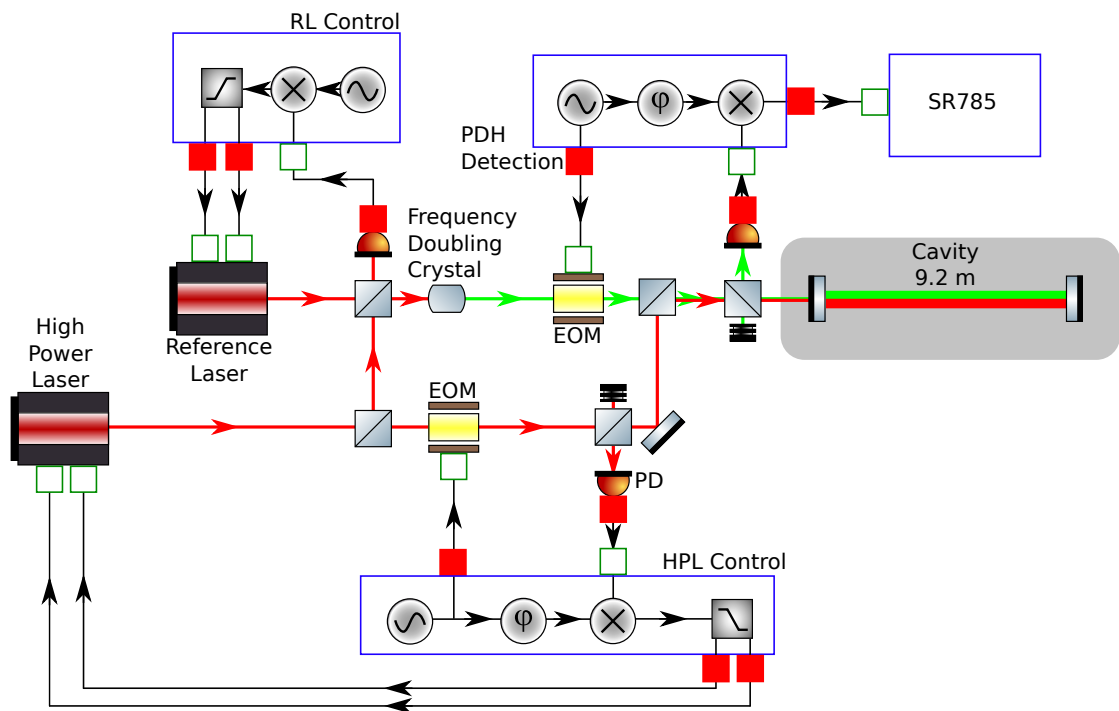


Figure 5.4.: Schematic of a phase-locked loop controller and sensing system for the ALPS IIa RC. Rather than actuating on the length of the cavity to match the HPL phase to the RL phase, this system actuates on the RL phase to match it to the HPL phase. As the HPL is tracking the cavity resonance, the RL should be indirectly matched to the cavity resonance. The frequency mismatch between the RL and the cavity can be measured with the PDH sensing system.

A schematic showing the experimental setup to control the frequency of the RL such that it is resonant with the ALPS IIa RC using a PLL, and measure the performance of this system is shown in Figure 5.4. For this system, the HPL is frequency controlled with the system discussed in Section 3.2. Then, to produce the error signal for the PLL control, the HPL and RL are interfered before the RL light is frequency doubled

5.2. Phase-Locked Loop for Frequency Actuation

to green light. This is compared to an offset frequency that is set such that the RL is maximally resonant in the cavity. Finally, the Pound-Drever-Hall technique is used to determine how much frequency noise is present on the green light. Unlike in previous chapters, this is a fully out-of-loop measurement, as the measurement systems for the control loop and the frequency sensing are entirely separate. This is similar to the length control system shown in Figure 5.3 except that the PLL-based controller is actuating on the RL frequency to match it to the cavity resonance based on the offset frequency rather than actuating on the cavity length to match the resonance to the laser frequency. As the length of the cavity is not changing, there can be large changes of the control signal being sent to the RL frequency that do not affect the control of the HPL and thus a smooth lock acquisition is not necessary. This should give us information on how well this system is able to maintain the resonance condition compared to systems that directly measure this resonance condition.

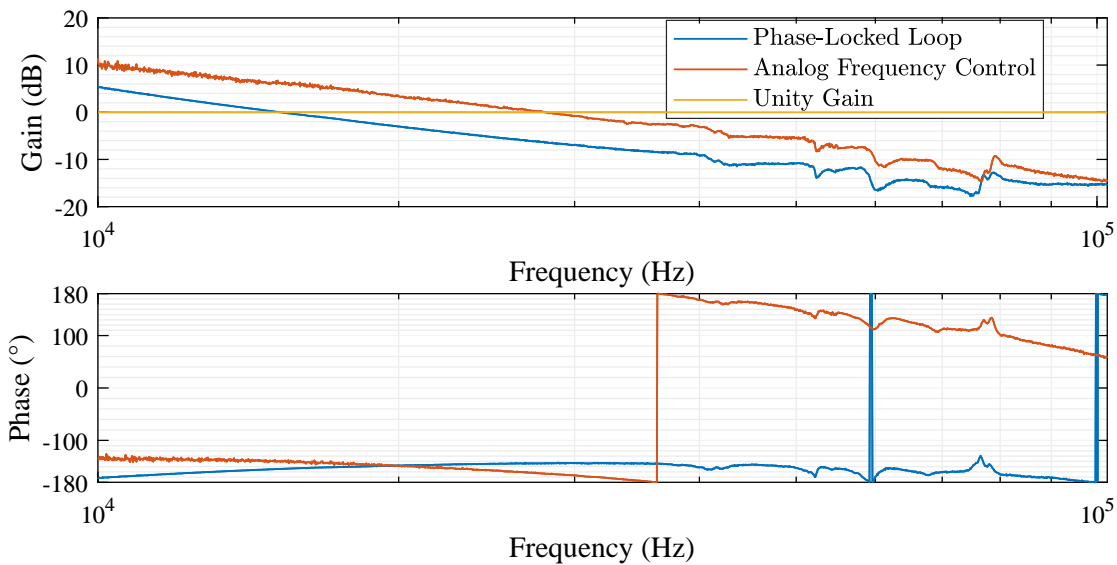


Figure 5.5.: Open-loop transfer function of the phase-locked loop compared to the analog frequency control. The unity gain frequency of the analog frequency control system is 28 kHz with a phase margin of 17 $^\circ$ compared to the phase-locked loop system that has a unity gain frequency of 15 kHz and a phase margin of 28 $^\circ$. Both transfer functions were measured by injecting a swept sine on the control signal and comparing the control signal with the swept sine to the control signal right before the swept sine was injected. The measurements were made with an averaging factor of 100 and an input of between 0.1 mV and 5 mV peak-to-peak.

The open-loop transfer function of this PLL-based system compared to the analog frequency control from Section 3.3 is shown in Figure 5.5. Like the system with digital demodulation, the PLL has more phase available than the analog frequency control. The limit of this system is resonances present at ≈ 300 kHz, which cause significant oscillations

at proportional gain settings well below the point at which the phase margin result in a significant servo bump. Though they are outside of the range of the transfer function shown, they were seen by the frequency those oscillations at higher proportional gain settings. The 6x6 state space controller does not have enough coefficients available to effectively notch out these resonances as was done with the length actuator in Section 3.4. As a result, the unity gain frequency of the PLL is 15 kHz with a phase margin of 25°. The PLL system has less phase margin at lower frequencies than the analog system. This is because poles were placed as close as possible to the unity gain frequency in order to achieve the most aggressive gain slope possible, to make up for the lower proportional gain of this system.

Calibrating the PDH signal for this system was not done using this unity gain frequency, as the control is not applied directly based on this PDH signal, but rather the PLL error signal. Instead, the RL was locked to the cavity using the analog frequency control system, an open-loop transfer function as well as a control and error spectrum of that system was taken, and that was used to calibrate the PDH signal.

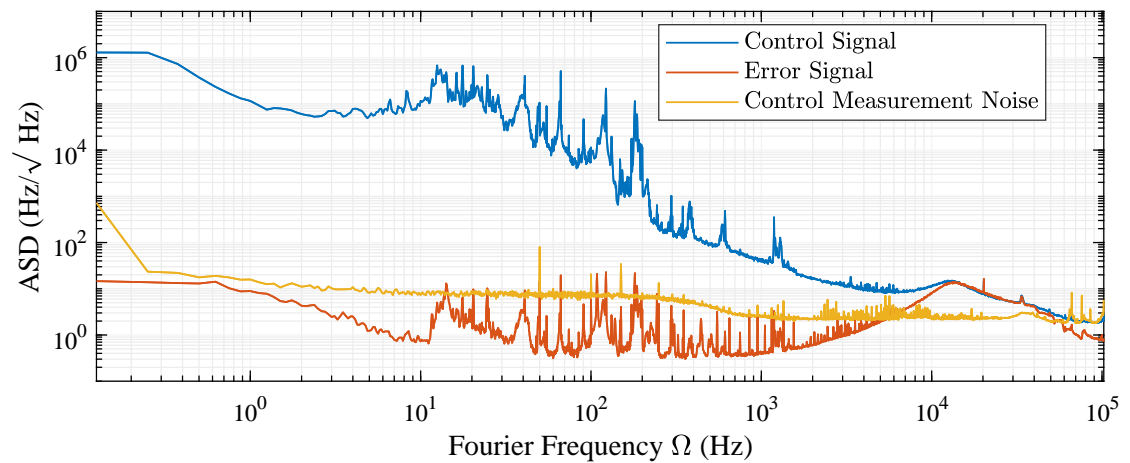


Figure 5.6.: Control and PDH spectra for the phase-locked loop. The control signal is the signal sent to the laser piezo. The error signal used by the control loop is not pictured and only the frequency noise signal measured by the PDH sensing path shown in Figure 5.4 is shown. The noise seen at lower frequencies in the control signal is primarily caused by movements of the cavity mirrors, whereas the higher frequency noise is caused by laser frequency noise. The unity gain frequency is where the signals cross. The rise near that frequency is known as a servo bump and is due to oscillations in the control loop. The internal noise of the SR785 measurement system for the control signal is also shown and limits the measurement of the control signal at high frequencies.

The control and PDH signal spectra are shown in Figure 5.6, along with the measurement limits of the SR785 for the control signal spectrum. The PDH signal spectrum is large enough compared to the measurement limits for that spectrum that they have

been omitted. The control signal spectrum is very similar to the control signal spectrum of the previous frequency control systems, which is expected as the RL is tracking the frequency of the HPL, which is locked to the cavity. We also see that the point where the control and PDH signal are equal is very close to the unity gain frequency, despite the control system not measuring this frequency but rather phase changes between the RL and the HPL.

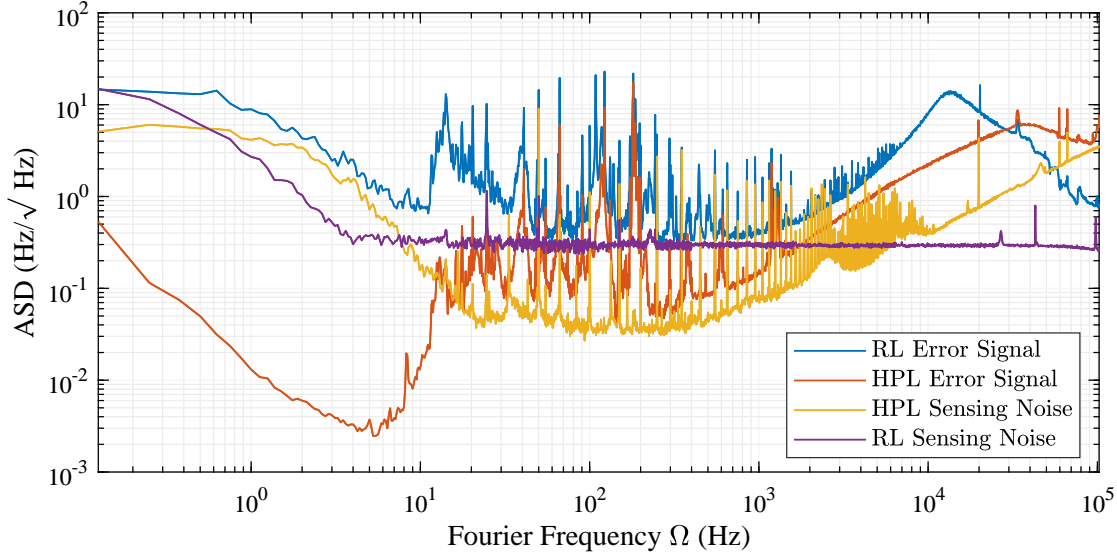


Figure 5.7.: Phase-locked loop PDH spectrum compared to noise sources. The RL error signal is the same as shown in Figure 5.6. As the PLL tracks the HPL, any noise present on at laser within the control bandwidth will also be present on the RL. Therefore, the noise spectrum of the frequency control of the HPL and the sensing system noise are shown in orange and yellow, respectively. These are measured the same way as the measurements of the HPL frequency control system in Section 3.2. The RL sensing noise is the noise of the PDH sensing system. This was measured using the same setup as the measurement of the error spectrum with the laser on but the cavity significantly misaligned such that the laser could not be resonant with the cavity. This should include all electronic and optical sources of noise. All error and sensing noise spectra have been converted into the equivalent RL frequency noise by applying the error signal calibration and a factor of 2 as necessary to account for the frequency doubling of the RL.

Figure 5.7 shows the PDH spectrum of the PLL frequency control compared with different sources of noise that contribute to this spectrum. The blue curve is the spectrum of the measured PDH signal, which is the same spectrum as shown in Figure 5.6. The first source of noise is the HPL error spectrum, which is the orange curve. As the PLL is trying to minimize any difference between the HPL and the RL, any residual error in the HPL frequency control will directly couple into the frequency noise of the RL. The ALPS IIa cavity pole has been applied to the measured error spectrum to accurately depict the frequency noise spectrum of the HPL, and it has additionally been multiplied

by 2 to compare it with the RL frequency noise spectrum because of the frequency doubling before the RL light is incident on the cavity. The yellow curve is the sensing noise of the HPL frequency control, also with the cavity pole and factor of 2 applied. As discussed previously, the sensing noise is combined with the measured error spectrum as the control system imprints the sensing noise on the light in the cavity. There is not a strong contribution from this sensing noise except at frequencies less than 10 Hz, when this sensing noise begins to contribute significantly to the RL PDH spectrum. One thing to note is that, above the unity gain frequency, the RL is not tracking the HPL and therefore this part of the HPL error and sensing spectra do not contribute to the RL PDH spectrum. The final limit is the sensing noise of the RL PDH system, which is the purple curve. This does not limit the performance of the system, but rather the ability to measure the performance of the system. It is clear that there is a noise floor from the electronic portion of this sensing noise, in addition to a contribution from the low-frequency sensing noise.

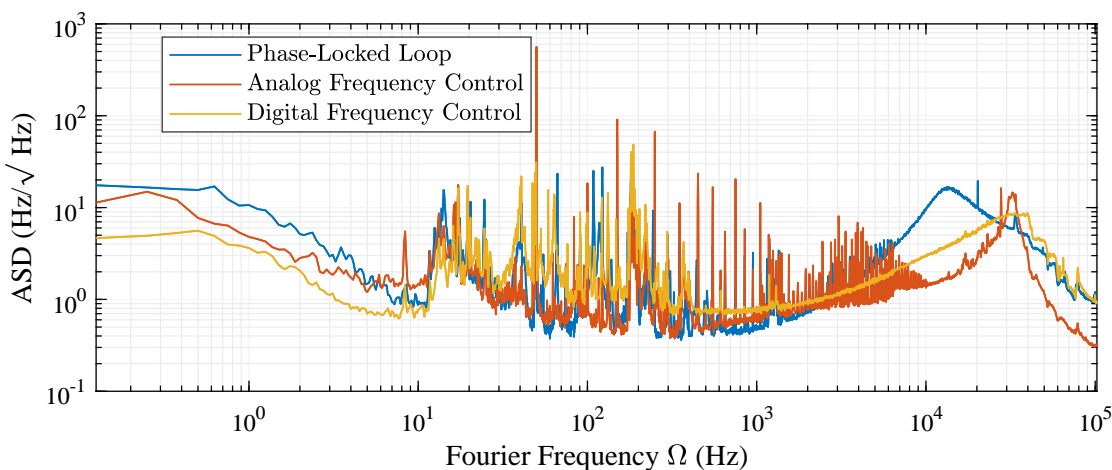


Figure 5.8.: Phase-locked loop PDH spectrum compared to analog frequency control error spectrum. The phase-locked loop error spectrum is the same as that in Figure 5.6. The analog frequency control is the secondary error spectrum in Figure 3.11. The digital frequency control spectrum is the error spectrum in Figure 4.9. The three spectra demonstrate that each loop achieves similar noise suppression and has a similar noise floor. The primary difference between the three is the different servo bumps near the unity gain frequency of each.

Figure 5.8 shows the PDH spectrum of the PLL compared to the analog frequency control in Section 3.3 and the digital frequency control in Section 4.3. The lower unity gain frequency for the PLL is seen in the servo bump at a lower frequency. The servo bump is also wider for the PLL than for the analog frequency control, though similar to the digital frequency control. Otherwise, the three spectra are quite similar to each other. The PLL system has a similar noise floor to the analog system, but the peaks for the 50 Hz noise are much closer to those for the digital frequency control system.

Though not shown, the RMS for the PLL is 1800 Hz compared to the RMS of 1100 Hz of the analog frequency control, and the RMS of 1400 Hz for the digital frequency control in Section 4.3. The primary driving factor of the RMS for each of these systems is the servo bump. If we consider only the noise below 5 kHz to avoid the contribution of the servo bump, the PLL system spectrum has the lowest RMS at 120 Hz, compared to the digital system with an RMS of 130 Hz and the analog system with an RMS of 290 Hz. A greater reduction of the effect of the resonances at higher frequencies provided by a control system with more coefficients would allow more proportional gain and a higher unity gain frequency. This could reduce the RMS of the PLL system even further, and allow for a reduction of the servo bump as higher frequencies have less phase lag with the current control setup.

5.3. Simulated Length Actuation

Though length control has not been achieved yet, it is possible to determine the possible performance of length control once it is achieved. This can be done by controlling the frequency of the laser, but with a control loop transfer function that matches one used for length control. Using the frequency actuator in this way should demonstrate what would be possible for length control using the same system. This is done in the same way as the frequency control in Section 5.2 using the system shown in the schematic in Figure 5.4, but using a transfer function similar to that of the compensated length control system in Section 3.4.

The length control has a unity gain frequency approximately an order of magnitude lower than that of the frequency control. Therefore, this simulated length control will need a unity gain frequency similar to achievable length control unity gain frequencies. The open-loop transfer function of this simulated length control is shown in comparison to the compensated length control transfer function in Figure 5.9. The transfer function of these systems is very similar below the unity gain frequency. Because the phase-locked loop is not using the length actuator, it does not interact with the actuator resonances, the compensation for these resonances, or the phase loss due to both of these elements. However, the phase loss at the unity gain frequency is not the limiting factor for the length control but rather those mechanical resonances. Therefore, we do not expect this phase difference to contribute to a large difference between the two systems. The unity gain frequency of the phase-locked loop simulation is 3.7 kHz compared to 3.9 kHz for the compensated length control.

The control and PDH spectra, as well as the measurement limits for the control spectrum are shown in Figure 5.10. As with the phase-locked loop data in Section 5.2, the measurement limits of the PDH spectrum are well below the PDH spectrum and are therefore omitted. Also similar to Section 5.2, the control and PDH spectra meet just at the unity gain frequency.

In addition to the measured open-loop transfer function in Figure 5.9, the servo gain can be calculated by dividing the control signal by the PDH signal. This should give the suppression of the control system. This was done for both the PLL length control

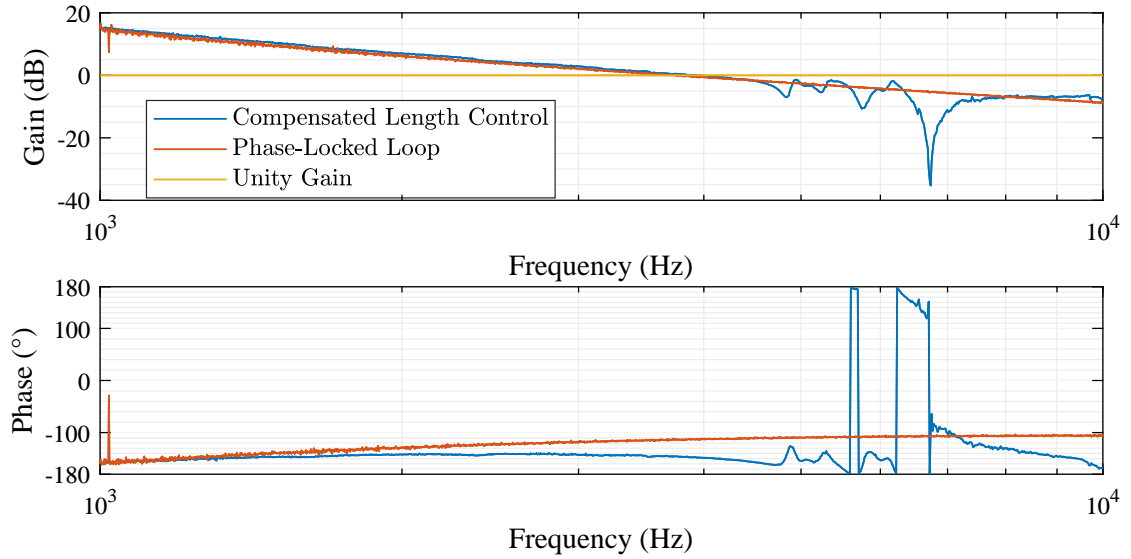


Figure 5.9.: Open-loop transfer function of the phase-locked loop length control simulation compared to the compensated length control. The unity gain frequency of the compensated length control system is 3.9 kHz compared to the phase-locked loop length control simulation that has a unity gain frequency of 3.7 kHz. The resonances from the mirror actuator are not present in the transfer function for the phase-locked loop length control simulation. Both transfer functions were measured by injecting a swept sine on the control signal and comparing the control signal with the swept sine to the control signal right before the swept sine was injected. The control signal of the length control system was measured and modified before the high voltage amplifier. The measurements were made with an averaging factor of 100 and an input of between 0.1 mV and 5 mV peak-to-peak.

simulation as well as the compensated length control and shown in Figure 5.11. For the length control, the spectra for the secondary PDH sensing path was used. The out-of-loop PDH sensing path was used for the PLL. The servo gain for the two systems is very similar, which was intended by the design of the servo of the PLL. The major difference is the compensation for the resonances seen above the unity gain frequency of the length control system that are not present in the PLL system.

The sources of noise for this PLL are identical to the noise sources for the PLL in Section 5.2 shown in Figure 5.7. They are shown in comparison with the measured error spectrum for this length control simulation in Figure 5.12. With these control parameters in comparison to the previous control system, there is less suppression and thus the electronic noise floor is never reached. However, just as with the previous measurement, the low-frequency sensing noise from both the HPL frequency control and the PDH sensing path contribute significantly below 10 Hz. Additionally, as with the previous system, there the control system is not exerting control above the unity gain frequency, and therefore the HPL frequency and sensing noise can exceed the RL error

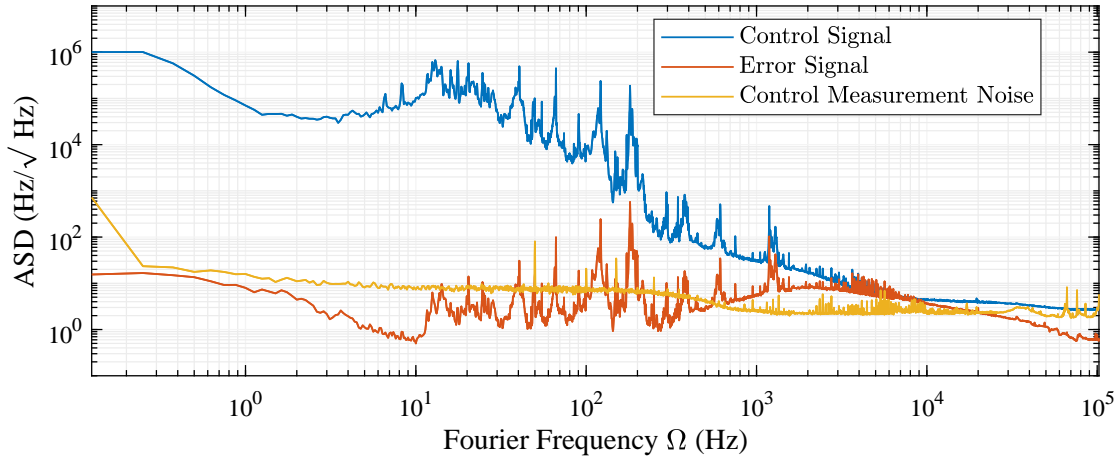


Figure 5.10.: Control and PDH spectra for the phase-locked loop with a transfer function to simulate the performance of the phase-locked loop actuating on length. The control signal is the signal sent to the laser piezo. The error signal used by the control loop is not pictured and only the frequency noise signal measured by the PDH sensing path shown in Figure 5.4 is shown. The noise seen at lower frequencies in the control signal is primarily caused by movements of the cavity mirrors, whereas the higher frequency noise is caused by laser frequency noise. The unity gain frequency is where the signals cross. The internal noise of the SR785 measurement system for the control signal is also shown and limits the measurement of the control signal at high frequencies.

spectrum.

As the suppression of each system is similar, and the sensing noise does not contribute significantly, one would expect the spectra to be similar. Figure 5.13 shows that this is the case. The opto-mechanical setup of the cavity is not exactly the same between measurements, so there are some differences in the peaks that are seen, but the majority of features are nearly identical. As with the servo gain, the mechanical resonances of the mirror actuator are visible in the error spectrum for the length control but not in the PDH spectrum for the PLL as the actuator for that system is the laser frequency, which does not have resonances in that frequency range. These are visible both just above the unity gain frequency and in the ~ 10 kHz region for the compensated length control.

The final comparison between the two systems is to project the performance of each onto the ALPS IIc cavity. This projection is performed as described in Section 1.5 and in the same way as performed in Section 3.4. The results, along with the RMS, are shown in Figure 5.14. The RMS of the compensated length control was calculated to be 1.0 Hz and the RMS of the simulated length control is 2.5 Hz. Just as with the compensated length control, the resonance at 180 Hz is a significant contributor to the simulated length control RMS, to a larger degree than the length control system. There is an additional contribution from a resonance at 120 Hz that is not present in the length control system. Either of these could be reduced by the use of resonant gain, but the

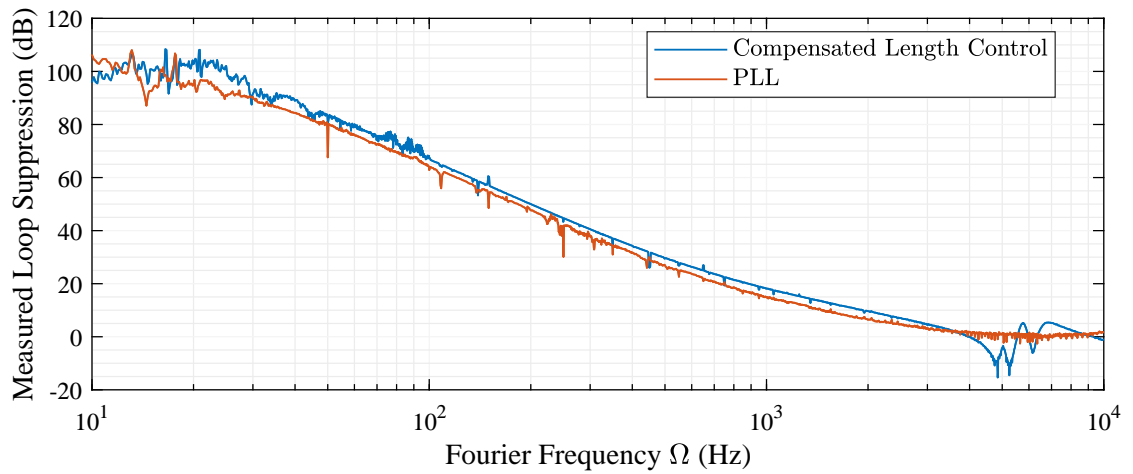


Figure 5.11.: Calculated servo gain of the phase-locked loop length control simulation compared to the compensated length control. This gain was calculated by dividing the control spectrum by the error spectrum. The control and error spectra used for the calculation of the compensated length control suppression are the control and secondary path error signals shown in Figure 3.24. The control and error spectra used for the calculation of the phase-locked loop length control simulation are the control and frequency noise signals shown in Figure 5.10.

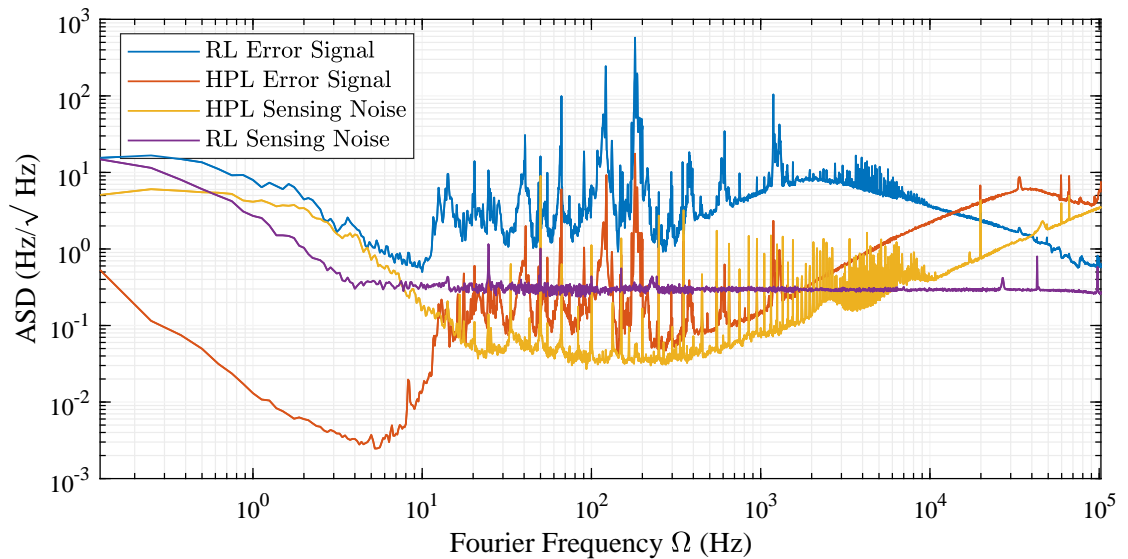


Figure 5.12.: Phase-locked loop length control simulation PDH spectrum compared to noise sources. The PDH spectrum is the same as shown in Figure 5.6 and the noise sources are the same as shown in Figure 5.7.

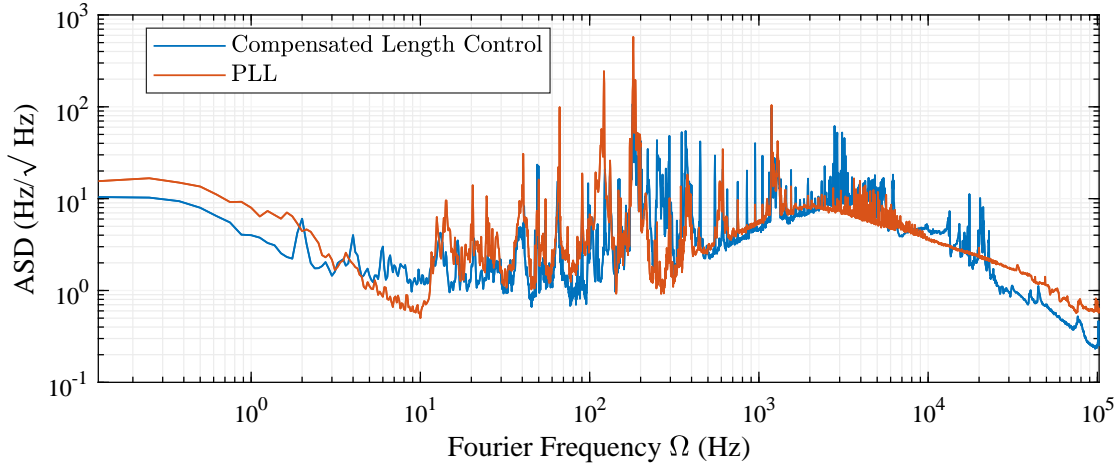


Figure 5.13.: Phase-locked loop length control simulation PDH spectrum compared to compensated length control error spectrum. The compensated length control spectrum is the secondary sensing path error spectrum in Figure 3.24 and the PLL spectrum is the frequency noise spectrum in Figure 5.6.

system meets the ALPS IIc requirement of 3.0 Hz as it is.

5.4. Measuring Cavity Free Spectral Range and Linewidth Using a Phase-Lock Loop

It is also possible to use the PLL frequency control system in Section 5.2 to probe the cavity's response to frequencies that are a constant offset away from the cavity resonance. The frequency offset does not have to be set such that the RL is resonant with the cavity, and can be slowly adjusted to measure how much power is built up at different offset frequencies. This can be used to scan across a full free spectral range to obtain the linewidth of the cavity for green, as well as the length of the cavity. When expanding beyond the 1-dimensional optical cavity, this can also be used to determine the coupling between the input laser beam and different higher-order spatial modes, as well as some information about the cavity geometry that couples into the resonance frequency of those higher-order spatial modes through the Gouy phase. This section will focus on using this system to measure the linewidth and the length of the cavity.

The transmitted power is directly proportional to the circulating power. Measuring that with a photodetector can show changes to the circulating power. Determining the exact magnitude of this power is less important than determining the shape and its relationship to the offset frequency in this experiment. Figures 5.15a and 5.15b each show three measurements of resonances, with the resonance for each figure separated by a free spectral range.

In order to determine the center frequency and FWHM, we start with Equation 1.53.

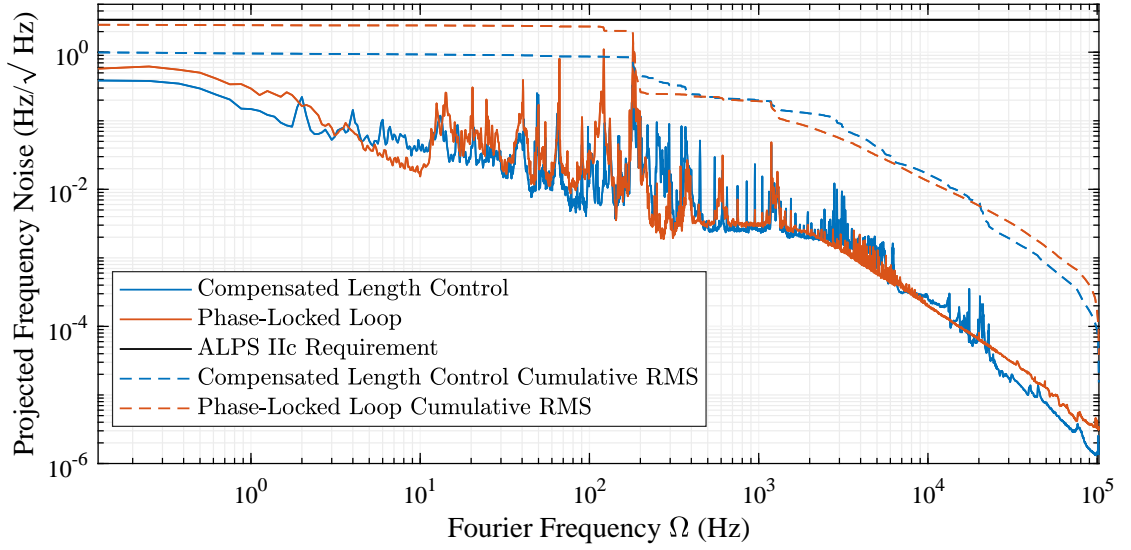


Figure 5.14.: Phase-locked loop length control simulation PDH spectrum compared to compensated length control error spectrum with both projected onto the ALPS IIC cavities. The compensated length control spectrum projected is the secondary spectrum shown in Figure 3.24, which is also projected onto the frequency onto the ALPS IIC cavities in Figure 3.27. The PLL frequency noise spectrum projected is the frequency noise spectrum in Figure 5.10. The spectra are converted into the expected spectra for IR light by dividing by a factor of two, and then projecting the ALPS IIC RC noise onto the ALPS IIC PC by dividing by the ratio of the two cavity lengths. Finally, Equation 1.61 is applied where A is the spectrum of the frequency noise projected to be present in the ALPS IIC PC which is the same as calculating the RMS of the frequency noise filtered by the low-pass behavior of the cavity. As such, this cumulative RMS is displayed by the dashed lines. Additionally, shown in black is the ALPS IIC requirement of 3.0 Hz. The RMS for the compensated length control is 1.0 Hz which meets the requirement. The RMS for the PLL is 2.5 Hz which also meets the requirement.

As the signal measured is a voltage that is proportional to the power circulating in the cavity with an offset caused by electronics and ambient light, this equation is modified to become

$$V(f) = V_{peak} \frac{1}{1 + \left(\frac{2[f - f_{peak}]}{\Delta f_{peak}} \right)^2} + V_{offset}. \quad (5.15)$$

This equation was then fit to the data with the parameters V_{peak} , f_{peak} , Δf_{peak} , and V_{offset} . The data in Figure 5.15 is shown with V_{offset} removed, and V_{peak} normalized to 1. The f_{peak} and Δf_{peak} give us the center frequency and FWHM of the resonance, respectively, for each measurement.

For the lower offset frequency resonance, the measured center frequency was 2.003 MHz \pm 200 Hz. The measured center frequency for the higher offset frequency resonance is

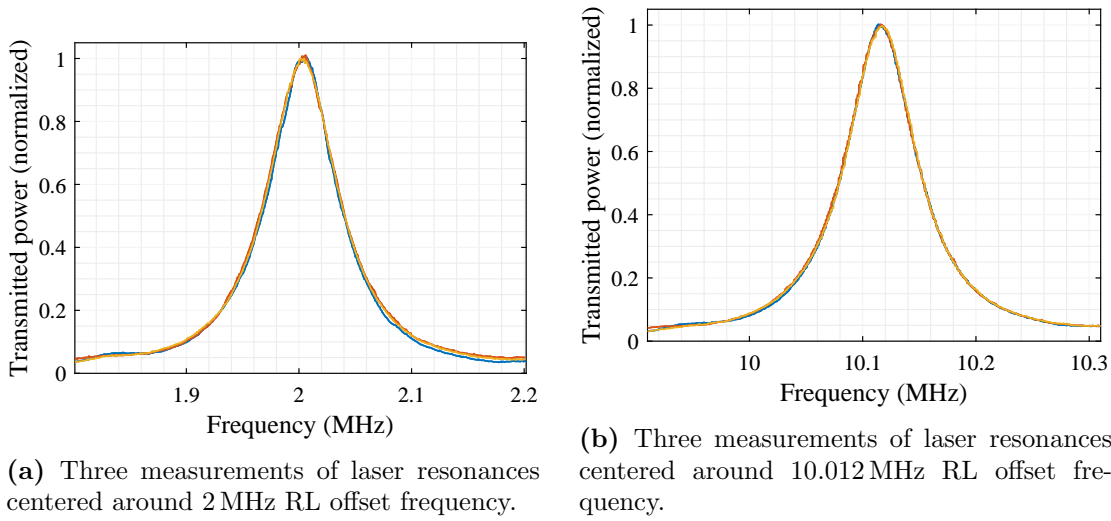


Figure 5.15.: Measurement of the transmitted power versus the RL offset frequency for two cavity resonances separated by a free spectral range. This was performed by matching the HPL to the cavity and matching the RL to the HPL. The offset frequency of the two lasers is then changed so that the frequency doubled RL moves from not resonant, to resonant, back to not resonant. How resonant the RL is with the cavity is measured with the cavity transmitted power. This was then fit to Equation 5.15. The center frequency of the lower resonance was found to be $2.003 \text{ MHz} \pm 200 \text{ Hz}$ and the higher resonance was found to be $10.116 \text{ MHz} \pm 400 \text{ Hz}$.

$10.116 \text{ MHz} \pm 400 \text{ Hz}$. One thing to note is that since these measurements are made with the offset frequency of the RL before it is frequency doubled, the light circulating in the cavity had double the offset frequency. With this in mind, the FSR for the light in the cavity is $16.226 \text{ MHz} \pm 700 \text{ Hz}$. This corresponds to a length of $(9.2444 \pm 0.0004) \text{ m}$.

The FWHM calculation is done much the same way, except each cavity resonance can be used to calculate the FWHM independently. As such, we have six measurements of the FWHM, which are all shown overlaid around their center frequency in Figure 5.16. Just as above, the measurement of the frequency offset needs to be doubled to calculate the frequency changes to the green beam. This gives us a FWHM of $(148 \pm 2) \text{ kHz}$. As a note, this is smaller than the expected FWHM calculated in Section 1.5, which was 160 kHz . This can be explained by having a slightly lower transmission on either mirror. Keeping the transmission of the other mirror as specified, a transmission of 4.6% for the first mirror or a transmission of 0.6% for the second mirror would completely explain this slightly narrower linewidth.

5.5. Conclusions

A PLL is an important technique in maintaining a constant phase and frequency relationship. This is an important task for ALPS IIc to maintain a phase and frequency

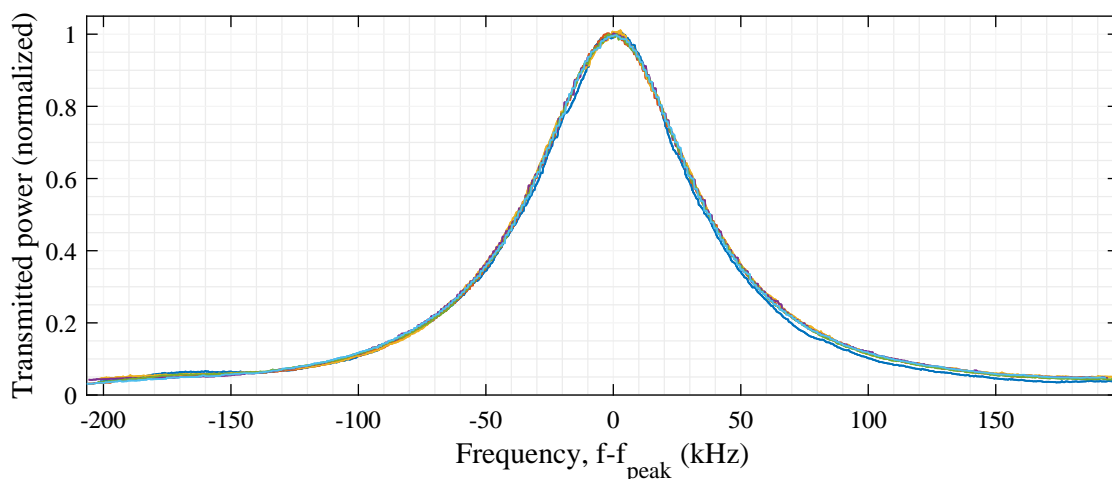


Figure 5.16.: All cavity resonance measurements overlaid. The resonances measured in Figure 5.15 had their fitted center frequency subtracted to show the width of the resonances and their deviations from each other.

relationship between the light circulating in the two optical cavities. This phase-locked loop can be implemented using the length of the ALPS IIc PC as the actuator, and it can be made more robust by maintaining an NCO and using the control of that system as the input to the length control servo.

Additionally, the performance of this system can be tested using only a single cavity with the ALPS IIa RC. Though the length control system is not yet able to be implemented, the performance of this system actuating on the laser frequency compared to dedicated frequency control systems is within a factor of two.

Using this frequency actuation system, the performance of a length control system can be simulated by implementing the same transfer function that was used for a length control system. This simulation indicates that such a control system would have similar performance to the primarily analog length control system and also meets the ALPS IIc requirements on phase noise.

Work is ongoing to overcome the difficulties with lock acquisition that limit the use of this system to frequency control rather than length control.

6. Conclusions

The Any Light Particle Search II (ALPS II) intends to search for a class of novel particles known as axion-like particles. The existence of these axion-like particles is suggested both by theoretical extensions of the standard model and by astrophysical observations. A number of experiments searching for these particles have been conducted with different sources of the axion-like particles. ALPS II is a light-shining-through-a-wall experiment, which intends to produce axion-like particles using the interaction between photons and a magnetic field. These axion-like particles will then pass through a wall to block the photons used to generate them. Finally, the axion-like particles will oscillate back into photons behind the wall using the interaction between the axion-like particles and a magnetic field. The detection of regenerated photons would indicate the existence of axion-like particles and would not depend on a model of any external source of axion-like particles.

The use of optical cavities is vital to the success of the ALPS II experiment. These cavities will both enhance the rate of generated axion-like particles on one side of the wall as well as the probability of them oscillating back into photons. In order to effectively use these cavities, control systems are necessary to maintain a match between the input laser light and the resonance condition of the cavity. These control systems can either actuate on the frequency of the input laser light or on the length of the cavities. ALPS II is conducted in two phases: ALPS IIa for technology maturation and demonstration, and the full-scale experiment ALPS IIc. ALPS IIc will require systems to ensure a high power build-up factor in each of the 124.4m long cavities as well as a good match between the resonances of the two cavities such that light in the production cavity (PC) would be resonant with the regeneration cavity (RC). In order to achieve the desired sensitivity of $g_{A\gamma\gamma} = 2 \times 10^{-11} \text{ GeV}^{-1}$, the requirements on the cavities and the match between the cavities are very demanding. The requirement that is most relevant for projection from the measurements in this thesis is the dynamic phase noise between the two cavities. The goal for that dynamic noise is a maximum 3.0 Hz of RMS frequency noise in ALPS IIc.

ALPS IIa is an important step to the full-scale ALPS IIc experiment. ALPS IIa has the facilities for two cavities to mirror the PC and RC in ALPS IIc. Control systems can be designed and tested to determine their suitability for use in ALPS IIc, and alternative designs can be compared based on their performance in the short-scale experiment. Additionally, these systems can be used to investigate phenomenology that is important for ALPS IIc. For the measurements made in this thesis, only the RC was in place in ALPS IIa, and all measurements were made on that cavity.

The performance of systems in ALPS IIa as well as drivers of this performance are important to characterize. This is both to explore their suitability for use in ALPS IIc

and to compare to digital systems to see what the limitations of different implementations of the same system are. The two main performance drivers are the transfer function of the servo, and the sensing system noise. As such, these must be investigated for all of the systems currently in use in ALPS IIa as well as any digital alternatives in order to understand any differences in performance between the two systems.

The analog control systems used in the RC of ALPS IIa have been characterized. These include frequency control of both the infrared light from a high-power laser (HPL) and the green light from frequency-doubling a reference laser (RL). These frequency control systems only constitute part of the frequency control system intended for the ALPS IIc cavities, and as such projecting their performance onto ALPS IIc is not relevant. However, there is also a length control system using a custom-designed actuator both with and without digital compensation for the actuator's mechanical resonances. This length control system is similar to the system that will be used to match the resonances between the two cavities in ALPS IIc. The length noise of this system can be projected to the expected performance for the same system in ALPS IIc. The projected RMS of the length noise projected onto the frequency noise of ALPS IIc without compensating for the mechanical resonances is 9.8 Hz, which does not meet the requirements. The length control system with compensation is able to suppress the projected frequency noise of ALPS IIc to an expected RMS of 1.0 Hz, which exceeds the requirements.

A number of digital control systems for both frequency control and controlling the relationship between the two optical cavities were developed and tested. The digital systems used in this thesis have several advantages over both analog systems and off-the-shelf digital systems. Advantages over analog systems include more flexibility for rapid re-configuration, the ability to define the control systems with more granularity, and additional automation options. Advantages over off-the-shelf digital systems include the use of an open computing standard for the hardware for increased flexibility, and the development of the firmware by the Maschine Strahlkontrollen department at DESY to ensure ease of collaboration.

Two different digital systems are compared to the analog system controlling the frequency of the RL. The first is using the analog electronics to demodulate and adjust the offset of the error signal used in Pound-Drever-Hall frequency sensing, and replacing the analog servo with a digital system using a field-programmable gate array to produce the control signal sent to the frequency actuator. This system includes all noise sources present in the analog system—though some of those noise sources seem to produce more noise in this hybrid digital setup than in the analog system—as well as additional ones, and thus results in more frequency noise. A digital system taking the input directly from the photodetector and performing all demodulation on-board was able to reduce the sensing noise significantly over the analog/digital hybrid system. As such, the performance was significantly better and very similar to the analog system. This indicates that digital systems are capable of very good performance in control over the cavities in ALPS IIc.

The most important role for digital systems is not the frequency control that can be implemented easily with analog systems, but rather the control of the resonance overlap between the two cavities. This system benefits significantly from faster actuation of

the phase between the two cavities than the length actuator is able to provide. This additional speed can be provided by a phase-locked loop (PLL) that can follow phase changes very fast as well as keep track of the net phase change to use as the input to the length control system. This is easily implemented as a digital system using an NCO to maintain the PLL and using accumulators to track the exact phase of the NCO. Though this system is intended to be used to keep two cavities in phase, there are ways to test the performance using a single cavity and two lasers.

The performance of this system was compared to the other frequency control systems in this thesis, even though those control systems directly measured the frequency of the cavity resonance compared to the input field. The performance of the digital PLL-based control system is better than the analog/digital hybrid, and is similar to both the fully analog system and the fully digital system.

As discussed earlier, one of the primary performance drivers of a system is the transfer function. The length control system is not able to suppress noise as well as frequency control systems because the magnitude of the transfer function is limited by the smaller actuator bandwidth. As such, actuating on the frequency but using a transfer function similar to that of the length control system should have similar performance to a length actuation system. This system was tested and the noise suppression was projected onto ALPS IIc to result in an RMS frequency noise of 2.5 Hz, which is larger than the length control system with resonance compensation, but does meet the requirements.

Work is ongoing on implementing length control with the digital system, as well as attempts to implement improvements with the current frequency control. As it stands, the digital control in ALPS IIa shows great promise for use in ALPS IIc and is worth pursuing. The frequency control system with digital demodulation is nearly at parity with the fully analog frequency control system in ALPS IIa. For ALPS IIc, an additional fast phase actuator will be used, so more improvements are needed for that system. The digital phase-locked loop system meets the ALPS IIc requirements with the frequency control simulation. Improvements to that system are required for use in a length actuation system, but some changes can also be made to further improve the performance in a way that would be difficult for an analog system.

Bibliography

- [1] M. Tanabashi et al., Phys. Rev. D **98**, 030001 (2018).
- [2] R. D. Peccei and H. R. Quinn, Phys. Rev. Lett. **38**, 1440 (1977).
- [3] M. Meyer, D. Horns, and M. Raue, Phys. Rev. D **87**, 035027 (2013).
- [4] M. Giannotti, I. Irastorza, J. Redondo, and A. Ringwald, Journal of Cosmology and Astroparticle Physics **2016**, 057 (2016).
- [5] L. Abbott and P. Sikivie, Physics Letters B **120**, 133 (1983).
- [6] P. Arias, J. Jaeckel, J. Redondo, and A. Ringwald, Phys. Rev. D **82**, 115018 (2010).
- [7] V. Anastassopoulos et al., Nature Physics **13**, 584 (2017).
- [8] B. L. and, Journal of Physics: Conference Series **1342**, 012070 (2020).
- [9] T. Braine et al., Phys. Rev. Lett. **124**, 101303 (2020).
- [10] B. T. McAllister et al., Physics of the Dark Universe **18**, 67 (2017).
- [11] L. Zhong et al., Phys. Rev. D **97**, 092001 (2018).
- [12] J. L. Ouellet et al., Phys. Rev. Lett. **122**, 121802 (2019).
- [13] B. M. Brubaker et al., Phys. Rev. Lett. **118**, 061302 (2017).
- [14] P. Sikivie, Phys. Rev. Lett. **51**, 1415 (1983).
- [15] K. Van Bibber, N. R. Dagdeviren, S. E. Koonin, A. K. Kerman, and H. N. Nelson, Phys. Rev. Lett. **59**, 759 (1987).
- [16] R. Cameron et al., Phys. Rev. D **47**, 3707 (1993).
- [17] E. Zavattini et al., Phys. Rev. Lett. **96**, 110406 (2006).
- [18] E. Zavattini et al., Phys. Rev. D **77**, 032006 (2008).
- [19] A. S. Chou et al., Phys. Rev. Lett. **100**, 080402 (2008).
- [20] M. Fouché et al., Phys. Rev. D **78**, 032013 (2008).
- [21] R. Battesti et al., Phys. Rev. Lett. **105**, 250405 (2010).

- [22] P. Pugnati et al., Phys. Rev. D **78**, 092003 (2008).
- [23] M. Betz, F. Caspers, M. Gasior, M. Thumm, and S. W. Rieger, Phys. Rev. D **88**, 075014 (2013).
- [24] K. Ehret et al., Physics Letters B **689**, 149 (2010).
- [25] J. Redondo and A. Ringwald, Contemporary Physics **52**, 211 (2011).
- [26] R. Bähre et al., Journal of Instrumentation **8**, T09001 (2013).
- [27] F. Hoogeveen and T. Ziegenhagen, Nuclear Physics B **358**, 3 (1991).
- [28] Y. Fukuda, T. Kohmoto, S. ichi Nakajima, and M. Kunitomo, Progress in Crystal Growth and Characterization of Materials **33**, 363 (1996).
- [29] P. Sikivie, D. B. Tanner, and K. van Bibber, Phys. Rev. Lett. **98**, 172002 (2007).
- [30] C. Albrecht et al., Straightening of Superconducting HERA Dipoles for the Any-Light-Particle-Search Experiment ALPS II, 2020.
- [31] T. Kozłowski, R. Shah, and R. Smith, Any Light Particle Search II, Poster presented at DESY FH Open Day, 2019.
- [32] A. Hallal et al., The heterodyne sensing system for the ALPS II search for sub-eV weakly interacting particles, 2020.
- [33] A. E. Siegman, *Lasers*, University Science Books, 1986.
- [34] R. W. P. Drever et al., Applied Physics B **31**, 97 (1983).
- [35] R. V. Pound, Review of Scientific Instruments **17**, 490 (1946).
- [36] A. Abramovici et al., Science **256**, 325 (1992).
- [37] S. Seel, R. Storz, G. Ruoso, J. Mlynek, and S. Schiller, Physical Review Letters **78**, 4741 (1997).
- [38] E. D. Black, American Journal of Physics **69**, 79 (2001).
- [39] R. W. Boyd, *Nonlinear Optics, Third Edition*, Academic Press, Inc., USA, 3rd edition, 2008.
- [40] B. E. A. Saleh and M. C. Teich, *Fundamentals of Photonics*, Wiley Series in Pure and Applied Optics, Wiley, 2007.
- [41] A. Spector, ALPS Technical Note: Calculating the coupling of the axion-like field and the RC, 2019.
- [42] J. H. Pöld and H. Grote, ALPS II design requirement document, Internal Note ID: D00000008263751, 2020.

-
- [43] M. T. Hartman et al., Design of the ALPS II Optical System, 2020.
- [44] P. Kwee et al., *Opt. Express* **20**, 10617 (2012).
- [45] M. Frede et al., *Opt. Express* **15**, 459 (2007).
- [46] J. H. Pöld and A. D. Spector, *EPJ Techniques and Instrumentation* **7**, 1 (2020).
- [47] G. F. Franklin, D. J. Powell, and A. Emami-Naeini, *Feedback Control of Dynamic Systems*, Prentice Hall PTR, USA, 5th edition, 2006.
- [48] A. Abramovici and J. Chapsky, *Feedback Control Systems: A Fast-Track Guide for Scientists and Engineers*, Kluwer Academic Publishers, USA, 2000.
- [49] S. Saperstone, *Introduction to Ordinary Differential Equations*, Brooks/Cole Pub., 1998.
- [50] M. Morari, M. Zafiriou, and E. Zafiriou, *Robust Process Control*, Prentice Hall, 1989.
- [51] A. V. Oppenheim and R. W. Schaffer, *Discrete-Time Signal Processing*, Prentice Hall Press, USA, 3rd edition, 2009.
- [52] L. B. Jackson, *Digital Filters and Signal Processing: With MATLAB Exercises*, Kluwer Academic Publishers, USA, 3rd edition, 1996.
- [53] C. L. Mueller et al., *Review of Scientific Instruments* **87**, 014502 (2016).
- [54] T. Isogai, J. Miller, P. Kwee, L. Barsotti, and M. Evans, *Opt. Express* **21**, 30114 (2013).
- [55] P. Kwee and B. Willke, *Appl. Opt.* **47**, 6022 (2008).
- [56] A. D. Spector, J. H. P. old, R. Bähre, A. Lindner, and B. Willke, *Opt. Express* **24**, 29237 (2016).
- [57] N. C. Wong and J. L. Hall, *J. Opt. Soc. Am. B* **2**, 1527 (1985).
- [58] D. Miller, *Seismic noise analysis and isolation concepts for the ALPS II experiment at DESY*, PhD thesis, Leibniz Universitt Hannover, 2020.
- [59] M. Endo and T. R. Schibli, *OSA Continuum* **1**, 116 (2018).
- [60] MicroTCA (MTCA.0), Standard, PCI Industrial Computer Manufacturers Group, Wakefield, MA, USA, 2006.
- [61] MicroTCA Enhancements for Rear I/O and Precision Timing (MTCA.4), Standard, PCI Industrial Computer Manufacturers Group, Wakefield, MA, USA, 2011.

- [62] B. Friedland, *Control System Design: An Introduction to State-Space Methods (Dover Books on Engineering)*, Dover Publications, Inc., New York, NY, USA, 2005.
- [63] G. F. Franklin, M. L. Workman, and D. Powell, *Digital Control of Dynamic Systems*, Addison-Wesley Longman Publishing Co., Inc., Boston, MA, USA, 3rd edition, 1997.
- [64] S. R. Gillmer, R. C. G. Smith, S. C. Woody, and J. D. Ellis, *Measurement Science and Technology* **25**, 075205 (2014).
- [65] R. C. G. Smith, A. M. Sarangan, Z. Jiang, and J. R. Marciante, *Opt. Express* **20**, 4436 (2012).
- [66] R. C. G. Smith, A. M. Sarangan, and J. R. Marciante, Direct Measurement of Bend-Induced Mode Deformation Using a Helical-core Fiber, in *Frontiers in Optics 2010/Laser Science XXVI*, page FWK3, Optical Society of America, 2010.

A. State Space Models

Frequency-domain analysis and design of control systems is valuable in many situations. However, some systems are more easily represented in state space. Additionally, sometimes the implementation of control systems is done in state space, which is the case for many of the digital systems in this thesis. This appendix will discuss the formalism of state space as well as how to convert between state space and transfer function models.

A.1. State Space Representation

The majority of this and the following two sections are similar to the presentation and derivations found in [62]. They are presented here for reference. Similar to the description of the outputs in terms of linear, constant coefficient differential equations, we can describe the states of a system in a series of linear, first order differential equations

$$\begin{aligned}\dot{x}_1 &= \sum_{k=1}^m a_{1k}x_k + b_1u, \\ \dot{x}_2 &= \sum_{k=1}^m a_{2k}x_k + b_2u, \\ &\dots \\ \dot{x}_m &= \sum_{k=1}^m a_{mk}x_k + b_mu,\end{aligned}\tag{A.1}$$

where the collection of m number of x variables describe the state of the system, u describes the input to the system, the a variables describe how certain state variables interact with each other, and the b variables describe how the input couples to the state of the system. We will be suppressing the explicit t -dependence of all variables, since it adds no clarity, but all lower-case x , y , and u variables are assumed to be dependent on t .

Given potentially large numbers of variables, it becomes convenient to collect the state variables into a vector

$$\vec{x} = \begin{bmatrix} x_1 \\ x_2 \\ \vdots \\ x_m \end{bmatrix}, \quad (\text{A.2})$$

and then convert the a and b variables into matrices to re-write Equation A.1 into the much simpler form

$$\dot{\vec{x}} = \mathbf{A}\vec{x} + \mathbf{B}u, \quad (\text{A.3})$$

where \mathbf{A} is in this case an $m \times m$ square matrix, and \mathbf{B} is a $m \times 1$ vector. A separate equation is needed to show the output of the system, in this case the output, y . In a linear, time-invariant system, y can be given by a linear combination of the state of the system and the inputs of the system,

$$y = \mathbf{C}\vec{x} + Du, \quad (\text{A.4})$$

where \mathbf{C} is a $1 \times m$ matrix and D is a scalar. The full single input, single output system is described in Equations A.3 and A.4.

A.2. Converting a State-Space Model to a Transfer Function Model

Both the transfer function and state space models are different ways of looking at physical systems, therefore it is possible that there may be need to convert between the two. In this section, the process of converting a state space model to a transfer function will be shown and in the next section, the reverse process is presented.

Since we will be converting the time-domain state space model to a complex frequency-domain transfer function, the first step is to take the Laplace transform of Equation A.3

$$s\vec{X}(s) - \vec{x}(0) = \mathbf{A}\vec{X}(s) + \mathbf{B}U(s), \quad (\text{A.5})$$

where $\vec{x}(0)$ is the state of the system at $t = 0$. Just as in Section 2.2, this initial state is important for determining the exact state of a system at a given time, it is not vital for input vs. output analysis and can be assumed to be zero. Once that is done, the previous equation can be re-arranged to solve for $X(s)$ and results in

$$\vec{X}(s) = (s\mathbf{I} - \mathbf{A})^{-1}\mathbf{B}U(s), \quad (\text{A.6})$$

where \mathbf{I} is the identity matrix. Similarly to this Laplace transform, the Laplace transform of Equation A.4 is

$$Y(s) = \mathbf{C}\vec{X}(s) + DU(s). \quad (\text{A.7})$$

If we substitute Equation A.6 into Equation A.7, we get

$$Y(s) = \mathbf{C}(s\mathbf{I} - \mathbf{A})^{-1}\mathbf{B}U(s) + DU(s). \quad (\text{A.8})$$

This can be easily re-arranged to give us the transfer function in terms of our state matrices

$$\frac{Y(s)}{U(s)} = H(s) = \mathbf{C}(s\mathbf{I} - \mathbf{A})^{-1}\mathbf{B} + D. \quad (\text{A.9})$$

One could stop at this step and calculate the frequency response, $H(i\omega)$, but it is possible to continue and calculate each individual coefficient, a_k and b_k from Equation 2.15. This involves calculating the $(s\mathbf{I} - \mathbf{A})^{-1}$ by its relationship to the adjugate and determinant given which is

$$\mathbf{G}^{-1} = \frac{1}{\det(\mathbf{G})}\text{adj}(\mathbf{G}). \quad (\text{A.10})$$

With this, we can re-write Equation A.9 as

$$\frac{Y(s)}{U(s)} = H(s) = \frac{\text{adj}(s\mathbf{I} - \mathbf{A})\mathbf{C}\mathbf{B} + D}{\det(s\mathbf{I} - \mathbf{A})}. \quad (\text{A.11})$$

At this point, possible calculate the coefficients of the denominator, as we can set the denominator of the standard transfer function equal to the denominator of Equation A.11. The form of the determinant will be a polynomial of maximum order m . This is because with $s\mathbf{I}$ each diagonal element has a factor of s . All terms with like powers of s can then be collected into that polynomial, which take the form

$$\det(s\mathbf{I} - \mathbf{A}) = \sum_{k=0}^m a_{m-k}s^k, \quad (\text{A.12})$$

where all of the a terms are determined by the calculation of the determinant. As one note, the order of the numerator and denominator of the transfer function have been set equal to each other, that is $m = n$. Though this is generally not the case, it can be done in this instance as the coefficients a_k and b_k can be zero for factors of s that are larger than the order of the numerator or denominator.

The calculation of each element of $\text{adj}(s\mathbf{I} - \mathbf{A})$ can also be done by combining orders of s . Since the magnitude of each element, i and j , of $\text{adj}(\mathbf{G})$ is given by the determinant of a sub-matrix of \mathbf{G} with row i and column j removed, we know that we will have a polynomial of order s^{m-1} , since every determinant will have one factor of s removed. This means $\text{adj}(s\mathbf{I} - \mathbf{A})$ will take the form

$$\text{adj}(s\mathbf{I} - \mathbf{A}) = \sum_{k=1}^m \mathbf{E}_k s^{m-k}, \quad (\text{A.13})$$

This can be calculated from the adjugate directly, but it is useful to look at another way to calculate this by re-arranging Equation A.10 to get

$$\mathbf{G} \text{adj}(\mathbf{G}) = \det(\mathbf{G})\mathbf{I}, \quad (\text{A.14})$$

and we can then substitute $s\mathbf{I} - \mathbf{A}$ in for \mathbf{G} as well as the solutions for the various parts in Equation A.12 and A.13. This gives us the relationship

$$\sum_{k=0}^m a_{m-k} s^k \mathbf{I} = (s\mathbf{I} - \mathbf{A}) \left(\sum_{k=1}^m \mathbf{E}_k s^{m-k} \right). \quad (\text{A.15})$$

Here we can set powers of s equal to get the following recursive relationship for E_k

$$\begin{aligned} \mathbf{E}_1 &= \mathbf{I} \\ \mathbf{E}_2 &= a_1 \mathbf{I} + \mathbf{A} \mathbf{E}_1 \\ &\vdots \\ \mathbf{E}_m &= a_{m-1} \mathbf{I} + \mathbf{A} \mathbf{E}_{m-1} \\ 0 &= a_m \mathbf{I} + \mathbf{A} \mathbf{E}_m \end{aligned} \quad (\text{A.16})$$

Though it is often easier to simply calculate the adjugate, this derivation tells us that the first term, \mathbf{E}_1 , is simply the identity matrix. Additionally, this method can provide a useful check that the adjugate is being calculated correctly.

Once $(s\mathbf{I} - \mathbf{A})^{-1}$ is calculated, we can substitute the results of Equations A.12 and A.13 into A.11 to get

$$H(s) = \frac{\mathbf{C} \mathbf{B} s^{m-1} + \mathbf{C} \left(\sum_{k=2}^m \mathbf{E}_k s^{m-k} \right) \mathbf{B}}{\det(s\mathbf{I} - \mathbf{A})} + D. \quad (\text{A.17})$$

This equation shows that the order of s in the numerator will always be less than the denominator unless $D \neq 0$. Additionally, we can see that the order of the transfer function is m , which is the same as the order of the state space system. When describing the complexity of a system, an m -order transfer function is equivalently complex as an $m \times m$ state space system.

A.3. Converting a Transfer Function Model to a State-Space Model

Similar to Section A.2, it may be useful to convert from an existing transfer function model to a state-space model. This section presents how that conversion can be done.

In doing this, we will make a few modifications to the transfer function in Equation 2.15. The first is that we will set the orders of the numerator and the denominator as equal to each other, that is $m = n$ just as we did in the previous section. The second is that we will divide a_0 , the coefficient for s^m , from the denominator. In Section 2.3 we showed that the relative degree cannot be less than zero, $n - m \geq 0$. Using this fact, we know that a_0 cannot be zero. This gives us

$$H(s) = \frac{\sum_{k=0}^m b_{m-k} s^k}{s^m + \sum_{k=0}^{m-1} a_{m-k} s^k}, \quad (\text{A.18})$$

where a_k and b_k are not the same as in Equation 2.15 but are re-defined as the original a_k/a_0 and b_k/a_0 .

We can consider the case where the transfer function has no zeros, that is b_0 through b_{m-1} are zero. This transfer function looks like

$$H(s) = \frac{b_m}{s^m + \sum_{k=0}^{m-1} a_{m-k} s^k}. \quad (\text{A.19})$$

In this case, we can re-arrange our inputs and outputs to obtain the equation

$$\left(s^m + \sum_{k=0}^{m-1} a_{m-k} s^k \right) Y(s) = b_m U(s), \quad (\text{A.20})$$

which is just a specific version of the more general form seen in Equation 2.14. Using the inverse Laplace transform, we can get back to the differential equation that would give us the transfer function in Equation A.19

$$\frac{d^m}{dt^m} y + \sum_{k=0}^{m-1} \frac{a_{m-k} d^k y}{dt^k} = b_m u, \quad (\text{A.21})$$

which can be re-arranged to get

$$\frac{d^m}{dt^m} y = - \sum_{k=0}^{m-1} \frac{a_{m-k} d^k y}{dt^k} + b_m u. \quad (\text{A.22})$$

If we then identify a series of variables, x_1 through x_m where

$$\begin{aligned} x_1 &= \frac{d^{m-1}}{dt^{m-1}} y \\ x_2 &= \frac{d^{m-2}}{dt^{m-2}} y \\ &\dots \\ x_{m-1} &= \frac{d}{dt} y \\ x_m &= y, \end{aligned} \quad (\text{A.23})$$

we can see that there is a recursive relationship between the variables such that

$$\begin{aligned}
\frac{d}{dt}x_2 &= x_1 \\
&\dots \\
\frac{d}{dt}x_{m-1} &= x_{m-2} \\
\frac{d}{dt}x_m &= x_{m-1},
\end{aligned} \tag{A.24}$$

and if we take the derivative of x_1 with respect to time, we see that

$$\frac{d}{dt}x_1 = \frac{d^m}{dt^m}y = -\sum_{k=0}^n \frac{a_{n-k}d^k y}{dt^k} + b_m u. \tag{A.25}$$

If we combine these equations, we can get a full equation for the state of the system

$$\begin{aligned}
\dot{x}_1 &= -\sum_{k=0}^n \frac{a_{n-k}d^k y}{dt^k} + b_m u \\
\dot{x}_2 &= x_1 \\
&\dots \\
\dot{x}_{m-1} &= x_{m-2} \\
\dot{x}_m &= x_{m-1},
\end{aligned} \tag{A.26}$$

which can be represented in the same way as other state equations, where the coefficients preceding the x variables are the appropriate elements of the \mathbf{A} matrix, and \mathbf{B} is given by

$$\begin{aligned}
x_1 &= b_m u \\
x_2 &= 0 \\
&\dots \\
x_{m-1} &= 0 \\
x_m &= 0,
\end{aligned} \tag{A.27}$$

which is the same form as is in Equation A.3. Furthermore, since $x_m = y$, the only output, \mathbf{C} is given by

$$y = x_m \tag{A.28}$$

The ordering of which x variables map to each other is arbitrary and not unique. It is, however, easier when the relationship between the x variables is recursive between adjacent rows.

With a more general transfer function of the form found in Equation A.18 we can multiply by $Z(s)/Z(s)$, where $Z(s)$ will be calculated shortly. This yields

$$\frac{Y(s) Z(s)}{Z(s) U(s)} = \frac{\sum_{k=0}^m b_{m-k} s^k}{s^m + \sum_{k=0}^{m-1} a_{m-k} s^k}, \tag{A.29}$$

thus giving us two equations that can be arranged to give us $U(s)$ and $Y(s)$ in terms of $Z(s)$

$$\begin{aligned} Y(s) &= \left(\sum_{k=0}^m b_{m-k} s^k \right) Z(s) \\ U(s) &= \left(s^m + \sum_{k=0}^{m-1} a_{m-k} s^k \right) Z(s). \end{aligned} \tag{A.30}$$

Once the equations are in this form, it makes sense to take the inverse Laplace transform as before, to get

$$\begin{aligned} y &= \sum_{k=0}^n \frac{b_{n-k} d^k z}{dt^k} \\ u &= \frac{d^m}{dt^m} z + \sum_{k=0}^{m-1} \frac{a_{m-k} d^k z}{dt^k}. \end{aligned} \tag{A.31}$$

Similar to the case above where we have no zeros, we then identify a series of variables, x_1 through x_m where

$$\begin{aligned} x_1 &= \frac{d^{m-1}}{dt^{m-1}} z \\ x_2 &= \frac{d^{m-2}}{dt^{m-2}} z \\ &\dots \\ x_{m-1} &= \frac{d}{dt} z \\ x_m &= z. \end{aligned} \tag{A.32}$$

We can see that there is the same recursive relationship between the variables as in Equation A.24. As such, the \mathbf{A} and \mathbf{B} matrices are calculated in much the same way as the previous case, as seen when we solve for the highest-order derivative

$$\frac{d^m}{dt^m} z = \dot{x}_1 = - \sum_{k=1}^m a_k x_k + u, \tag{A.33}$$

where we have reversed the sum indexing for clarity. Which gives us the equation for the first state variable in the form as found in Equation A.3. The rest of the state variables are the same as in Equation A.26, which gives us the state matrices \mathbf{A} and \mathbf{B} .

Solving for the \mathbf{C} matrix as well as D requires using the state variables defined in in Equation A.32 to substitute in state variables. Additionally, since $d^m z / dt^z$ is not a state variable, we must use in the results from Equation A.33. Combining those results with the equation for y in Equation A.31, we get an equation for the output

$$y = \sum_{k=1}^m (b_k - b_0 a_k) x_k + b_0 u, \quad (\text{A.34})$$

which is the same form as Equation A.4, and so we can determine the values of \mathbf{C} and D from this equation.

A.4. Discrete State Space

Just as with the transfer function, in discrete time, the state equations are slightly different from the continuous time variant. For the determination of the state variables of the system, we start with the assumption that the state of the next sample depends on current input and current state. A way to write this for a single input, single out system in a matrix format similar to Section A.1 would be

$$\vec{x}([n+1]T) = \mathbf{A}\vec{x}(nT) + \mathbf{B}u(nT). \quad (\text{A.35})$$

If we then look at the output, we make the assumption that the output at the current sample depends on the current state, as well as the current input. Writing this in the same way that we wrote Equation A.35, we get

$$y(nT) = \mathbf{C}\vec{x}(nT) + Du(nT). \quad (\text{A.36})$$

As with the transfer function, the formalism of state space in discrete time remains very similar to the formalism in continuous time. Since the formalism is the same, the conversion between transfer functions and state space models is very similar.

A.5. Converting a Transfer Function Model to a State-Space Model in Discrete Time

With this formalism in place, we can again look at converting transfer functions into state space matrices just like in Section A.3. We will see that the calculation of the state space matrices from the transfer function is done in a way that is essentially identical to the way it is done in continuous time [63]. One of the important properties of the Z transform that we will use for this is that of time-delay, where we get

$$Z\{f_{n-k}\} = z^{-k}F(z). \quad (\text{A.37})$$

We start off by taking Equation 2.31 and multiplying by z^m/z^m , giving us

$$H(z)\frac{z^m}{z^m} = \frac{\sum_{k=0}^m \beta_{m-k}z^k}{z^m} \frac{z^m}{z^m + \sum_{k=0}^{m-1} \alpha_{m-k}z^k} = \frac{\sum_{k=0}^m \beta_k z^{-k}}{1 + \sum_{k=1}^m \alpha_k z^{-k}}. \quad (\text{A.38})$$

Just as we did with continuous time in Equation A.29, we can break this into two functions multiplied with each-other

$$\frac{Y(z) P(z)}{P(z) U(z)} = \frac{\sum_{k=0}^m \beta_k z^{-k}}{1 + \sum_{k=1}^m \alpha_k z^{-k}}, \quad (\text{A.39})$$

and then split that into two equations that can be arranged to solve for $Y(z)$ and $U(z)$

$$\begin{aligned} Y(z) &= \left(\sum_{k=0}^m \beta_k z^{-k} \right) P(z) \\ U(z) &= \left(1 + \sum_{k=1}^m \alpha_k z^{-k} \right) P(z). \end{aligned} \quad (\text{A.40})$$

If we use the time shifting property in Equation A.37, we can get two equations in the time-domain

$$\begin{aligned} y_n &= \sum_{k=0}^m \beta_k p_{n-k} \\ u_n &= p_n + \sum_{k=1}^m \alpha_k p_{n-k}. \end{aligned} \quad (\text{A.41})$$

We can re-arrange the equation for u_n to get

$$p_n = - \sum_{k=1}^m \alpha_k p_{n-k} + u_n. \quad (\text{A.42})$$

Now, we can begin to define our state variables similar to the way we did in Equation A.32 to get

$$\begin{aligned} x_1 &= p_{n-1} \\ x_2 &= p_{n-2} \\ &\dots \\ x_{m-1} &= p_{n-m-1} \\ x_m &= p_n, \end{aligned} \quad (\text{A.43})$$

which turns into the recursive relationship similar to Equation A.24, which is more easily shown by re-introducing the functional notation of $f(nT) = f_n$

$$\begin{aligned} x_1(nT) &= p([n-1]T) \\ x_2(nT) &= x_1([n-1]T) \\ &\dots \\ x_{m-1}(nT) &= x_{m-2}([n-1]T) \\ x_m(nT) &= x_{m-1}([n-1]T). \end{aligned} \quad (\text{A.44})$$

When we advance x_1 in time by one sample, we get

$$x_1([n+1]T) = -\sum_{k=1}^m \alpha_k p_{n-k} + u_n, \quad (\text{A.45})$$

and combining this equation with our recursive relationship, we can see that

$$\begin{aligned} x_1([n+1]T) &= -\sum_{k=1}^m \alpha_k p_{n-k} + u_n \\ x_2([n+1]T) &= x_1 \\ &\dots \\ x_{m-1}([n+1]T) &= x_{m-2} \\ x_m([n+1]T) &= x_{m-1}. \end{aligned} \quad (\text{A.46})$$

These equations can then tell us how to build our \mathbf{A} and \mathbf{B} matrices as given in Equation A.35. And similarly, we can substitute Equation A.45 in for p_n in the equation for y_n in Equation A.41 and collect like terms to get

$$y_n = \sum_{k=1}^m (\beta_k - \beta_0 \alpha_k) p_{n-k} + \beta_0 u_n, \quad (\text{A.47})$$

which can be combined with the state vector in Equation A.44 to get the state matrix \mathbf{C} , and D in Equation A.36. This calculation is exactly the same as the one done in Section A.3, and just as that is the same, the conversion from state space to transfer function is identical and will not be included for discrete time.

Acknowledgments

The journey to a doctoral degree is not one that begins at the start of doctoral work. My journey into optics was started by Narayanan Kuthirummal, and for that start I am very thankful. Additionally, my time at the University of Rochester Institute of Optics was incredibly valuable, and I thank especially John Marciante and Jonathan Ellis for supervising and supporting my experimental work there.

My time at DESY and AEI has been filled with incredibly valuable experiences, especially because of the people I have had the pleasure to interact with. I have been lucky to have had Benno Willke as my adviser, who has consistently left me with more motivation and understanding of the task at hand after every conversation, despite the difficulty of advising from a distance. My time at DESY has been made significantly easier and more enjoyable by having Axel Lindner as a supervisor, who has almost always been available for guidance despite his incredibly busy schedule. Of course, I could not go without mentioning the incredible help that Aaron Spector and Jan Pöld have been in progressively challenging me and giving me the tools to do the best work I could do. Finally, the entire ALPS group both at DESY and the entire collaboration has been an absolute joy to work with and I cannot imagine a better group of people to realize this ambitious experiment.

The work in this thesis would not have been possible without the support of people outside the ALPS group. Sven Pfeiffer's assistance has been invaluable for his knowledge of controls and giving me the tools to develop a small fraction of that same knowledge. Collaborating with Lukasz Butkowski to design and implement the digital systems in this thesis was the difference between writing a thesis about why the systems did not work, and being able to achieve the very promising results presented here. In addition to converting the requests into reality, he was extremely helpful in helping me understand how the whole system was functioning. Additional thanks belong to the MSK group as a whole for supporting this effort, providing advice on hardware, and helping with the initial setup despite my inexperience.

Special thanks are also in order for those who read and reviewed my thesis. For this I must again thank Aaron Spector and Jan Pöld, as well as Sven Pfeiffer. This document is significantly improved thanks to their efforts.

Finally, I am lucky to have had great support outside of work. Most importantly, I would like to thank my wife, Nicole Kendrot, for moving to a new country with me to help me achieve my dream. Her help and support is a key reason I have undertaken this effort. I would also like to thank my parents, Evelyn and Rick, for pushing and helping me to achieve anything that I wanted to achieve. Those friends and family who have helped in large and small ways are too numerous to name, though I would especially single out Zeke and Moki for being there for me every day.

I would also like to acknowledge the ComponentLibrary from Alexander Franzen, which was used for all of the schematic diagrams in this thesis under a Creative Commons Attribution-NonCommercial 3.0 Unported License and found at <http://www.gwoptics.org/ComponentLibrary>. Some of the components used were slightly modified to better describe the systems in this thesis.

Curriculum Vitae

Richard Cameron Gardner Smith
Schäferstr. 19
20357 Hamburg, Germany

Born on 4 April 1985 in Beverly, Massachusetts

Work Experience

- 2017–Present** **Graduate Research Assistant** *Deutsches Elektronen-Synchrotron*
Hamburg, Germany
- 2015–2017** **Electronics/Lead Systems Engineer** *Night Vision and Electronic Sensors Directorate, U.S. Army*
Fort Belvoir, Virginia, USA
- 2013–2015** **Applications Engineer** *Semrock, Inc.*
Rochester, New York, USA
- 2008–2013** **Graduate Research Assistant** *The Institute of Optics, The University of Rochester*
Rochester, New York, USA

Education

- 2008–2013** **Master of Science in Optics** University of Rochester
Masters Thesis: *Physical Optics Analysis of a Fiber-Delivered Displacement Interferometer*
- 2003–2007** **Bachelor of Science in Physics** College of Charleston
Bachelors Thesis: *Fabrication and testing of Neodymium-doped borophosphate glasses*
- 1999-2003** **High School Diploma** Thomas Jefferson High School for Science and Technology

Publications

M. T. Hartman et al., Design of the ALPS II Optical System, 2020

S. R. Gillmer, R. C. G. Smith, S. C. Woody, and J. D. Ellis, Measurement Science and Technology **25**, 075205 (2014)

R. C. G. Smith, A. M. Sarangan, Z. Jiang, and J. R. Marciante, Opt. Express **20**, 4436 (2012)

R. C. G. Smith, A. M. Sarangan, and J. R. Marciante, Direct Measurement of Bend-Induced Mode Deformation Using a Helical-core Fiber, in *Frontiers in Optics 2010/Laser Science XXVI*, page FWK3, Optical Society of America, 2010